MASTER THESIS

Automatic depth measurements of lower-extremity arteries and carotid artery tortuosity, curvature and torsion measurements

J. Klaassen

March 27, 2020

Examination committee:

Prof. dr. ir. C.H. Slump	(Chairman and Technical supervisor)
Dr. C.E.V.B. Hazenberg	(Medical supervisor)
Drs. R.J. Haarman	(Process supervisor)
Dr. E. Groot Jebbink	(External member)

UNIVERSITY OF TWENTE

Preface

In september 2012 begon ik in Enschede aan de opleiding Technische Geneeskunde. Na 4 intensieve jaren in de bachelorfase, waarin het maken van hertentamens meer regel dan uitzondering was, uiteindelijk doorgestroomd naar de master Technical Medicine om mijzelf te verdiepen in de richting van 'Imaging & Interventions'. De masterstages hebben mij langs interessante stageafdelingen in verschillende centra in Nederland geleid. Tijdens deze stages heb ik ontdekt dat mijn interesses vooral bij zogeheten snijdende specialismen liggen. Uiteindelijk heeft het ervoor gezorgd dat ik voor mijn M3 afstudeerstage terecht ben gekomen op de afdeling vaatchirurgie in het UMC Utrecht. Ondanks dat het een lang en bewogen jaar is geweest, heb ik op deze afdeling leuke en vooral ook leerzame ervaringen opgedaan. Naast het feit dat ik zeer vaak van toegevoegde waarde kon zijn tijdens complexe endovasculaire operaties, heb ik ook aan twee uitdagende opdrachten mogen werken. Uiteindelijk resulteert dit in de thesis zoals deze voor u ligt en wordt het na bijna acht jaar studeren tijd voor een nieuwe uitdaging. Graag wil een aantal personen bedanken die hebben bijgedragen aan de totstandkoming van deze thesis.

Allereerst wil ik graag Stijn Hazenberg bedanken voor de mogelijkheid om mijn afstudeerstage bij de vaatchirurgie in het UMC Utrecht te doen en voor de begeleiding in het afgelopen jaar. Gedurende het hele jaar ben jij laagdrempelig bereikbaar geweest en hebben we onder het genot van een goede koffie vaak mijn voortgang besproken. Bovendien ben ik erg dankbaar voor de ruimte en steun die je mij hebt geboden rondom het overlijden van mamma. Ik kijk dan ook met veel plezier terug op onze samenwerking en ben blij dat ik de keuze heb gemaakt om bij jou te komen afstuderen.

Ten tweede wil ik graag professor Slump bedanken voor de persoonlijke begeleiding, scherpe analyses en punctuele controle van de draftversie van mijn thesis. Ik denk met veel plezier terug aan de lol die u heeft beleefd om de foto's die wij in onze werkkamer op de lamellen hadden geplakt.

Ook wil ik graag Rian Haarman bedanken voor de procesbegeleiding en de gesprekken over mijn persoonlijke ontwikkeling. Alhoewel ik altijd vrij sceptisch was over VCPG, heb jij ervoor gezorgd dat ik hier anders naar ben gaan kijken. Ik wil je graag bedanken voor het luisterende oor wat je hebt geboden en de leuke en gezellige intervisie momenten die wij het afgelopen twee jaar hebben gehad. Uiteraard wil ik Evelien, Nynke en Mirte hier voor ook bedanken. Ik heb veel van onze gesprekken geleerd.

Tot slot wil ik graag familie, Esmé en vrienden bedanken voor alle support, vertrouwen en de nodige ontspannende activiteiten tijdens het afgelopen jaar. Zonder hen had ik de eindstreep waarschijnlijk niet zo snel kunnen halen.

Nogmaals bedankt allen en ik wens jullie veel plezier met lezen,

Jurre Klaassen
Rotterdam, 25 maart 2020

Abstract

Aims To develop a technique that can automatically measure the depth of lower-extremity arteries and to address the clinical implication of carotid artery (CA) geometry expressed in tortuosity index (TI), curvature and torsion.

Method and Materials Manual depth measurements were performed by three independent observers in 5 predefined measurement directions at 4 anatomical locations in 35 unique computed tomography angiography (CTA) studies. Measurement reproducibility was assessed with intraclass correlation coefficient (ICC) and Bland-Altman plots. Next, automatic depth measurement technique was developed in MATLAB to measure lower-extremity arterial depth and validated using phantom study and same 35 CTA studies. Measurement agreement of manual and automatic performed arterial depth measurements at the superficial femoral artery (SFA) was assessed using ICC and Bland-Altman plots. To address clinical implication of CA geometry, two independent observers performed 175 TI measurements of the CA in 140 unique CTA studies using 3Mensio software. Moreover, MATLAB was used to calculate curvature and torsion using coordinates of exported 3Mensio 1mm interpolated CA central luminal line (CLL). Intra- and interobserver agreement was assessed using ICC and visualized using Bland-Altman plots. Moreover, correlation of TI, curvature and torsion was assessed when comparing intra-patient ipsi- and contralateral CA with present extracranial carotid artery aneurysm (ECAA) and when comparing CA of ECAA patients with control patients. Finally, Pearson correlation coefficient was calculated to test correlation between measured TI, curvature and torsion.

Results Assessed intraobserver agreement of manual performed depth measurements showed excellent reliability and agreement in SFA. Validation of developed automatic depth measurement technique showed that only the set requirement of maximum measurement deviation of 3mm was achieved. Moreover, assessed manual and automatic measurement agreement at the SFA showed excellent reliability and agreement. Furthermore, assessment of intra-and interobserver agreement of TI measurements showed excellent reliability and agreement all cases, indicating that TI measurements are reproducible. In addition, no significant difference was found between ipsi- and contralateral CA in ECAA patients, while this difference was significant between the ECAA and the control group. Moreover, strong and positive correlation was found between true length and sharp bends of the carotid arteries.

Conclusion The arterial depth of the lower extremities can be measured in any case at the level of the SFA using the developed automatic depth measurement technique. Furthermore, geometry of the CA in terms of tortuosity index, curvature and torsion, seems to be comparable within patients with a carotid aneurysm, but in comparison with control patients seems strikingly different. Additionally, a strong and positive correlation was found between true length and sharp bends of the carotid arteries.

Table of contents

Preface ii

Abstract iv

Chapter 1: Introduction 1

1.1 Research aims 1

1.2 Outline 1

Chapter 2: Development of an automatic depth measurement technique for measuring depth of the lower-extremity arteries in patients suffering from peripheral arterial disease 3

2.1 Clinical background 3

2.2 Research questions 5

2.3 Aim of the study 6

2.4 Manual measurements 6

2.4.1 Method 6

2.4.2 Results 8

2.5 Development of an automatic depth measurement technique 11

2.5.1 Requirements 11

2.5.2 Depth measurement algorithm 12

2.5.3 Validating the developed depth measurement algorithm 20

2.6 Automatic performed depth measurements. 22

2.6.1 Method 23

2.6.2 Results 23

2.7 Discussion 23

2.7.1 Manual depth measurements 24

2.7.2 Validation of developed depth measurement technique 26

2.7.3 Agreement of manual and automatic performed depth measurement at the 31

2.8 Conclusion 32

Chapter 3: The correlation of tortuosity, curvature and torsion in the extracranial carotid artery **33**

3.1 Clinical background 33

3.2 Research aims 34

3.3 Aim of the study 34

3.4 Method 35

3.4.1 Patient selection and image technique 35

3.4.2 Carotid tortuosity measurements 35

3.4.3 Carotid artery curvature and torsion measurements 35

3.4.4 Statistical analysis 37

3.5 Results 38

3.5.1 Interobserver agreement 38

3.5.2 Intraobserver agreement 39

3.5.3 The correlation of tortuosity, and curvature and torsion when comparing ipsi- and contralateral carotid artery in subjects with ECAA 39

3.5.4 The correlation of TI, curvature and torsion in ECAA subjects compared to control group without presence of ECAA 41

3.5.5 Correlation of measured tortuosity index, curvature and torsion in the carotid artery 41

3.6 Discussion 43

3.6.1 Tortuosity index measurement reproducibility 43

3.6.2 Curvature and torsion measurements 44

3.6.3 Correlation of TI, and curvature and torsion 46

3.7 Conclusion 47

Chapter 4: General discussion **49**

Bibliography **50**

Appendices **56**

Appendix A 56

Appendix B 58

List of figures

Figure 1	Schematic overview of thesis outline	2
Figure 2	Overview of progression of atherosclerosis starting at the initial lesion and ending at the complicated lesion.[25]	4
Figure 3	Association of risk factors with the level of atherosclerotic target lesions. Red overlay on the anatomic cartoon illustrates the association of risk factor with pattern of atherosclerotic lesions. Image and caption adapted from Diehm et al.[6]	5
Figure 4	Example of measurement performed at the external iliac artery. Measurement direction A, B, C, D and E correspond to five measurement directions described in section 2.4.1.2.	7
Figure 5	Bland-Altman plots for depth measurements in the AFS in measurements direction A (A), B (B), C (C), D (D) and E (E). Figures show comparison of measurements performed by observer 1 and 2 (Blue), observer 1 and 3 (Black) and observer 2 and 3 (Orange). In all plots the horizontal dotted colored lines represent from top to bottom the upper limit of agreement, the bias and the lower limit of agreement with corresponding to the measurement comparison observer groups.	10
Figure 6	Examples of anatomical structure segmentation: arterial vessel segmentation (A), bone segmentation (B) and skin segmentation (C).	13
Figure 7	Example of combined structure edge image in which the edges of skin (skin-colored), bone (light) and artery (red) in leg of interest are viewed (A) and projected on corresponding CT-slice (B). Example of 3D overview of combined segmented anatomical structures (C).	14
Figure 8	Schematic overview of depth measurement steps described in step 4. Blue boxes represent measurement steps and orange boxes represent in- or exclusion steps of measurement points.	16
Figure 9	Example of 3D overview of performed depth measurements. Colored lines represent measured depth according to described depth intervals presented in Table 4. Furthermore, denoted anatomical landmarks presented.	17
Figure 10	Example of graph presenting the measured minimum vessel depths. Horizontal dotted green and orange colored lines and datapoint color corresponds to depth intervals described in Table 4. Vertical dotted black lines correspond to denoted anatomical landmarks. The x-axis refers to the slice and the y-axis represents the measured depth	18

Figure 11 Overview of performed depth measurements at two locations around denoted SFA origin. Depth measurement colors correspond to depth intervals described in Table 4. 19

Figure 12 Schematic representation of the phantom with corresponding internal dimensions (A) and the created phantom used for automatic depth measurement validation (B). 20

Figure 13 Sagittal (A) and transversal (B) view of 3D reconstructed phantom with depth measurements. Depth measurement direction is presented as green lines within the 3D reconstructed figures. Measured depth is showed in the graph (C), where the x-axis refers to the slice and the y-axis represents the measured depth 21

Figure 14 Bland-Altman plot of depth measurements in the SFA. In all plots the horizontal dotted lines represent from top to bottom the upper limit of agreement, the bias and the lower limit of agreement. 23

Figure 15 Overview of difference in measured depth measured at the EIA by observer 1 (A), observer (B) and observer 3 (C) within the EIA. Selected slice differed only 3 slices, whereas measurement location differed much more. 25

Figure 16 Example of depth measurement graph in which bone structures are incorporated in the arterial segmentation and therefore depth measurements are also performed between skin and bones (A). In addition, example of slice on which multiple erroneous depth measurements are performed between bone and skin. 28

Figure 17 Example of depth measurement graph in which part of the sacrum was segmented incompletely and therefore depth measurement was performed through this bone region. (A). In addition, 30

Figure 18 Different types of Dolichoarteriopathies: A: tortuous, B: coiling and C: kinking. CCA: common carotid artery, ECA: external carotid artery and ICA: internal carotid artery.[54] 33

Figure 19 Example of a 3Mensio created segmentation of a subject with an extracranial carotid aneurysm of the right internal carotid artery (ICA). The carotid tortuosity index was calculated for every study patient as ratio of the length of the central luminal line (CLL) and the straight line length. The carotid artery was measured from skull base (A) until carotid bifurcation (B), and origin of the CCA (C). The CLL for the ICA is indicated in blue, for the common carotid artery (CCA) in red. The CLL of the total carotid artery was calculated by adding ICA and CCA CLL length. The straight distances are indicated in yellow and green. 36

Figure 20 Bland-Altman plots of tortuosity index in ICA (A), CCA (B) CA (C). In all plots the horizontal dotted lines represent from top to bottom the upper limit of agreement, the bias and the lower limit of agreement. 38

Figure 21 Bland-Altman plots of tortuosity measurements performed by observer 1 in ICA (A), CCA (C) and CA (E) and observer 2 in ICA (B), CCA (D) and CA (F). In all plots the horizontal dotted lines represent from top to bottom the upper limit of agreement, the bias and the lower limit of agreement. 40

Figure 22 Overview of incorrect alignment of exported CLL and corresponding DICOM-files (A) and incorrect exported CLL-coordinates (B). In figure A exported CLL's lie behind created segmented area. In figure B, CLL from observer one (light blue) and observer 2 (blue) follow different pathways suggesting incorrect CLL placement. 45

Figure 23 Example of depth measurements at origin of external iliac artery. 57

Figure 24 Example of depth measurements at origin of popliteal artery at the first slice on which kneecap is not visible when looking in a craniocaudal direction. 57

Figure 25 Bland-Altman plots for depth measurements in the AIE in measurements direction A (A), B (B), C (C), D (D) and E (E). Figures show comparison of measurements performed by observer 1 and 2 (Blue), observer 1 and 3 (Black) and observer 2 and 3 (Orange). In all plots the horizontal dotted colored lines represent from top to bottom the upper limit of agreement, the bias and the lower limit of agreement with corresponding to the compared measurements. 58

Figure 26 Bland-Altman plots for depth measurements in the ATA in measurements direction A (A), B (B), C (C), D (D) and E (E). Figures show comparison of measurements performed by observer 1 and 2 (Blue), observer 1 and 3 (Black) and observer 2 and 3 (Orange). In all plots the horizontal dotted colored lines represent from top to bottom the upper limit of agreement, the bias and the lower limit of agreement with corresponding to the compared measurements. 59

Figure 27 Bland-Altman plots for depth measurements in the ATP in measurements direction A (A), B (B), C (C), D (D) and E (E). Figures show comparison of measurements performed by observer 1 and 2 (Blue), observer 1 and 3 (Black) and observer 2 and 3 (Orange). In all plots the horizontal dotted colored lines represent from top to bottom the upper limit of agreement, the bias and the lower limit of agreement with corresponding to the compared measurements. 60

List of tables

Table 1	Reliability classes with corresponding ICC values as described by Koo and Li33	8
Table 2	The ICC, reliability according to the predefined ICC classes (Table 1) and CV%mean $_{for}$ interobserver agreement at the following anatomical landmarks: External Iliac artery (EIA)(n=35), Superficial femoral artery (SFA)(n=35), Anterior tibial artery (ATA)(n=34) and posterior tibial artery (PTA)(n=33). Values $_{between}$ brackets are the 95% confidence intervals of the calculated ICC. CV%mean is divided into three subgroups: observer 1 vs 2, observer 1 vs 3 and observer 2 vs 3.	9
Table 3	Overview of attributes that define the transmitted pixel array of a two-dimensional image plane. Table is derived from DICOM PS3.3 2020a - Information Object Definitions from NEMA.[41]	12
Table 4	Overview of depth measurement colors with corresponding measured depth intervals (mm).	15
Table 5	Mean, median, minimum and maximum for the measured depth (mm) and difference between real and measured depth (mm) (n=64)	21
Table 6	Overview of successful segmentation results and automatic depth measurement time. Time is viewed with “HH:MM:SS” notation and values between brackets show minimum and maximum measurement time.	22
Table 7	The ICC, reliability according to the predefined ICC classes (Table 1) and CV%mean $_{for}$ interobserver agreement at the AFS (n=35). Values between brackets are the 95% confidence intervals of calculated ICC.	23
Table 8	Curvature and torsion groups with corresponding cutoff values.	37
Table 9	The ICC, reliability according to the predefined ICC classes (Table 1), lower limit of agreement (LLA), upper limit of agreement (ULA) and CV%mean $_{for}$ interobserver agreement (n=174). Values between brackets are the 95% confidence intervals of the calculated ICC.	38
Table 10	The ICC, reliability according to the predefined ICC classes (Table 1), lower limit of agreement (LLA), upper limit of agreement (ULA) and CV%mean $_{for}$ intraobserver agreement (n=35). Values between brackets are the 95% confidence intervals of the calculated ICC.	39
Table 11	Baseline characteristics of study population.	41

Table 12 CA median TI, curvature and torsion values in cases with ECAA compared with own contralateral CA. Values between brackets are minimum and maximum values of TI, curvature and torsion. 42

Table 13 CA median TI, curvature and torsion values in cases with ECAA compared with carotid arteries from control group. Values between brackets are minimum and maximum values of TI, curvature and torsion. 42

Table 14 Correlation of measured TI, low, medium and high curvature and low and high torsion (n = 155). Values between brackets are calculated p-values. 42

Chapter 1: Introduction

According to the World Health Organization (WHO), around 18 million people died from the effects of cardiovascular disease (CVD) in 2016, an estimated 31% of all global deaths.[1,2] In Europe, 45% of all deaths are caused by CVD.[3,4] CVD refers to a group of disorders of the heart and blood vessels, such as coronary heart disease, cerebrovascular disease and peripheral vascular disease, the latter of which is considered the most prevalent cardiovascular condition globally.[1–3] The majority of fatalities are caused by vascular obstructions leading to cardiovascular events such as myocardial infarct, ischemic stroke or peripheral artery disease (PAD).[1,3,4]

PAD usually affects the lower-extremity arteries and its development site is known to correlate strongly with known risk factors.[5–11] In all cases, corner stone of PAD treatment is to address existing risks. However, in some cases vascular intervention is planned to reduce symptoms. Endovascular interventions intent to revascularize lower-extremity segments by ballooning the plaque against the vessel wall.[9,12] Although percutaneous recanalization is a minimal invasive technique, it is also combined with limitations like restenosis, and complications like bleeding, thrombo-embolism and infection.[13–15] To overcome these limitation, currently non-invasive PAD treatment techniques are explored. Yet, such transcutaneous techniques can have a specific depth range in which the technology works and for treatment of atherosclerotic plaques therefore the depth of the target artery must therefore be within this range. Consequently, to determine whether a patient with PAD is eligible for such transcutaneous treatment, it is important to know the depth of the arteries in the lower extremities. Therefore, the first aim of this thesis was to develop a technique that can automatically measure the depth of lower-extremity arteries.

Although in the case of lower-extremity PAD the correlation between risk factors and development site is known, it is not the case in abnormal phenotypes of the carotid arteries (CA). Still little is known about the relationship between these abnormalities and for example the development of cerebral ischemia (*i.e.* transient ischemic attack or stroke). Some studies have found that the presence of cardiovascular atherosclerotic risk factors are comparable in patients with and without present CA abnormalities.[61,62] Since the anatomical variety in CA deviation is large, it is important to find out the similarities and/or difference in geometry in CAs. Therefore, the second aim of this thesis was to address the clinical implication of CA geometry expressed in tortuosity index (TI), curvature and torsion.

1.1 Research aims

In order to achieve the two stated research aims, the following research questions have been defined:

1. *Can the arterial depth of lower-extremity arteries in patients suffering from peripheral arterial disease be measured using an automatic measurement technique?*
2. *What is the correlation between tortuosity index and, curvature and torsion of the carotid artery?*

1.2 Outline

Figure 1 presents a schematic overview of the thesis outline. In chapter 1 the subject and research questions are introduced. Chapter 2 discusses all aspects of the development of the depth measurement technique. First, the topic and reason for the development of the technique is

discussed (section 2.1, 2.2 and 2.3). Subsequently, method and results of manual measurement interobserver agreement, development of the automatic depth measurement techniques along with technique requirements and validation and method and results of agreement of manual and automatic performed measurements was discussed (section 2.4, 2.5 and 2.6). Last sections of chapter 2 discuss outcomes of all afore mentioned studies and a final conclusion (section 2.7 and 2.8). Chapter 3 describes the CA TI, curvature and torsion correlation assessment study. This chapter is divided into the following parts: introduction of subject and research aims(section 3.1, 3.2 and 3.3), description of used method (section 3.4), results (section 3.5), discussion on study outcomes and final conclusion (section 3.6 and 3.7). Finally, important outcomes and future perspectives will be summarized in chapter 4.

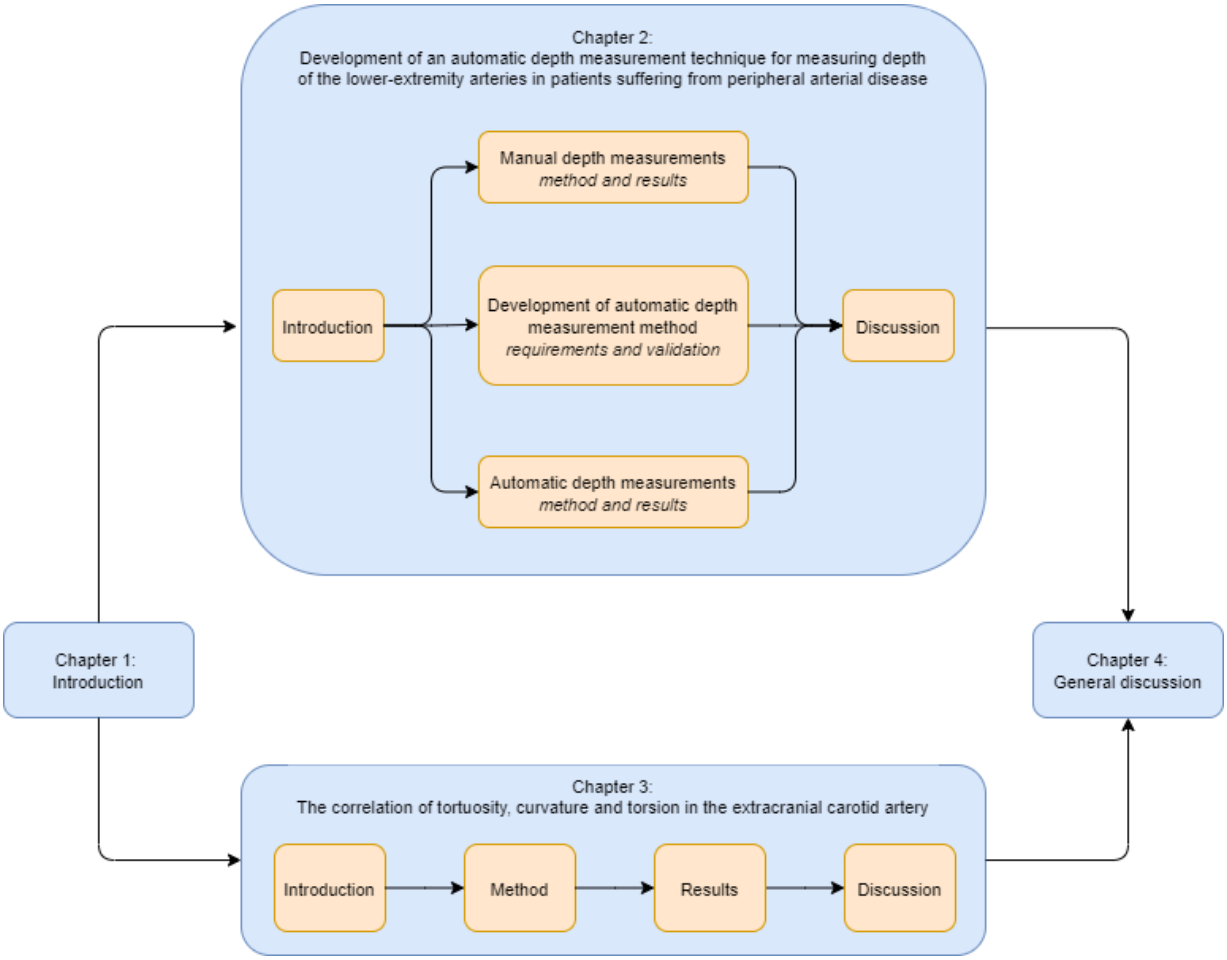

Figure 1: Schematic overview of thesis outline

Chapter 2: Development of an automatic depth measurement technique for measuring depth of the lower-extremity arteries in patients suffering from peripheral arterial disease

2.1 Clinical background

PAD refers mainly to obstructions of the lower-extremity arteries involving all arteries distal from the aortic bifurcation. It's prevalence and incidence is highly age-related, around 10%-20% of the general population aged between 55 and 65 years is affected by PAD.[19,20] Most vascular obstructions are caused by the formation of atherosclerotic plaques or thrombi. Those atherosclerotic plaques are the result of atherosclerotic lesions which are formed by infiltration of macrophages, accumulation of cholesterol and connective tissue components, proliferation of smooth muscle cells and formation of thrombus.[8,21] The earliest visible atherosclerotic lesions are so called fatty streaks which are formed within the intimal layer of the artery by accumulation of lipid-laden foam cells and macrophages that provoke chronical inflammation at susceptible sites in the walls of arteries.[8,21–23] These fatty streaks can eventually turn into fibrous plaques, some of which eventually also have an increased chance of rupturing which can cause thrombosis or stenosis.[8,21–23] An overview of the different stages of atherosclerotic plaque formation is shown in Figure 2.

In most cases, PAD appears to be a multi-segmental condition of which the development location strongly correlates with present risk factors, such as smoking, hypertension, hypercholesterolemia and diabetes.[6–11] Figure 3 presents an overview of the association of risk factors with location of atherosclerotic target lesions. In all cases, corner stone of PAD treatment is to address existing risks through, for example, cardiovascular risk management; cholesterol lowering drugs, smoking cessation and blood pressure control.[9,10,24] Depending on the classification and symptom severity, it may be decided to advise supervised exercise therapy, or plan an (endo-) vascular intervention to reduce symptoms. Invasive treatment options include endovascular, surgical or hybrid (both) interventions. Open surgical interventions intent to revascularize lower-extremity segments by either bypass surgery, and segmental or remote endarterectomy [9,24] Because open vascular surgery is combined with high morbidity and mortality and endovascular (mini-invasive) techniques improved the last decade, there was a major shift from open to endovascular therapy.[14] Endovascular interventions intent to revascularize lower-extremity segments by ballooning the plaque against the vessel wall (percutaneous balloon angioplasty).[9,12] Additionally, to improve patency, drug (paclitaxel) coated balloons, or balloon and self-expandable stents can be used, depending on plaque characteristics and location. Although percutaneous recanalization is a minimal invasive technique, it is also combined with limitations like restenosis, and complications like bleeding, thrombo-embolism and infection.[13–15]

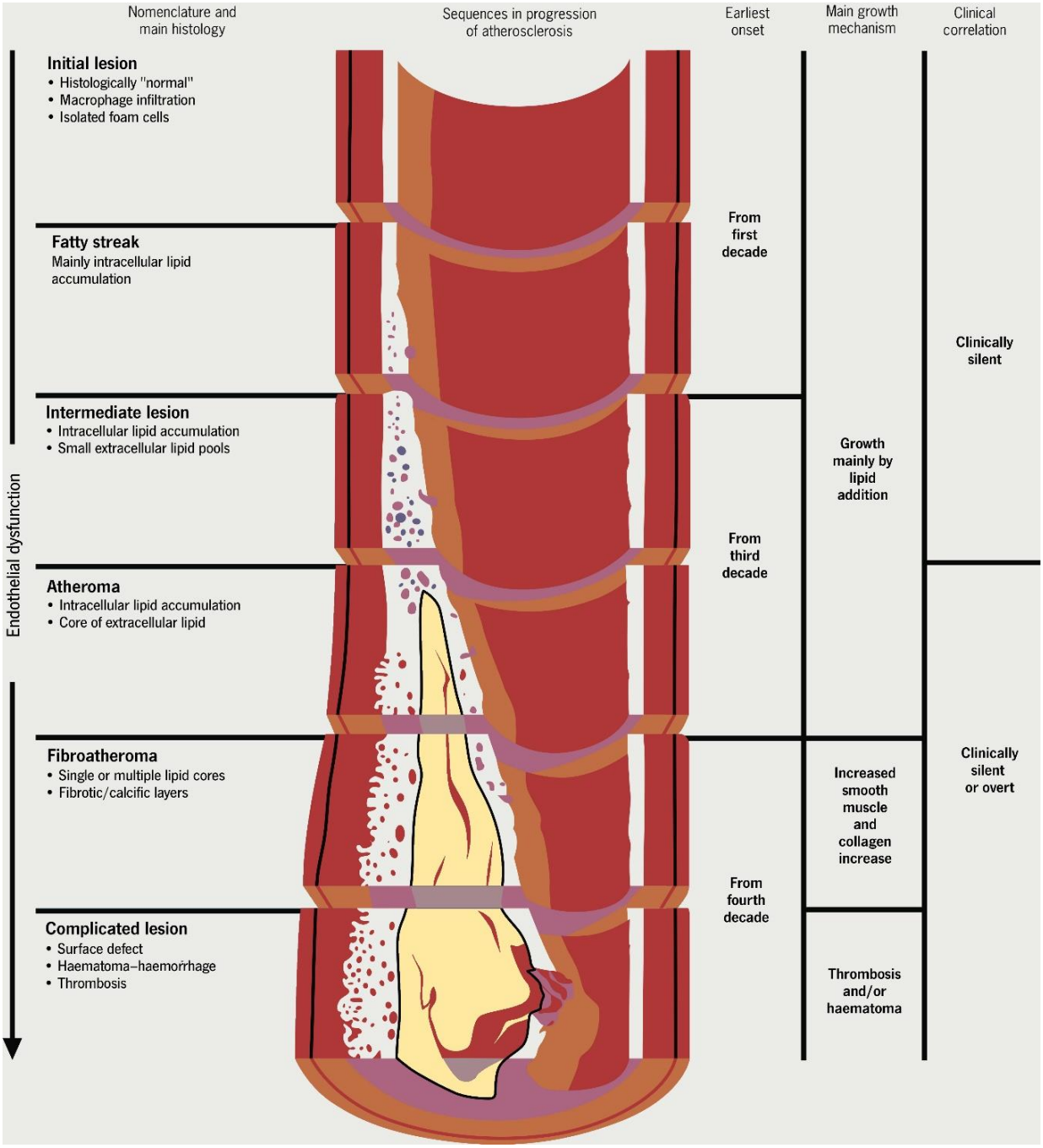

Figure 2: Overview of progression of atherosclerosis starting at the initial lesion and ending at the complicated lesion.[25]

Currently, non-invasive PAD treatment techniques are explored. High-intensity focused ultrasound (HIFU) is a potential non-invasive treatment technique that uses ultrasonic waves with an intensity larger than 5 W/cm^2.[16] The HIFU beam can be accurately focused on target lesions within a small focal volume. This leads to an increase in local tissue temperature, resulting in localized tissue damage and necrosis.[16,17,26–29] This then causes an acute inflammatory response, including cellular regeneration, proliferation, migration, and debris removal.[17,18] Recent animal studies have shown that HIFU is a promising technique to crush atherosclerotic plaques.[29–31] However, transcutaneous techniques like HIFU can have a specific depth range in which the technology works. For the treatment of atherosclerotic plaques with HIFU, the depth of the target artery must be within this range. Because the depth of the lower extremity arteries will be different for each patient due to anatomical variability, it is important to develop an automatic technique for performing depth measurements. Therefore, the aim of this study is to develop a technique that can automatically measure the depth of lower-extremity arteries.

2.2 Research questions

The main research question that will be answered in this chapter of the thesis is described below:

Can the arterial depth of lower-extremity arteries in patients suffering from peripheral arterial disease be measured using an automatic measurement technique?

To answer the main question, the following supporting research questions have been formulated:

1. *Are manual measurements of lower-extremity arteries reliable and reproducible?*
2. *Can an automatic measurement method be developed for measuring arterial depth?*
3. *What is the interobserver agreement and reliability in lower-extremity artery depth measurements while comparing a manual and automatic measurement technique?*

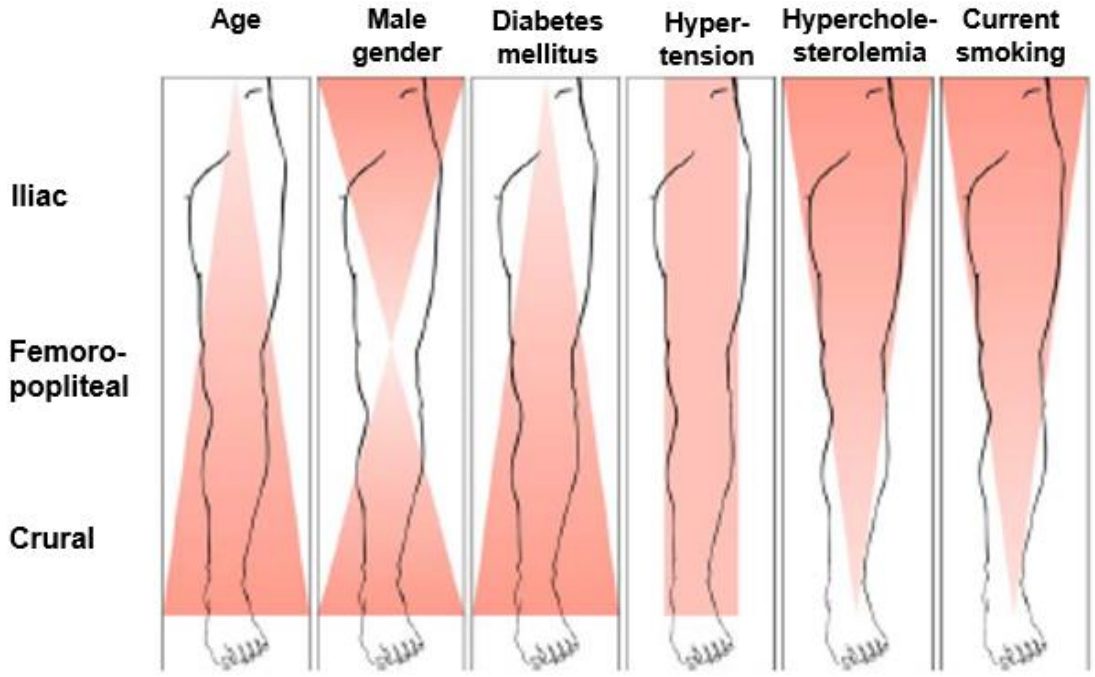

Figure 3: Association of risk factors with the level of atherosclerotic target lesions. Red overlay on the anatomic cartoon illustrates the association of risk factor with pattern of atherosclerotic lesions. Image and caption adapted from Diehm et al.[6]

2.3 Aim of the study

The aim of the study is to develop a technique that can automatically measure the distance between lower-extremity arteries and the skin in patients with peripheral artery disease. This objective is subdivided into various subgoals that are described below:

1. *Determine the reliability and reproducibility of manual depth measurement method.*
2. *Determine if an automatic depth measurement method can be developed.*
3. *Assess technique variability and reproducibility when comparing manual and automatic depth measurement technique of lower-extremity arteries.*

2.4 Manual measurements

2.4.1 Method

2.4.1.1 Patient selection and image technique

The dataset for depth measurements exists of 35 subjects of which all were diagnosed with PAD. Subjects underwent a computed tomography angiography (CTA) scan according to regular protocols. All CTA studies were performed using a 128-slice or IQon Spectral CT scanner (Philips Brilliance; Philips Medical Systems, Best, The Netherlands). All lower extremity arteries were at least visualized from aortic bifurcation to the plantar arteries. Slice thickness was 3mm, collimation 64x0.625 and pitch 0.797. Radiation exposure parameters were 120 kilovolt and 120-180 milliampere second. The field of view was set per patient. Injection of 144 milliliter intravascular contrast (Lopromide, Schering, Berlin, Germany) was followed by a saline bolus of 60 milliliter, both at a flow rate of 6.0 milliliter per second.

2.4.1.2 Depth measurements

Three independent observers (vascular surgeon, researcher and graduation student at department of vascular surgery) performed manual depth measurements using a picture archiving and communication system (PACS) (Sectra group, Linköping, Sweden). To ensure measurement comparability, measurements were performed at the following four predefined anatomical landmarks: origin of (1) external iliac artery (EIA), (2) superficial femoral artery (SFA), (3) anterior tibial artery (ATA) and (4) posterior tibial artery (PTA). In addition, as most of the selected anatomical landmarks were visible on multiple transversal slices, depth measurements were performed on the most proximal transversal slice in which the origin of the anatomical landmark of interest was seen when looking in a craniocaudal direction. At each anatomical landmark, five following depth measurements are performed; (A) from dorsal arterial wall to ventral skin, (B) from ventral arterial wall to dorsal skin, (C) from lateral arterial wall to medial skin, (D) from medial arterial wall to lateral skin and (E) the apparently shortest distance from the contralateral side of the vessel wall to the skin. All measurements were performed by drawing a straight line at the above-mentioned directions. An example of all measurement directions at the external iliac artery is shown in Figure 4 and overview of the complete measurement protocol can be found in Appendix A.

2.4.1.3 Statistical analysis

First, inter-observer agreement was assessed by calculating the Intraclass Correlation Coefficient (ICC) to indicate measurement agreement and reliability. Second, measurement agreement was visualized and Coefficient of Variation (CV) was determined.

Measurement reliability and agreement

First, ICC was calculated to indicate measurement agreement and reliability. ICC for measurement comparison is the two way random effect convention, which is based on single measurement absolute agreement and determined with the equation as described by McGraw and Wong[32].[33] The equation is described below:

$$ICC = \frac{MS_R - MS_E}{MS_R + (k-1) + \frac{k}{n}(MS_C - MS_E)} \quad \textbf{(1)}$$

Where MS_R is the mean square for measurements, MS_E the mean square for error, MS_C the mean square for observers, n the number of measurements and k the number of observers. All ICC values were calculated using SPSS statistical package version 25 (IBM SPSS for windows, Armonk, NY). The ICC returns a value between zero and one, where zero corresponds to circumstances where all variability is caused by measurement errors and one means there are no measurement errors at all.[34] For this study reliability classes as suggested by Koo and Li[33] have been used. An overview of used reliability classes with corresponding intraclass correlation coefficient is shown in Table 1.

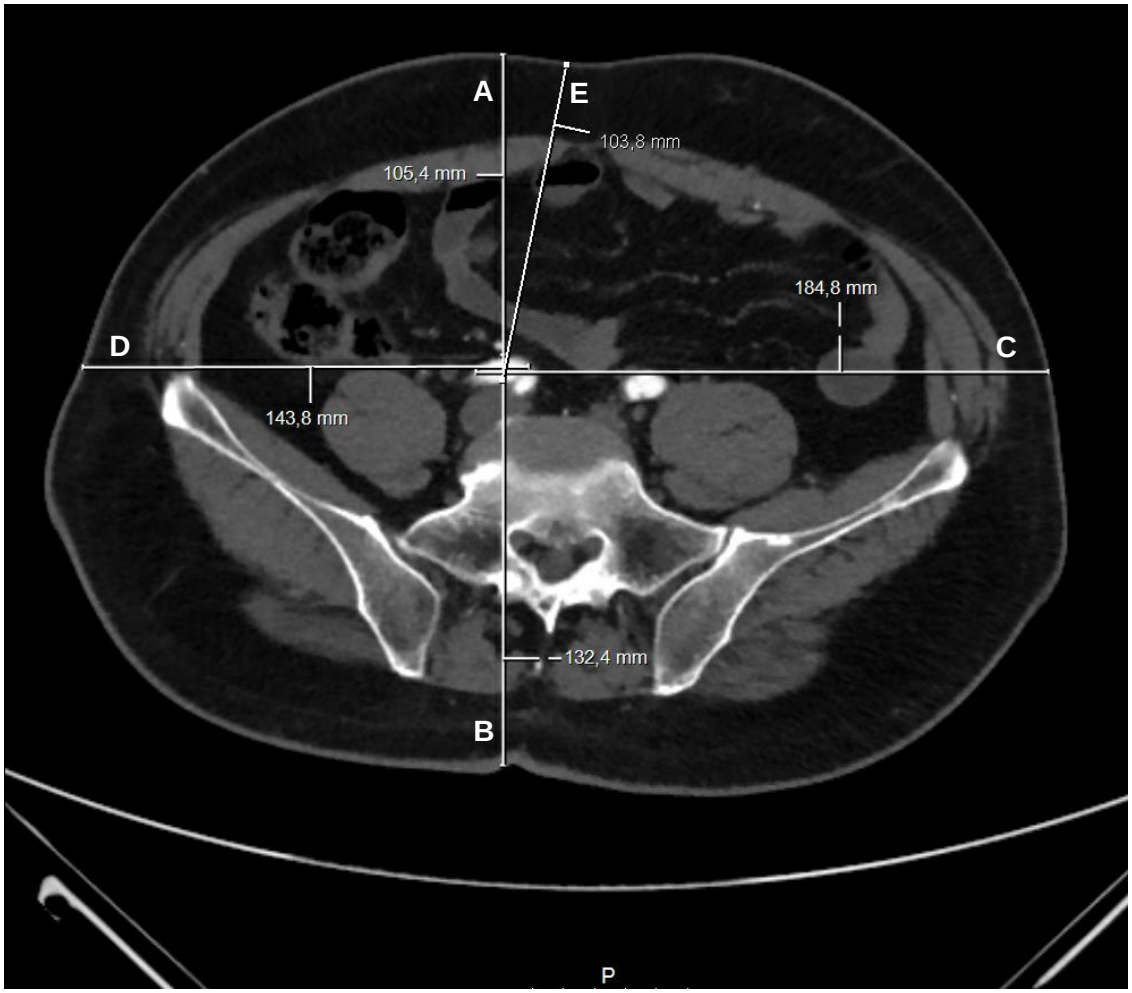

Figure 4: Example of measurement performed at the external iliac artery. Measurement direction A, B, C, D and E correspond to five measurement directions described in section 2.4.1.2.

Table 1: Reliability classes with corresponding ICC values as described by Koo and Li[33].

Reliability	Intraclass correlation class value
Excellent	ICC ≥ 0.9
Good	0.75 ≤ ICC < 0.9
Moderate	0.5 ≤ ICC < 0.75
Poor	ICC < 0.5

Second, measurement agreement was visualized using Bland-Altman plots in which the difference between measurements is plotted against their mean.[34,35] Furthermore, distribution and limits of agreement can be assessed from created plots.

Coefficient of Variation

The CV was used to assess the extent of variability in relation to the mean absolute agreement value. This coefficient is defined as the 95% probability that the outcome will be below the difference of two measurements and is calculated using the following equation:

$$CV = 1.96 \times SD \quad \textbf{(2)}$$

Where *SD* the standard deviation for single differences in subjects.[36,37] To ensure measurement outcomes are comparable at different locations, CV was normalized to a percentage of the mean distance value ($CV_{\%mean}$).[37,38]

2.4.2 Results

Each observer performed 685 depth measurements of possible 700 depth measurements. Table 2 presents an overview of interobserver agreement and measurement variability. All measurements performed at the SFA and PTA show excellent reliability. Furthermore, measurements performed at the ATA only scored good or moderate reliability. Highest precision and lowest $CV_{\%mean}$ values were seen for measurements performed within the SFA. On the other hand, lowest precision and highest $CV_{\%mean}$ values where seen in the measurements performed at the PTA. Moreover, the calculated $CV_{\%mean}$ values for the measurements of observer 2 and 3 were generally the lowest everywhere. Figure 5 shows the created Bland-Altman plots for measurements performed within the SFA. These graphs show a comparison of the measurement results per measurement direction of observer 1 and 2 (blue), observer 1 and 3 (black) and observer 1 and 3 (orange). All plots show no systematic bias for all three measurement comparisons. An overview of the created Bland-Altman plots for all measurements performed in the described measurement directions at the different anatomical landmarks can be found in Appendix B.

Table 2: The ICC, reliability according to the predefined ICC classes (Table 1) and $CV_{\%mean}$ for interobserver agreement at the following anatomical landmarks: External Iliac artery (EIA)(n=35), Superficial femoral artery (SFA)(n=35), Anterior tibial artery (ATA)(n=34) and posterior tibial artery (PTA)(n=33). Values between brackets are the 95% confidence intervals of the calculated ICC. $CV_{\%mean}$ is divided into three subgroups: observer 1 vs 2, observer 1 vs 3 and observer 2 vs 3.

Measurement		ICC	Reliability	$CV_{\%mean}$		
				1 vs 2	1 vs 3	2 vs 3
EIA (n=35)	A	0.987 (0.977 – 0.993)	Excellent	6.06%	6.36%	2.89%
	B	0.988 (0.979 – 0.993)	Excellent	2.80%	3.15%	2.83%
	C	0.879 (0.785 – 0.935)	Good	7.45%	6.53%	4.18%
	D	0.932 (0.879 – 0.964)	Excellent	11.06%	8.08%	5.82%
	E	0.955 (0.910 – 0.977)	Excellent	10.43%	8.29%	6.07%
SFA (n=35)	A	0.989 (0.980 – 0.994)	Excellent	7.62%	8.22%	2.98%
	B	0.996 (0.993 – 0.998)	Excellent	1.68%	1.57%	0.91%
	C	0.992 (0.985 – 0.996)	Excellent	1.74%	1.31%	1.23%
	D	0.988 (0.980 – 0.994)	Excellent	3.18%	3.88%	2.04%
	E	0.956 (0.909 – 0.978)	Excellent	15.74%	14.37%	6.75%
ATA (n=34)	A	0.674 (0.447 – 0.821)	Moderate	4.36%	4.43%	3.56%
	B	0.878 (0.793 – 0.933)	Good	8.02%	21.54%	22.95%
	C	0.815 (0.528 – 0.919)	Good	12.73%	13.28%	4.88%
	D	0.651 (0.319 – 0.827)	Moderate	17.83%	18.15%	8.16%
	E	0.610 (0.286 – 0.799)	Moderate	17.79%	18.22%	9.45%
PTA (n=33)	A	0.982 (0.952 – 0.992)	Excellent	3.52%	4.30%	2.74%
	B	0.992 (0.979 – 0.997)	Excellent	3.03%	3.33%	1.62%
	C	0.987 (0.972 – 0.993)	Excellent	2.67%	2.83%	2.43%
	D	0.920 (0.754 – 0.967)	Excellent	4.43%	6.85%	5.48%
	E	0.953 (0.908 – 0.976)	Excellent	5.90%	5.99%	7.31%

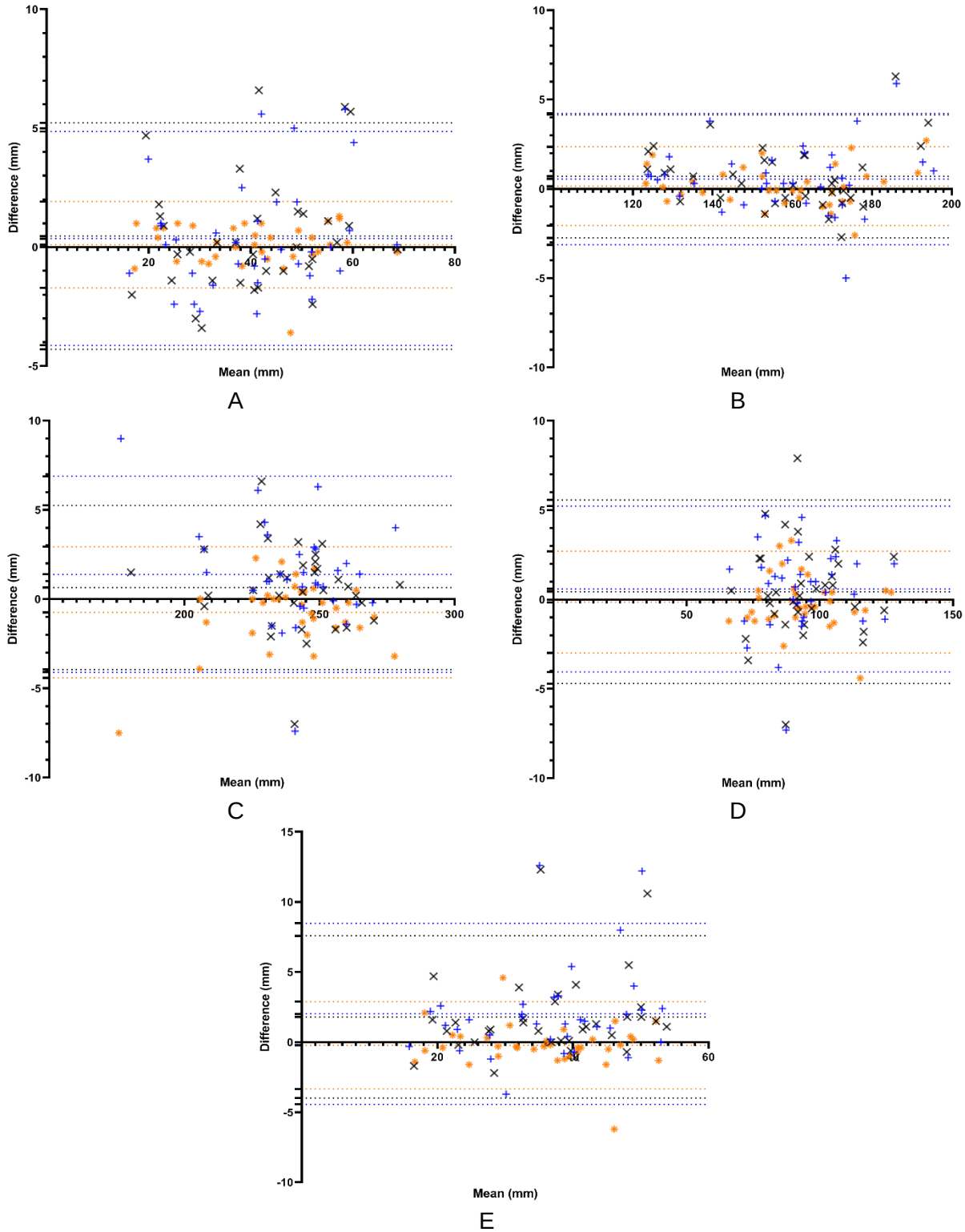

Figure 5: Bland-Altman plots for depth measurements in the AFS in measurements direction A (A), B (B), C (C), D (D) and E (E). Figures show comparison of measurements performed by observer 1 and 2 (Blue), observer 1 and 3 (Black) and observer 2 and 3 (Orange). In all plots the horizontal dotted colored lines represent from top to bottom the upper limit of agreement, the bias and the lower limit of agreement with corresponding to the measurement comparison observer groups.

2.5 Development of an automatic depth measurement technique

The developed automatic depth measurement technique exists of 4 different steps to measure arterial depth of which some require user input. First, CTA scans in Digital Imaging and Communications in Medicine (DICOM) format are loaded and transformed from DICOM image coordinate system to the patient-based coordinate system. Second, user indicates predefined landmarks and masks CT table. The vascular tree, skeleton and skin are then segmented, after which the technique calculates the distance between segmented vessels and skin. The technique excludes depth measurements of which the measurement direction passes through bone structures. The result of all performed depth measurements are displayed along with created segmentations in a 3D overview. In addition, all measured distances are displayed in a graph where measuring points can be selected to view the corresponding segment and depth measurements performed.

All steps mentioned above have been developed and implemented in MATLAB (Version R2019b, MathWorks, Natick, Massachusetts, USA). In the following sections the depth measurement technique requirements (section 2.5.1) and depth measurement algorithm steps (section 2.5.2), will be discussed. Furthermore, the maximum measurement deviation of the developed automatic measurement algorithm is validated (section 2.5.3) and the technique is compared with manual performed measurements (section 2.6). To conclude, salient features and results from the above sections are discussed in a general discussion (2.7).

2.5.1 Requirements

As described in section 2.3, the main objective of this study is to develop an automatic depth measurement technique able to automatically measure distance between lower extremity arteries and skin. To test the developed automatic depth measurement technique, depth measurement requirements were determined in advance. This section will address the minimal requirements for automatic depth measurements.

Segmentation of tissue structures of interest

To develop a successful depth measurement technique, the measurement algorithm must be able to segment the lower extremities, bones and skin separately. In addition, it is important that only the structure of interest is included into the segmentation, as otherwise incorrect measurements can be performed. For the lower extremity arterial tree segmentation, the following properties are important: 1. lower extremity arteries are segmented from aortic bifurcation to plantar arteries and 2. small arterial side branches or capillaries do not have to be segmented. However, if the origin of the ATA and ATP is segmented, but the segmentation does not extend to the plantar arteries, this is also considered sufficient. For bone segmentation, it is important that the cortical bone is segmented and spongy bone regions are included within the segmentation. Incomplete bone segmentation can result in erroneous depth measurements that cross bone structures, since these measurements do not reflect clinical use of transcutaneous techniques such as HIFU. Finally, a selected skin segmentation is important so that other objects, such as blankets or the mattress of the CT table, are not included in depth measurements.

Measurement deviation

HIFU has a therapeutic depth range between 30 and 40mm.[39] In addition, a range of 3mm is described to increase the therapeutic range of HIFU.[39] Therefore, a maximum measurement deviation of 3mm is considered sufficient.

Table 3: Overview of attributes that define the transmitted pixel array of a two-dimensional image plane. Table is derived from DICOM PS3.3 2020a - Information Object Definitions from NEMA.[41]

Attribute name	Attribute description
Pixel spacing	Physical distance in the patient between the center of each pixel, specified by a numeric pair - adjacent row spacing (delimiter) adjacent column spacing in mm.
Image orientation (patient)	The direction cosines of the first row and the first column with respect to the patient.
Image position (patient)	The x, y, and z coordinates of the upper left hand corner (center of the first voxel transmitted) of the image, in mm.
Slice thickness	Nominal slice thickness, in mm.
Slice location	Relative position of the image plane expressed in mm.

Measurement duration time

Factors that influence depth measurement time are the number of slices in the DICOM series, the extent to which the arterial vascular tree is segmented and patient size. As a result, elapsed time will differ between cases. In addition, duration must be limited to make the technology developed suitable for clinical use. Therefore, a maximum measurement time of 15 minutes is considered acceptable.

2.5.2 Depth measurement algorithm

In this section we will look in more detail at the steps of the developed algorithm mentioned at the beginning of section 2.5. All steps can be completed individually, but must always be carried out in the order described to reach the end result.

Step 1: Preparing DICOM files for depth measurements

The first depth measurement step ensures DICOM files are loaded and prepared for depth measurements. For this study, CTA studies with 3mm slice thickness have been used. After loading the DICOM files, the coordinate system of the DICOM files is converted from the image coordinate system to the patient-based coordinate system using MATLABs *imwarp* function.[40] This function uses the information from the image plane module which can be found in the DICOM header information and consists of the following components: pixel spacing, Image orientation, Image Position, slice thickness and slice location.[41] An overview of these components along with corresponding description is presented in Table 3.

Step 2: Define anatomical landmarks

Within the second step, the user indicates the following six predefined anatomical landmarks: origin of common iliac artery (CIA), EIA, SFA, popliteal artery visualized on the first slice on which the patella is not visible when looking in a craniocaudal direction (Apop), ATA and PTA. In addition, the user is asked to mask the CT table. Masking the CT table is performed manually by drawing an region of interest around the table and prevents the table from being included in a segmentation of an anatomic structure.

Step 3: Segment anatomical structures of interest and determine structure edge

Next, the arterial vascular tree, skeleton and skin are segmented. First, the contrast in the arterial vascular tree is increased with an enhanced Frangi filter.[42,43] This is a tubular shaped filter of varying sizes which searches for bright tubular shaped structures within the CT-images and requires input of two main parameters: σ and τ. Parameter σ represents the radius of the Gaussian tubular shaped structure and τ controls the output uniformity. The resulting enhanced vessel contrast image is segmented by selecting the largest connected region created using MATLAB's *bwlabeln* function with a three-dimensional 26 connected neighborhood filter.[44] Arterial segmentation outcome is checked by the user. If the resulting arterial segmentation is not satisfactory, segmentation steps are performed again. In addition, more regions can be included in the 26 connected neighborhood filter. An overview of a successful arterial segmentation is shown in Figure 6A.

Subsequently, the bones and skin are segmented. For both bone and skin segmentation, similar segmentation method is used to create both segmentations based on a predetermined threshold value. Predetermined threshold value are set according to Hounsfield units for bones and soft tissue.[45] In the case of bone segmentation, the contrast in the arteries is first masked using the segmented arterial tree because the used contrast medium increases Hounsfield unit to bone levels. Masking therefore prevents part of the arterial vascular tree from being included in the bone segmentation. The largest region in the segmentations is selected using the *bwlabeln* function described above. Figure 6B and Figure 6C present an overview of a successful bone and skin segmentation.

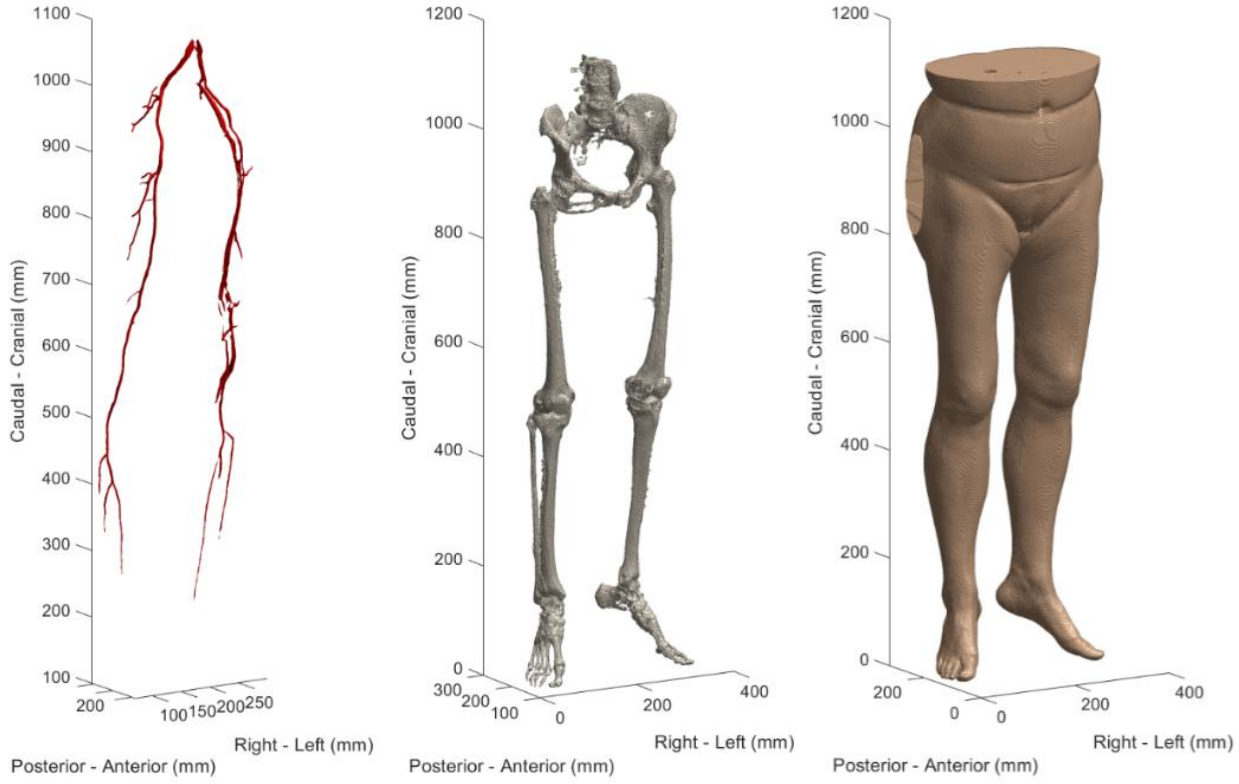

Figure 6: Examples of anatomical structure segmentation: arterial vessel segmentation (A), bone segmentation (B) and skin segmentation (C).

Finally, the developed technique determines segmentation edges separately. These edges are combined in an image file in which they can still be distinguished. Furthermore, contralateral leg is masked to reduce measurement time. In the final 3D-overview, however, both legs are visualized. Figure 7 presents an example of determined anatomic structure edges and combined 3D overview.

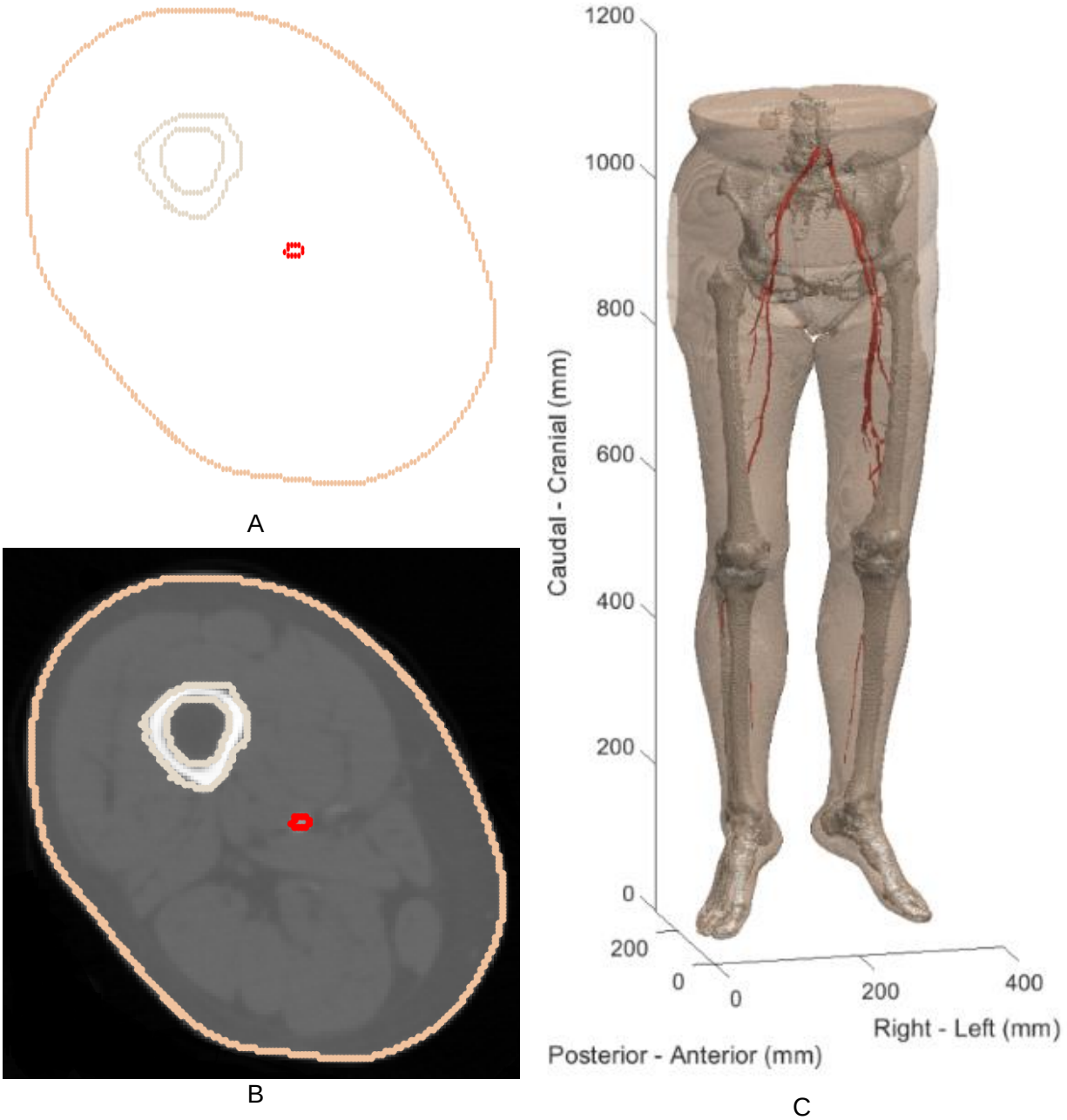

Figure 7: Example of combined structure edge image in which the edges of skin (skin-colored), bone (light) and artery (red) in leg of interest are viewed (A) and projected on corresponding CT-slice (B). Example of 3D overview of combined segmented anatomical structures (C).

Table 4: Overview of depth measurement colors with corresponding measured depth intervals (mm).

Color	Depth (mm)
Green	30 ≤ depth ≤ 40
Orange	27 ≤ depth < 30 or 40 < depth ≤ 43
Red	depth < 27 or depth > 43

Step 4: Automatic depth measurements

Now that the anatomical structure are segmented and their edge coordinates are determined, the developed depth measurement technique calculates shortest distance between skin and contralateral arterial wall on each transversal slice. All automatic depth measurement steps are shown schematically in Figure 8 and are described below.

First, centroid of vascular segmentation and bone regions are determined. If multiple segmented arterial branches are present within the selected transversal slice, centroid will be determined for each branch. Moreover, if vascular centroid is positioned within bone region, centroid is excluded for further analysis. Next, the Pythagorean theorem is used three times to calculate distance between certain points. First, the radius of the artery which is considered equal to the distances between arterial centroid and arterial edge coordinates is determined. To ensure the developed technology performs depth measurements for each within the slice present arterial branches separately, only arterial edge coordinates within 6mm of the centroid are selected. This maximum radius of 6mm is set according to the largest arterial radius as described by Lorbeer et al[46]. Second, the distances between the centroid and skin coordinates are calculated. The technique selects 50% lowest measured depths and verifies whether the measurement passes a bony region. If this is the case, the corresponding point on the skin edge is excluded from further analysis. Only if it appears that all selected measurements pass a bony region, the remaining half of the performed measurements are analyzed. At last, the Pythagorean theorem is used to calculate the distance between the remaining arterial and skin edge coordinates. The minimum arterial depth is then found by searching all these measured distances for the depth closest to the radius of the artery, combined with the shortest measured distance between the centroid of the artery and the skin.

Depth measurement results

The developed technology initially gives the user an overview of the measured depths in two different figures. First, a 3D overview presents the combined segmentation along with denoted anatomical landmarks and provides insight into the measured shortest distances and their measurement direction (Figure 9). Second, all measured depths are viewed in a graph (Figure 10). However, this graph only provides an overview of the arterial depth and no information about the measurement direction. Therefore, depth measurement can be selected within the graph to open corresponding slices along with all performed measurements and their direction (Figure 11).

In all figures the measurements are shown in a color that correspond to measured depths within therapeutic range of HIFU (green) or ±3mm uncertainty of therapeutic range (orange) and outside the described range (red). Table 4 shows an overview of measurement colors along with corresponding depth ranges. Furthermore, denoted anatomical landmarks and defined measurement ranges are included in the depth measurement graph.

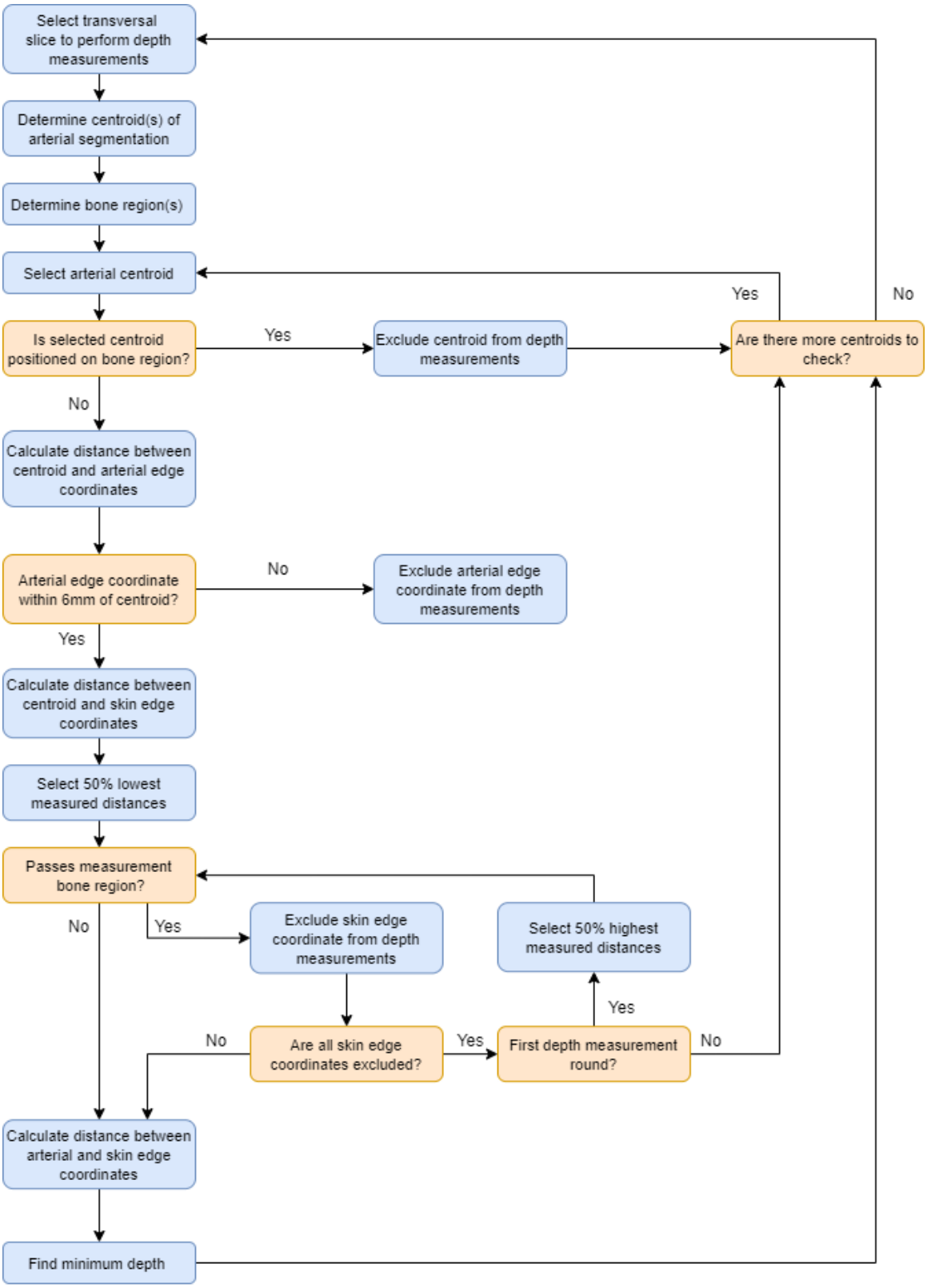

Figure 8: Schematic overview of depth measurement steps described in step 4. Blue boxes represent measurement steps and orange boxes represent in- or exclusion steps of measurement points.

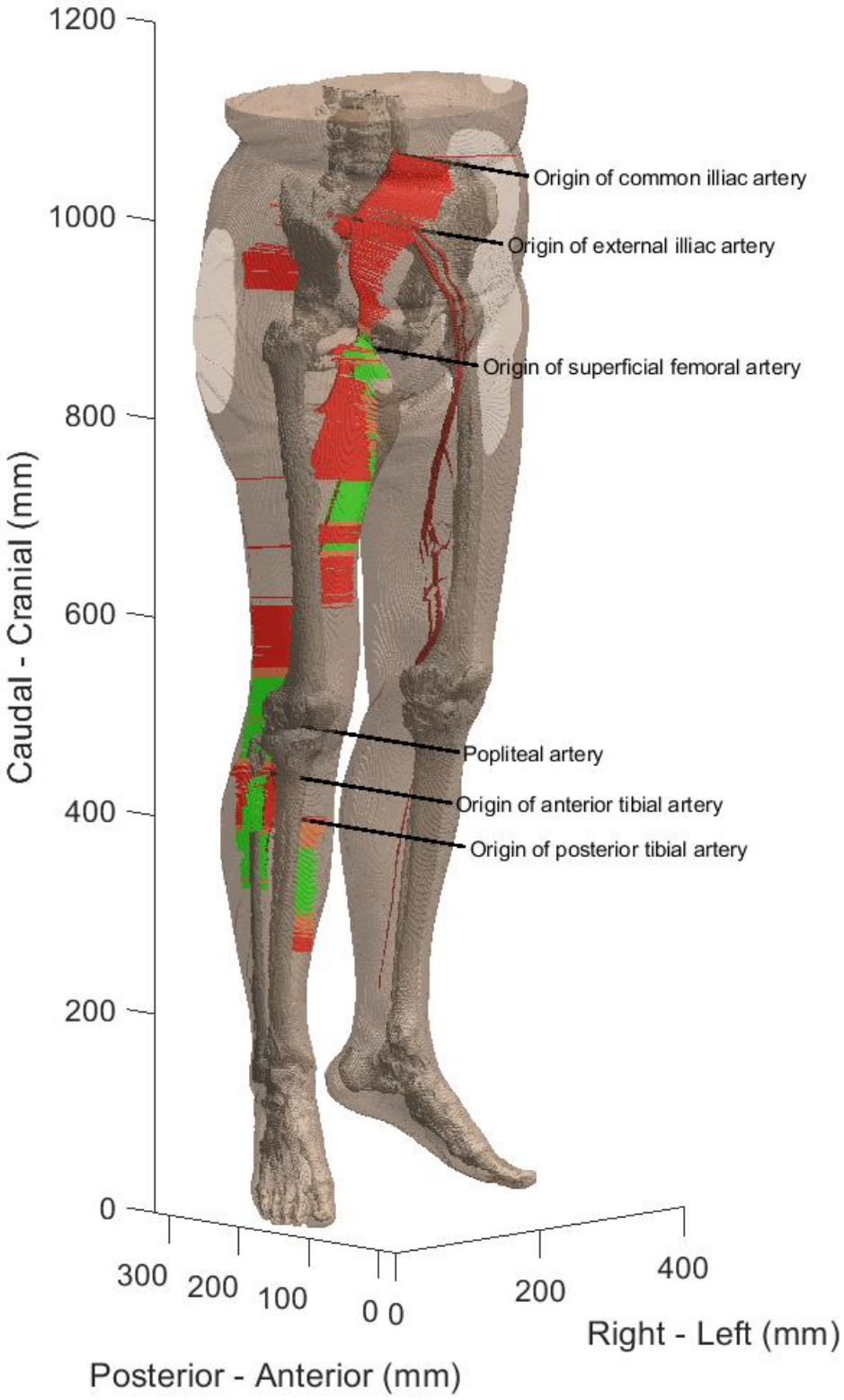

Figure 9: Example of 3D overview of performed depth measurements. Colored lines represent measured depth according to described depth intervals presented in Table 4. Furthermore, denoted anatomical landmarks presented.

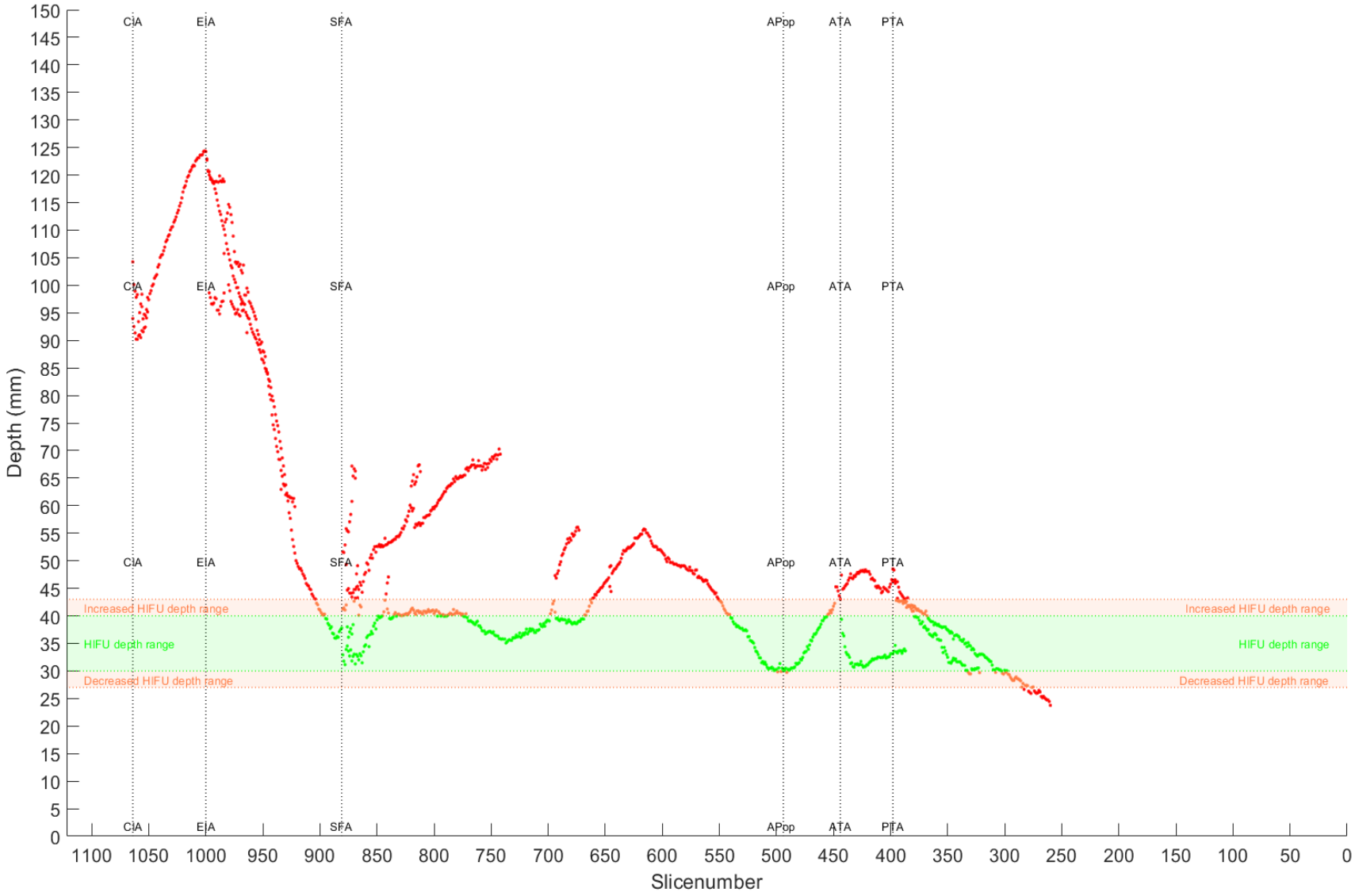

Figure 10: Example of graph presenting the measured minimum vessel depths. Horizontal dotted green and orange colored lines and datapoint color corresponds to depth intervals described in Table 4. Vertical dotted black lines correspond to denoted anatomical landmarks. The x-axis refers to the slice and the y-axis represents the measured depth(s) on corresponding slice.

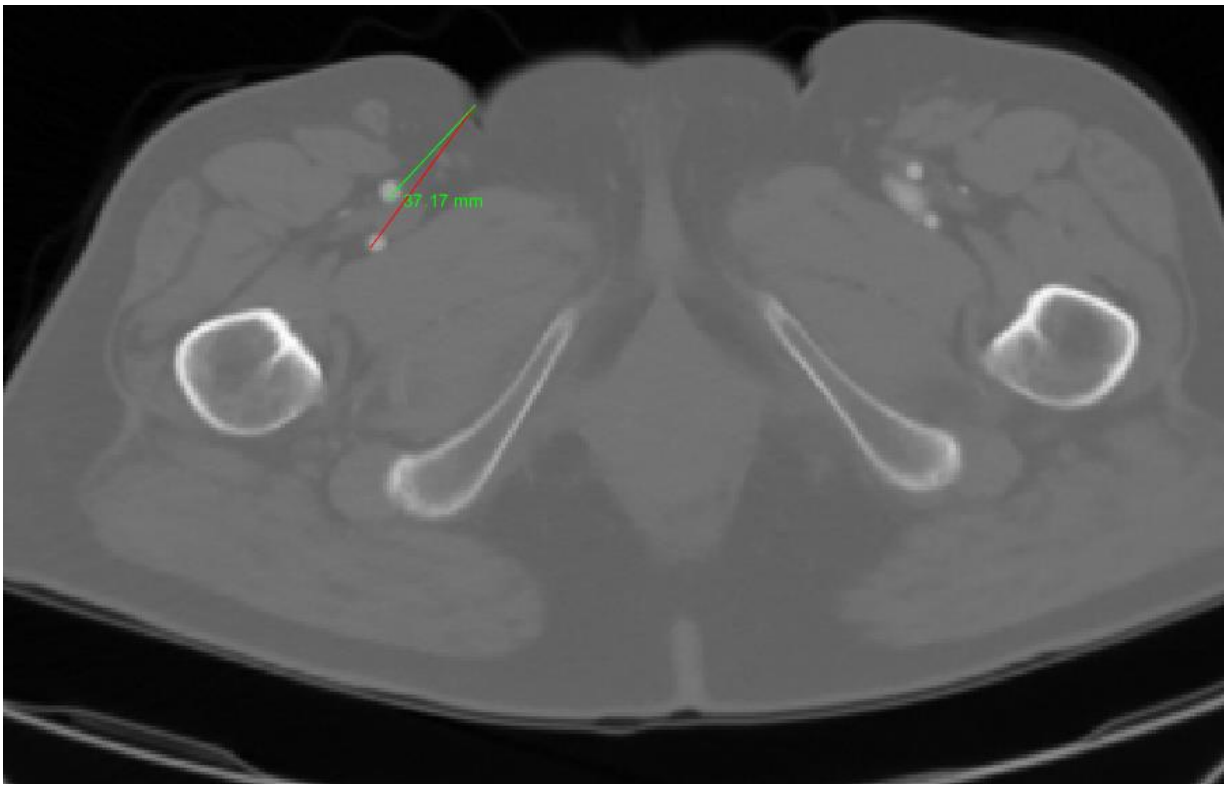

A

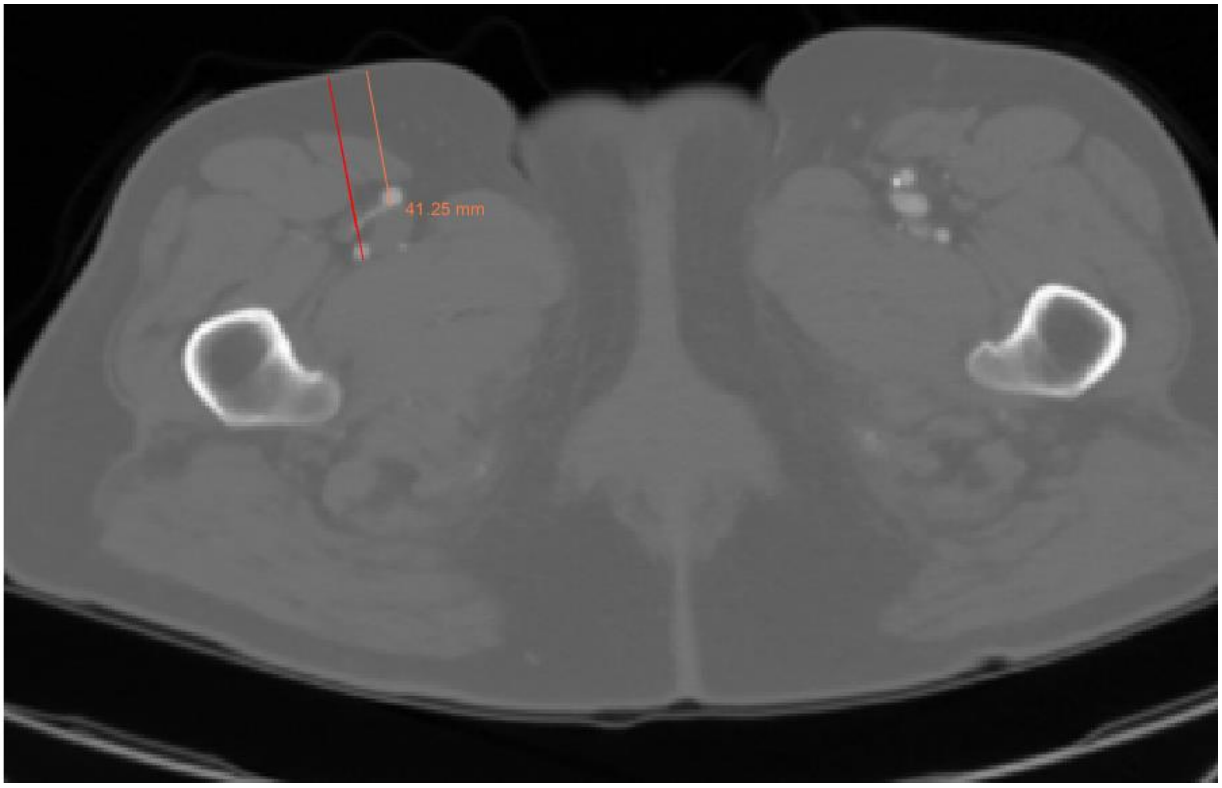

B

Figure 11: Overview of performed depth measurements at two locations around denoted SFA origin. Depth measurement colors correspond to depth intervals described in Table 4.

2.5.3 Validating the developed depth measurement algorithm

Phantom study and 35 CTA studies were used to verify whether the developed depth measurement technology meets the set requirements (section 2.5.1). In this section the phantom used, the applied validation method and the results are discussed.

2.5.3.1 Method

To make sure that the algorithm actually performs a correct depth measurement, a phantom has been developed whose exact dimensions are known. This Phantom consists of a cuboid container with internal dimensions of 200x80x100mm. To simulate a blood vessel, a tube with a diameter of 12mm runs in the center of this tank. In addition, 5 lime rings have been created with Hydroxyapatite and placed around the vessel tube to simulate calcified plaques. An overview of the used phantom is shown in Figure 12.

Before the phantom was scanned, the container was filled with demi water to a measured height of 75mm. As a result, the distance between the bottom of the tube and the water surface was 31mm. To simulate blood with contrast agent, the tube was filled with a mixture of contrast agent (Ultravist®-300 mg/mL, Bayer B.V., Mijdrecht, Netherlands) and demi water with a ratio of 1:30. Phantom scan was performed using an IQon Spectral CT scanner (Philips Brilliance; Philips Medical Systems, Best, The Netherlands) and scanned according to the lower extremity CTA protocol of the UMC Utrecht. Slice thickness was 3mm and radiation exposure parameters were 120 kilovolt and 106 milliampere second. To assess measurement deviation, vessel depth was measured on each slice using the developed depth measurement technique (section 2.5.2) and compared to the actual depth of 31mm. Furthermore, it is checked whether the depth measurements have been performed in the correct direction.

Next, DICOM files of CTA studies used for manual depth measurement (section 2.4.1.1) have been loaded and processed with use of the developed depth measurement technique (section 2.5.2) to verify whether the developed technique meets the remaining requirements (section 2.5.1). For all automatically processed CTA studies, it was checked whether the anatomical structures of interest were correctly and completely segmented. Furthermore, the measurement time was calculated for each processed study and it was checked whether the technique executed all depth measurements within 15 minutes.

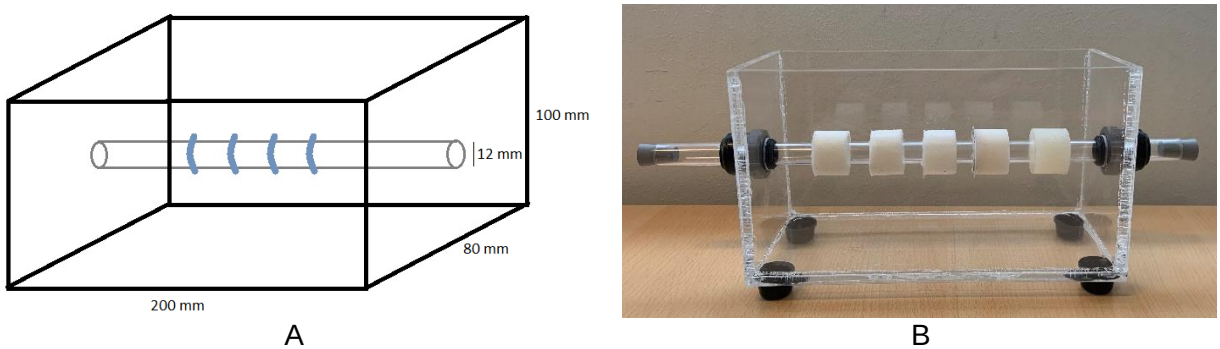

Figure 12: Schematic representation of the phantom with corresponding internal dimensions (A) and the created phantom used for automatic depth measurement validation (B).

Table 5: Mean, median, minimum and maximum for the measured depth (mm) and difference between real and measured depth (mm) (n=64).

	Mean	Median	Min	Max
Measured depth (mm)	30.57	30.50	28.25	32.00
Measurement Deviation (mm)	0.75	0.69	0.00	2.75

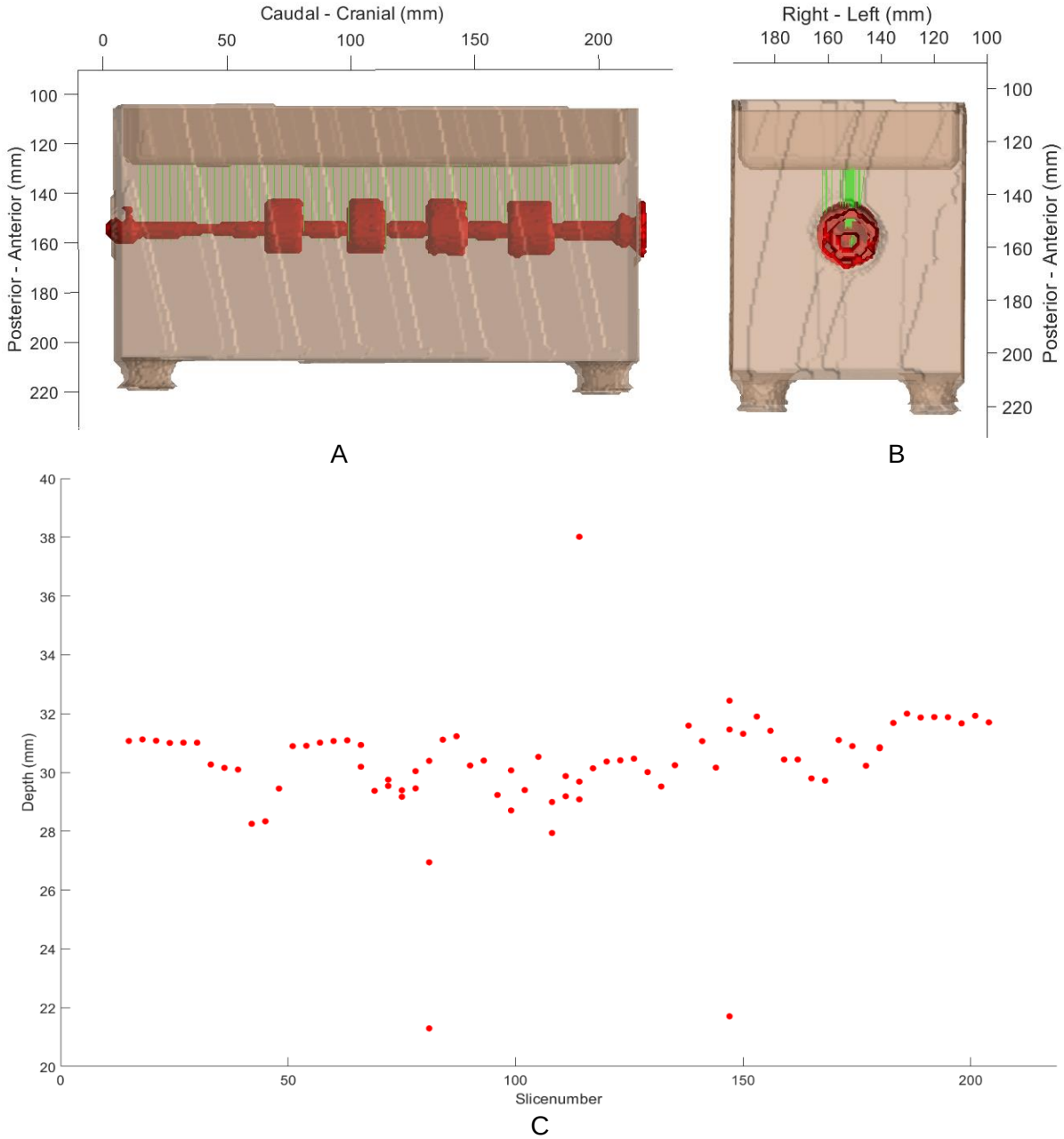

Figure 13: Sagittal (A) and transversal (B) view of 3D reconstructed phantom with depth measurements. Depth measurement direction is presented as green lines within the 3D reconstructed figures. Measured depth is showed in the graph (C), where the x-axis refers to the slice and the y-axis represents the measured depth (mm).

Table 6: Overview of successful segmentation results and automatic depth measurement time. Time is viewed with "HH:MM:SS" notation and values between brackets show minimum and maximum measurement time.

			Cases
	Number of cases		35
Segmentation	Aortic bifurcation – plantar arteries		12
	Aortic bifurcation – origin ATA/ATP		31
	Correct segmentation of anatomical structure	Arterial tree	15
		Bone	11
		Skin	33
Time	Below 15 minutes		20
	Below 30 minutes		27
	Median		00:13:32 (00:07:04 – 01:39:33)

2.5.3.2 Results

Sagittal and transversal overview of the 3D reconstructed segmentation of the phantom with 64 performed depth measurements show similar measurement directions for most measurements (Figure 13A and B). In addition, one of the five added calcified rings around the vessel is not segmented and reconstructed. Data points in the created depth measurement graph show a fairly constant line (Figure 13C). Table 5 shows an overview of mean, median and measurement range of the measured depth, difference between real and measured depth and the difference expressed as a percentages. Mean measured depth is 30.57mm (28.25mm – 32.00mm). Maximum difference between real and measured depth is 2.75mm.

In 31 CTA studies, the arterial vascular tree is in any case segmented from the aortic bifurcation to the origin of the ATA and ATP, while only in 12 studies the segmentation is extended to the plantar arteries. Furthermore, in 33 cases the skin is completely and correctly segmented, whereas for the segmentation of the arteries and bones this was only the case in less than half of the cases. The median duration that the algorithm needed to calculate the depth was 13:32 minutes. Minimum duration was 7:04 minutes and maximum duration was 01:39:33 hours. In 27 cases, the algorithm took less than 30 minutes to perform all depth measurements, whereas in 20 cases depth measurements took even less than 15 minutes. An overview of number all correct segmented anatomical structures and depth measurement duration can be found in Table 6.

2.6 Automatic performed depth measurements.

2.6.1 Method

To assess measurement agreement of manual and automatic performed measurements, shortest manually measured depths (measurement E, section 2.4.1.2) performed at the SFA by observer 1 were compared with automatic measured depths in 35 CTA cases (section 2.4.1.1). Measurements performed by this observer have been selected because the vascular surgeon is considered the most experienced observer. As a result, the measurements will best match current

Table 7: The ICC, reliability according to the predefined ICC classes (Table 1) and $CV_{\%mean}$ for interobserver agreement at the AFS (n=35). Values between brackets are the 95% confidence intervals of calculated ICC.

	ICC	Reliability	$CV_{\%mean}$
SFA	0.978 (0.956 – 0.989)	Excellent	8.95%

practice. To ensure measurement comparability, automatic depth measurement slice was matched to the slice on which the manual depth measurement was performed. In addition, it is checked whether the depth measurements performed manually and automatically on this slice had a comparable measurement direction. If the measurements are not taken in the same measuring direction, they must be excluded from further analysis.

2.6.1.1 Statistical analysis

First, the measurement agreement of manually and automatically performed depth measurements was assessed by calculating the Intraclass Correlation Coefficient (ICC) to indicate measurement reliability. Second, measurement agreement was visualized using Bland-Altman plot and CV was determined. Statistical analysis is performed with the same equations and reliability classes as used for manual depth measurement (section 2.4.1.3).

2.6.2 Results

Measurement agreement of manually and automatically performed depth measurements at the AFS was assessed with use of the ICC. Table 7 presents an overview of interobserver agreement and measurement variability. Measurement reliability was indicated as Excellent and $CV_{\%mean}$ was 8.95%. Furthermore, measurement agreement was assessed using Bland-Altman plot (Figure 5). Data shows no systematic bias and exceeded the limits of agreement only once.

2.7 Discussion

The aim of this study was to develop a technique that can automatically measure the distance between lower-extremity arteries and the skin in patients with peripheral artery disease. First, the reliability and agreement of manual performed depth measurement was determined. Assessed interobserver agreement showed excellent reliability and low $CV_{\%mean}$ for all measurements in the SFA and PTA. Second, automatic depth measurement method was developed in MATLAB and

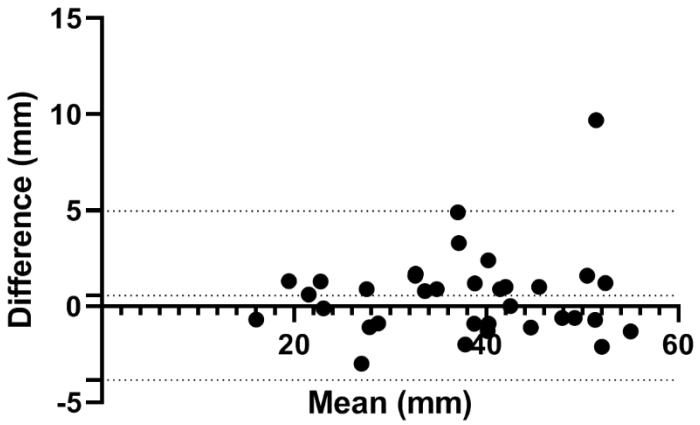

Figure 14: Bland-Altman plot of depth measurements in the SFA. In all plots the horizontal dotted lines represent from top to bottom the upper limit of agreement, the bias and the lower limit of agreement.

validated according to set requirements described in section 2.5.1. The maximum measurement deviation of the developed automatic depth measurement technique was to be lower than the set measurement deviation of 3mm. Furthermore, only in 11 of the used CTA studies segmentation of anatomical structures met all set requirements. Because in most cases this results in additional erroneous measurements in addition to well-measured depths between the skin and the contralateral vessel wall, the segmentation is considered acceptable. In addition, the set time limit of 15 minutes is achieved in 20 cases. However, in all cases this is caused by a multitude of depth measurements caused by incorrect segmentation of different anatomical structures. Therefore, improvement of the anatomical structure segmentation will lead to a reduction in measurement time. Finally, automatic depth measurement reliability and agreement was determined for measurements performed within the SFA. Assessed measurement agreement showed excellent reliability and low $CV_{\%mean}$. Although only one of the three requirements has been met, the developed technology shows a good match between manually and automatically measured depths. Moreover, the overall measurement deviation found is lower than 3mm and improvement of the anatomical structure segmentation will lead to a reduction in measurement time. Therefore, the development of the automatic depth measurement technique is considered successful.

2.7.1 Manual depth measurements

According to the reliability classes as defined by Koo and Li[33], interobserver agreement reliability scored Excellent for all depth measurements in SFA and ATA (Table 2). In addition, measurements performed in the EIA showed also excellent reliability for most measurements, whereas measurement reliability in the ATA was only moderate or good. Created Bland-Altman plots show no systematic bias (Figure 5 and Appendix B). Therefore, manual depth measurements within the EIA, SFA and PTA look reproducible. However, ICC only determines the ratio of interobserver differences. Consequently, reliability and agreement will still be high when both observers include similar depth measurement errors. To ensure measurement accuracy is also high, $CV_{\%mean}$ is used to provide information about the variability in terms of depth unit of measurement.[37] This means that the actual depth lies with a probability of 95% within the range of $CV_{\%mean}$ of the performed measurement. As a result, it means that the lower the $CV_{\%mean}$, the higher the accuracy of the performed measurements. When looking at all calculated $CV_{\%mean}$ percentages in Table 2, lowest $CV_{\%mean}$ values are found within the SFA and PTA. Furthermore, in accordance with the lower ICC values, a higher CV is found in the PTA. The excellent reliability and low $CV_{\%mean}$ found within the SFA and PTA, ensure that the depth measurements at those locations can be considered reproducible. In addition, measurements performed at the EIA showed slightly less good outcomes, but is still considered reproducible. The measurements in the ATA, on the other hand, only show moderate or good reliability with higher $CV_{\%mean}$ values. As a result, these measurements are considered less reproducible and therefore will not be included during further analysis.

For each anatomical landmark, five measurements were performed by each observer, of which only the measuring direction of measurement E is determined by the observer. Since for the other four measurements the measurement direction fixed, ICC was expected to show higher outcomes for these measurements. However, it appears that this expectation is incorrect for the measurements performed in the EIA and PTA (Table 2). Despite the guidelines set for performing the measurements, analysis of the selected slices showed a difference between selected slices on which the anatomical landmark is depicted by the observers. However, in most cases the difference in selected slice is only small. As a result, it does not seem logical that this has a major impact on the measured distance and therefore on the ICC. Nevertheless, in some cases this

small difference between selected slices has major consequences for the measured depth. This is mainly the case when a part of the artery has a larger horizontal than vertical deviation. Figure 15 shows an example of difference in measured distances, while maximum slice difference was only three slices. In this way, a difference in the chosen measurement location can induce larger differences in measured depths which will result in decrease in calculated ICC. A possible way to eliminate this difference in the selected slice is to improve the set definition of the anatomical landmark in the measurement protocol. Nonetheless it is likely that there will remain differences between the selected slices as observers still select the slices according to their interpretation of the set guidelines. It is therefore even better to determine in advance which slices should be used to perform depth measurements. As a result, the variation in selected measurement slice will disappear and therefore measurement comparability will increase.

The differences in selected measurement slices should not only be taken into account during ICC analysis. Additional uncertainty arises from the measuring direction determined by the user in measurement E, because outcomes is observer dependent. As a result, there is a possibility that the depth measurement was performed in different directions at the same anatomical location. Although it is possible that the measurements taken in different directions have approximately the same depth, these measurements are actually not comparable. Since the ICC also does not take

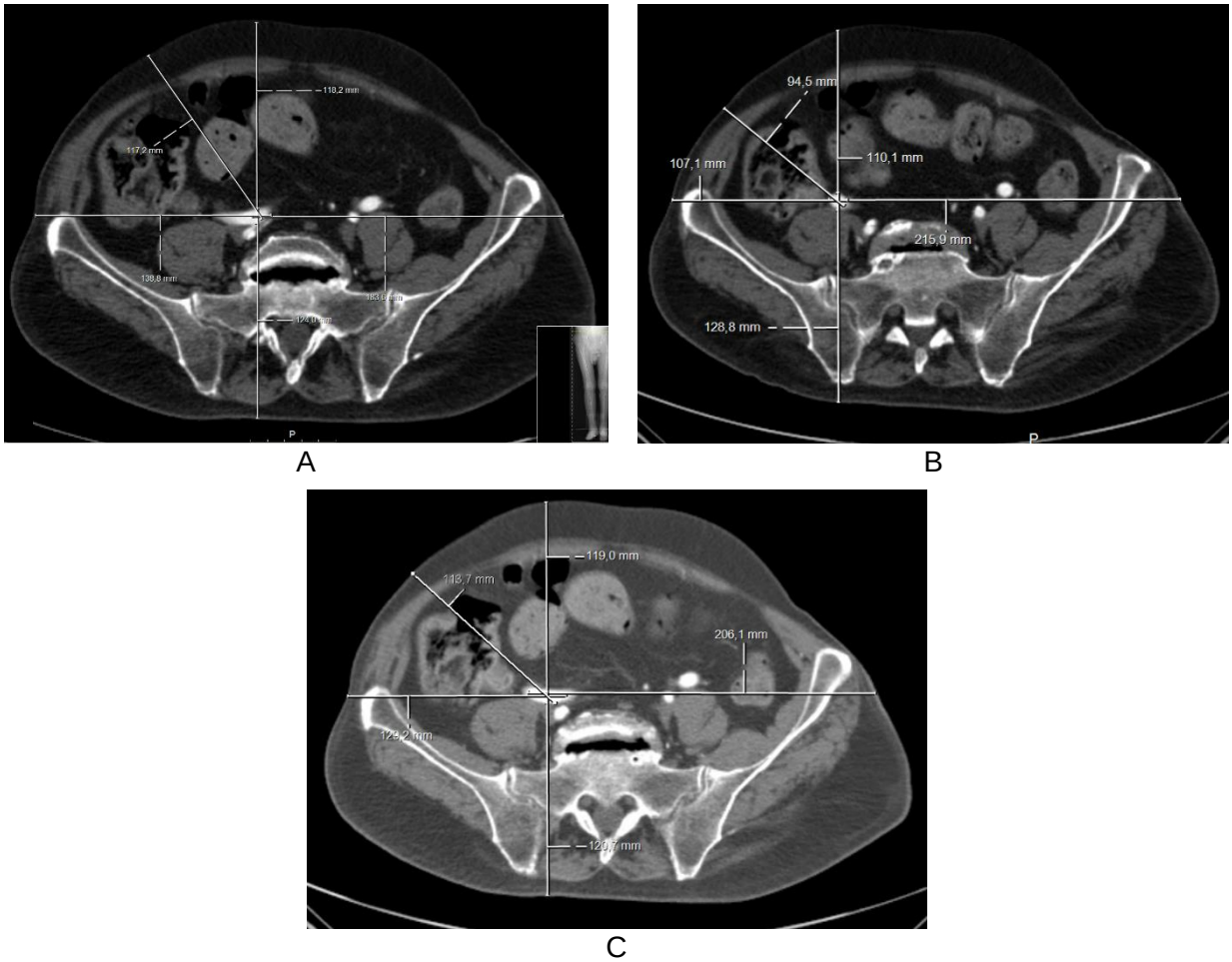

Figure 15: Overview of difference in measured depth measured at the EIA by observer 1 (A), observer (B) and observer 3 (C) within the EIA. Selected slice differed only 3 slices, whereas measurement location differed much more.

this difference in measurement direction into account, its outcome is only influenced by the measured depths. This raises the question whether the ICC values found for measurement are reliable, since different measurements with comparatively measured depths ensure a higher ICC, while this agreement is actually lower. A limitation of this study is therefore that only the measured depth is taken into account for assessment of measurement agreement.

Another important finding was that the calculated $CV_{\%mean}$ showed lowest variation for almost all measurement locations when comparing depth measurements performed by observer 2 and 3. This result suggests that depth measurements of these observers show more agreement compared to measurements performed by observer 1. Although observer 2 and 3 were less experienced observers, the reason why they have performed better corresponding depth measurements is difficult to determine. It is likely that these observers have maintained a less strict definition of the origin of anatomical landmarks or that, for example, they did not include the contralateral vessel wall during the measurements. On the other hand, this $CV_{\%mean}$ result for observer 2 and 3 does not indicate whether their depth measurements were performed more accurately compared to those performed by observer 1. To the best of our knowledge, no scientific papers have been published yet describing the influence of rater experience on agreement and accuracy in arterial depth measurements. However, there are publications that describe the influence of the experience of observers for other measurements. For example, Lee et al.[47] and Analan et al.[48] described the influence of observer experience on the assessment of respectively burn scars and hip migration. According to both studies, there is no evidence that experience improves measurement agreement or accuracy.[47,48] Although the measurements of observer 1 are less similar than those of observer 2 and 3 and there is no evidence indicating that the measurements of observer 1 were performed more accurately, only the measurements of observer 1 are used for subsequent analysis. Consequently, depth measurements performed by the surgeon are assumed to be closest to the clinical standards and are therefore considered the most representative in a comparison with the measurements made with the developed depth measurement technique.

2.7.2 Validation of developed depth measurement technique

Depth measurement outcomes presented in Table 5 show that maximum measurement deviation is 2.75mm. In addition, 3D overview of segmented phantom with performed depth measurements in Figure 13A and B show that most measurements are performed approximately in each slice at the same position and Figure 13C shows that most measured depths around 30 to 31mm. The result of the analysis of the segmentation of the various anatomical structures in Table 6 shows that the skin is well segmented in 33 cases. On the other hand, both arteries and bones are precisely segmented in less than half of the cases. In 15 cases, depth measurement time exceeded 15 minute limit. In 2 of these cases, the set 15-minute limit was exceeded by less than a minute. In both cases it concerned a large sized person, resulting in more skin edge data points and therefore more depth measurement possibilities to analyze. In the remaining 13 cases that exceeded the 15-minute time limit, bone regions were included in the arterial segmentation. In 7 cases this even resulted in a measurement time higher than 30 minutes. Of the 15 cases that met the 15-minute time limit, only 8 consisted of correctly segmented anatomical structures. In the other 7 cases, measurement time was mainly below 15 minutes because of inclusion of small bone regions or small sized persons. At the moment, the developed technology therefore only meets the 3mm measurement deviation.

The results of the phantom study showed that maximum measurement deviation smaller than set 3mm deviation. However, depth measurement chart in Figure 13C shows three measurements that deviate more than 3mm from the actual distance of 31mm. These measurements indicate the distance between the water surface and a segmented part of a lime ring. Therefore, these additional measurements were excluded from the deviation analysis. Moreover, the created measurement graph shows the pattern of the segmentation, since the measured depth of the vessel is lower at the level of the lime rings. This corresponds to the 3D overview of the phantom segmentation, since a decrease in diameter of the vessel is also seen at the position of the lime rings. The deviation at these positions are likely to be related to physics-based artifacts, such as beam hardening.[49] Another point of interest is that the actual distance between vessel and water surface did not remain constant. CT table movement during the scan caused a small wave in the water. Due to this water displacement, the possibility exists that the actual distance deviates from the originally measured 31 mm. This is a limitation of the research design used, since water displacement was not measured during scanning. Although the validation result may be slightly affected by this, the deviation caused by the wave is expected to be small. Therefore, this displacement was not taken into account during depth measurement deviation analysis.

Contrary to expectations, the developed depth measurement technique has not met set requirements for anatomical structure segmentation and measurement time. Analysis of the results of the developed depth measurement technique showed a relationship between the quality of the segmentation and the measurement time. Bone segmentation was considered successful only in 11 cases and therefore unsuccessful in 24 cases. Analysis of the segmentations showed that in 20 of these cases, arterial segmentation included bone regions, while bone segmentation was incomplete. This double segmentation error is caused by a combination of the CTA images and the applied segmentation techniques and steps. Usually in CT-images there is a large difference in intensity of blood and bone structures. However, in CTA images, the Hounsfield intensity of blood is increased by the use of contrast agents, and therefore the difference in intensity of blood and bones is much smaller. To prevent the threshold-based bone segmentation from including parts of the arterial vascular tree, the developed technique uses the arterial vascular tree that was previously segmented using the enhanced Frangi filter to mask the arteries. The limitation of this applied step is that the improved Frangi filter searches for clear tubular structures in the images. Because bones on CT images are represented as clear structures, there is the possibility that the improved Frangi filter detects a part of bone regions and therefore incorporates those bone regions in the arterial segmentation. This not only masks the arteries, but also the bone parts that are included in the vascular segmentation. As a result, the bone regions are segmented incompletely and are therefore considered incorrect. Moreover, the technology developed identifies the included bone parts as artery, resulting in additional performed depth measurements per slice. As a result of these additional incorrect measurements, the measurement time is also extended. Figure 16 shows an example of the above-described erroneous inclusion of bone regions in the arterial segmentation and resulting increase in depth measurements performed.

Although arterial and bone segmentation outcomes were not very encouraging, it seems that preventing the erroneous inclusion of bone segments in the arterial segmentation will lead to an increase of correctly segmented structures and a decrease in the measurement time. One possible way to improve this segmentation is by using magnetic resonance angiography (MRA) instead of CTA. MRA has the advantage that it only shows the blood vessels with a high intensity and therefore the enhanced Frangi filter used will only select the arteries. The disadvantage of

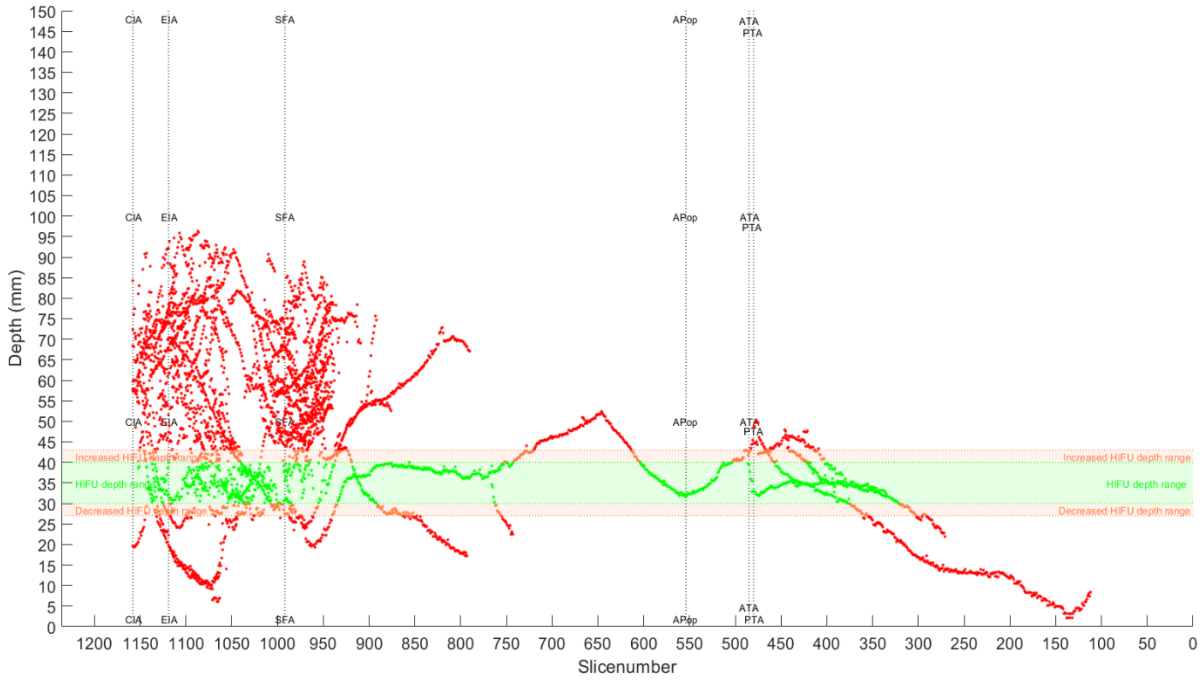

A

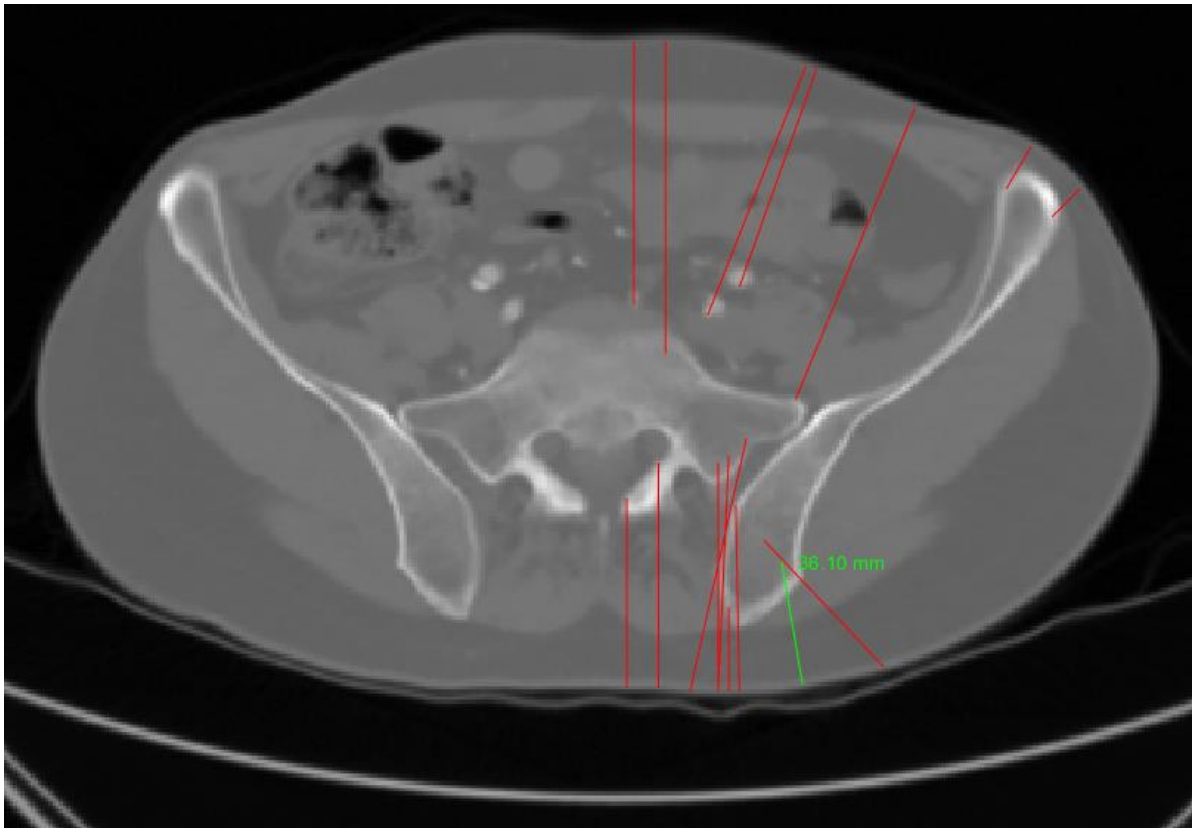

B

Figure 16: Example of depth measurement graph in which bone structures are incorporated in the arterial segmentation and therefore depth measurements are also performed between skin and bones (A). In addition, example of slice on which multiple erroneous depth measurements are performed between bone and skin. Colors correspond to measured depth described in Table 4.

MRA, however, is it's lower spatial resolution and longer scan time compared to CTA. In addition, an MRA of the lower extremities is scanned in phases, which means that an MRA data set consists of different parts. Although the MRA segments can be merged based on the DICOM info, additional steps are needed to align the data. Although MRA segments can be merged based on the DICOM info, additional steps are needed to align the data. Moreover, it is possible that MRA segments are difficult to align due to patient movement between acquisition of the different segments. The use of MRA instead of CTA is therefore not considered a better alternative. Another more suitable solution is to use CTA scans acquired with an IQON spectral CT scanner which has the ability to reconstruct a virtual non-contrast scan beside the original CTA scan with contrast.[50] The major advantage of using this technique is that the reconstructed non-contrast scan can be accurately aligned with the original scan and therefore the non-contrast scan can be used to mask bone regions within the original contrast scan. As a result, the used improved Frangi filter is prevented from including parts of bone regions in the arterial segmentation and therefore the number of correct segmented cases is expected to increase. In addition, improving arterial segmentation will reduce the number of erroneous arterial measurement points. It is therefore expected that the number of cases in which depth measurements are taken within 15 minutes will also increase.

In addition to the 20 cases in which both arterial and bone segmentation were incorrect, there are 4 cases in which only bone segmentation was incomplete. In all 4 incorrect bone segmentations, part of the sacrum was incompletely segmented and therefore a number of depth measurements are performed through this bone (Figure 17). This is most likely due to the fact that the sacrum, unlike for example the tibial bone, does not have a thick cortical bone edge. Therefore, segmentation of this specific bone is more difficult when using a segmentation technique based on a predetermined threshold level. To improve bone segmentation, it has been investigated whether an active contour based segmentation technique showed better segmentation results. Active contours can be defined as the process to obtain deformable models or structures with constraints and forces in an image for segmentation.[51] Although the MATLAB version used has a built-in function based on this active contour segmentation and showed better outcomes, the technique proved to be very time-consuming and therefore not a useful alternative. Another possible solution is to create the segmentation of the anatomical structures with a different segmentation program and then be aligned and merged in MATLAB. This means more additional steps must be performed before the developed technology actually measures artery depth. Moreover, these segmentation programs often require user input and created segmentations still need to be checked and often improved where necessary. As a result, this option becomes more time consuming and is therefore considered undesirable. Besides, the question is whether the incomplete segmentation influences treatment selection, since these measurements were performed at a location that is not eligible for transcutaneous treatment such as HIFU. Furthermore, the developed technique enables the user to verify whether the measurement has been properly performed and whether the measured distance is actually correct. Until the developed depth measurement technique can be linked to the transcutaneous treatment modality and without user intervention being determined at which location the treatment should be performed, these measurement errors will not have large-scale consequences.

At last, Table 6 showed that in 2 of the 35 cases the skin is not correctly segmented. Both times it concerned a case in which the intestines were filled with air. What is curious about this result is that the developed technique should fill any cavities present within the skin segmentation. However, it appears that when the cavity runs from the first slice, the cavities persist and the edges

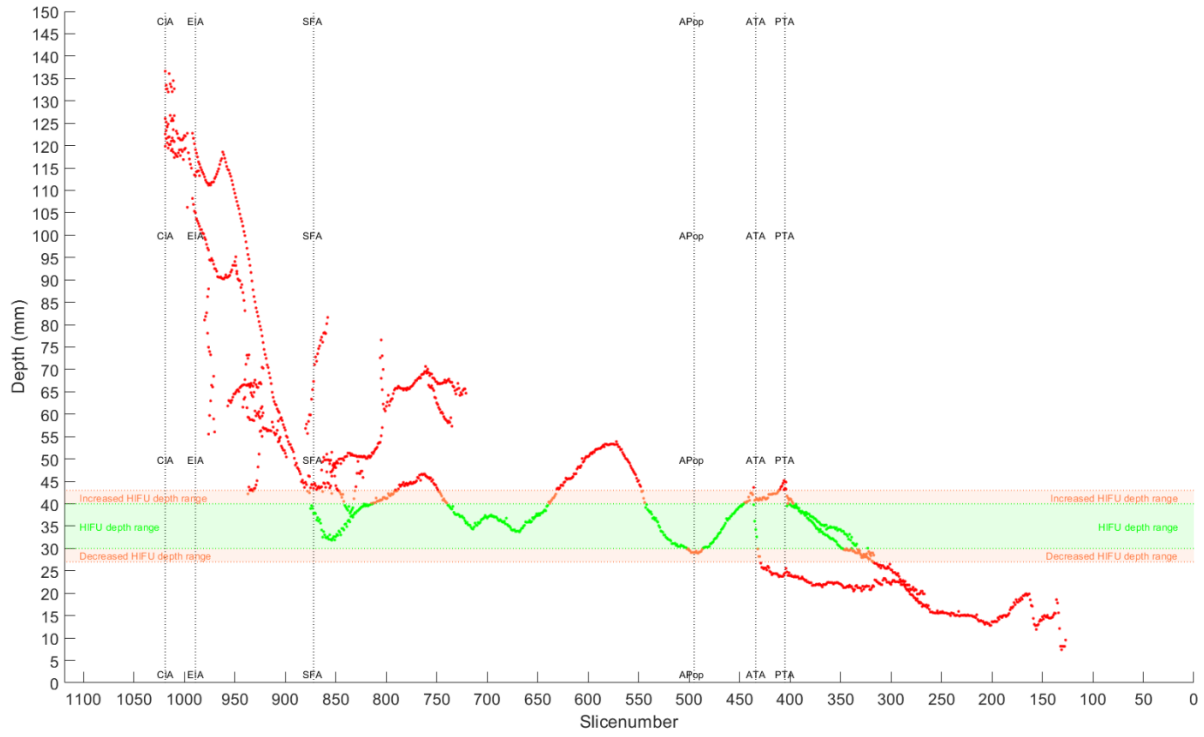

A

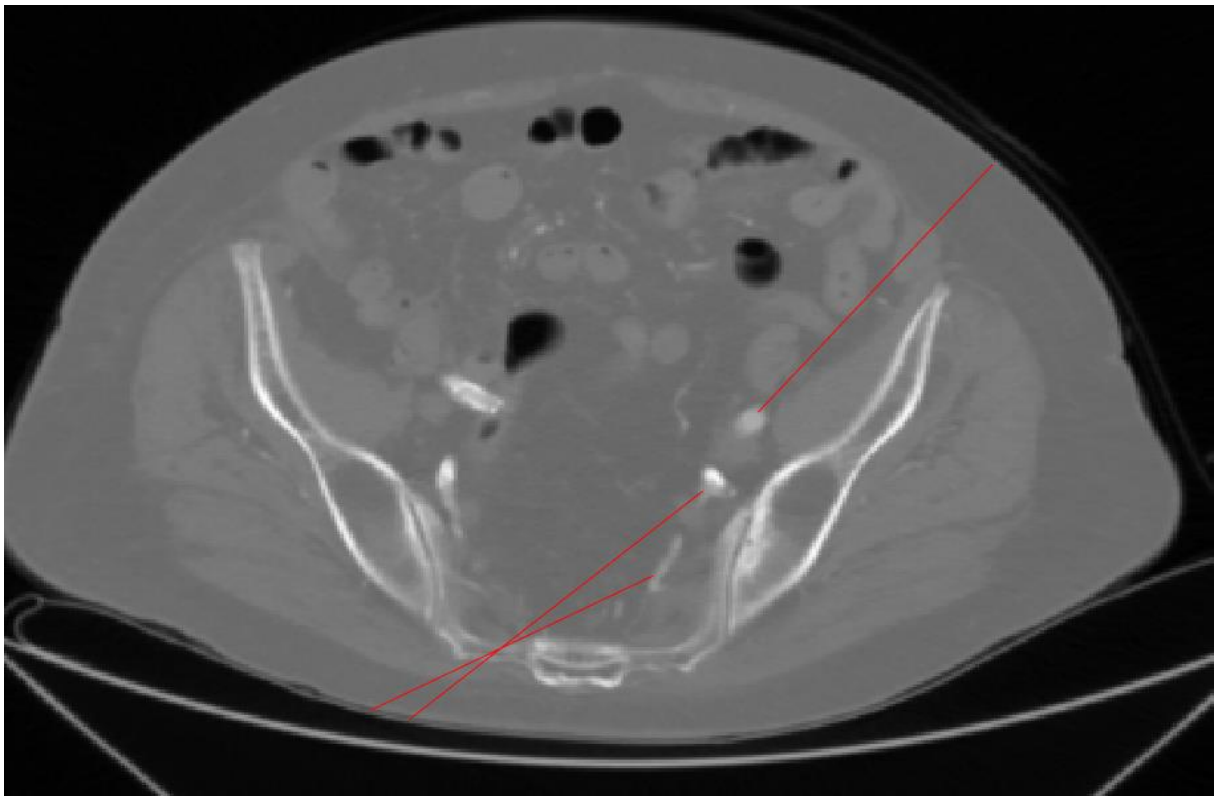

B

Figure 17: Example of depth measurement graph in which part of the sacrum was segmented incompletely and therefore depth measurement was performed through this bone region. (A). In addition, example of slice on which erroneous depth measurements were performed is showed (B).

of these cavities are therefore included as a skin edge. Consequently, the developed technology measures the shortest distance between these cavity edges and the arterial wall, resulting in incorrect depth measurements. Removement of these remaining cavities will improve skin segmentation and therefore will also result in correct performed depth measurements. In all cases, however, this deviation only applies to the lower abdomen and not to the segmented lower extremities. Depth measurements in the lower extremities will therefore not be affected by this incorrect skin segmentation. For this reason, this incorrect segmentation is considered acceptable.

Although the developed depth measurement technology meets only one of the three requirements, its operation is considered adequate. The main reason for this outcome is the fact that maximum measurement deviation found was less than 3 mm and that in all cases the technique is able to calculate the distance between skin and contralateral vessel walls. Moreover, the described segmentation errors and subsequent erroneous depth measurements only occur in the pelvic area or feet. As a result, the developed technology performed the depth measurements correctly in most parts of the lower extremities. By improving in particular the segmentation of the arteries and the bones, the measurement results of the technique will improve and the duration will decrease.

2.7.3 Agreement of manual and automatic performed depth measurement at the SFA

ICC showed excellent measurement reliability and $CV_{\%mean}$ below 10%. In addition Bland-Altman plot was used to visualize measurement agreement, showing no systematic bias and limits of agreement were only exceeded once. The developed technology showed measured depths that correspond well with the manually measured depths in the SFA. Therefore, the developed technology is considered to be able to automatically measure the arterial depth in the SFA.

As described in section 2.7.1, manual performed measurements performed in the EIA, SFA and PTA showed good measurement agreement. Therefore these measurements were used to compare manual performed measurements and measurements performed by the developed technique. To ensure measurements comparability, it was checked whether the manual and automatic depth measurements were performed in the same direction. Assessment of measurement directions at the defined anatomical landmarks showed that only at the SFA measurement were performed in similar directions. The deviating measurement directions in the EIA and PTA are mainly caused by a limitation of the measurement protocol used. The protocol instructs the observer to measure the shortest possible distance between skin and contralateral artery wall without specifying that these measurements should not pass through a bone area. As a result, the shortest manual measured distance in many cases has a different measuring direction compared to the measurement direction of the developed technology since it excludes measurements when passing through a bone region. Consequently, it was decided to compare the measured depth only at this anatomical landmark.

Another point of attention is that for the comparison of measurement results, the same cases and technique were used as in the validation of the technique. As a result, several automatic depth measurements were performed at the SFA in some cases. If this was the case, the correct depth measurements between skin and contralateral artery wall was selected from all measurements. It is therefore possible that when two of these measurements were close to each other, the wrong measurement was selected and this slightly influenced the outcome. It is therefore questionable whether these outcomes may be regarded as representative and actually demonstrate the true agreement. To find out, the technique must first be improved before this analysis is carried out again. If similarities are found, it can be assumed that the test results of the developed technology were initially also representative.

Finally, it is unlikely that depths measured by the developed depth measurement technique will fully correspond to manual measured depths. In addition to the fact that the manual measurements are observer-dependent and will therefore cause measurement deviations, the technology developed has two limitations that can lead to deviations from automatically measured depths. First, the technology only segments the contrast-enhanced arterial lumen. This means that the measurements are performed up to the edge of the lumen instead of up to the artery wall. Second, the developed technology measures the distance between the centers of pixels. Therefore, when the skin and / or vascular wall is located on a pixel edge, the technique possibly over or underestimated the measured depth. Although the expectation is that both limitations will only have a small influence on the measured depth, this study did not address this possible influence. Moreover, as far as we know, there are no publications describing the influence of these limitations in a similar measurement technology. In addition to improvement of the developed technology, future studies on the current topic are therefore recommended.

2.8 Conclusion

This study showed that manual depth measurements performed in EIA, SFA and PTA are considered reproducible. Subsequently, an automatic depth measurement technique was developed to measure the distance between the skin and the contralateral arterial wall in the lower-extremity. Three requirements were set in advance for the technology developed; maximum measurement deviation of 3mm, individual segmentation of anatomical structures and time limit of 15 minutes. Phantom measurements showed that the maximum measurement deviation of the developed technique was 2.75mm. On the other hand, set requirements for anatomical structure segmentation and time limit were exceeded. However, data analysis showed that improving the segmentation of the anatomical structure is likely to reduce measurement time and increase the number of cases in which the anatomical structures are segmented separately. Since in all cases only additional erroneous measurements have been performed and the measurement deviation found is lower than 3 mm, the result of the developed technology is considered acceptable. Finally, comparison of manually and automatically measured depths in the SFA showed excellent reliability and agreement. It is therefore possible in any case to measure the arterial depth of the lower extremities at the level of the SFA using the developed automatic depth measurement technique.

Chapter 3: The correlation of tortuosity, curvature and torsion in the extracranial carotid artery

3.1 Clinical background

Dolichoarteriopathies are arterial abnormality phenotypes that primarily affect the extracranial carotid artery (CA) and are often visualized with angiography and ultrasound studies.[52–55] Metz et al.[56] and Weibel et al.[57] have established a classification system for dolichoarteriopathies in the internal carotid artery (DICA) that consists of three types: tortuous, coiling and kinking (Figure 18). In addition, in some cases the tortuous type includes also the described coiling or kinking type. Several studies state that the prevalence rates of DICA are around 25%.[54,58] The degree of tortuosity within this percentage, however, still varies widely. Even though DICA can therefore be regarded as a common anatomical abnormality, still little is known about the relationship between DICA and for example the development of CA disease or cerebral ischemia (*i.e.* transient ischemic attack or stroke). In the present study, CA disease is defined as stenotic lesions or aneurysms -of the common carotid artery (CCA) or internal carotid artery (ICA).

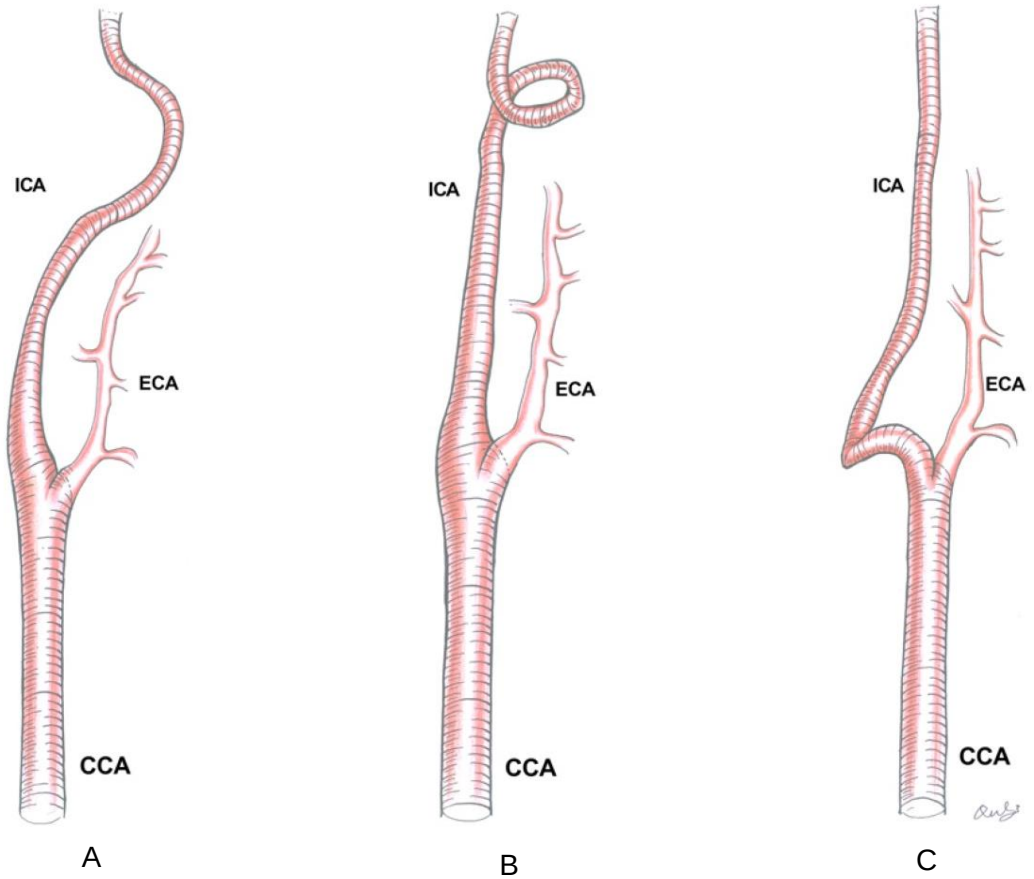

Figure 18: Different types of Dolichoarteriopathies: A: tortuous, B: coiling and C: kinking. CCA: common carotid artery, ECA: external carotid artery and ICA: internal carotid artery.[54]

Theoretically, DICA's may be associated with atherosclerotic risk factors, such as diabetes mellitus, hypercholesterolemia, hypertension and smoking.[54,59,60] However, some studies have found that the presence of cardiovascular atherosclerotic risk factors are comparable in patients with and without DICA.[61,62] Age and CA dissection are considered acquired risk factors which can cause DICA and also congenital factors can contribute DICA development.[58,63,64] Although there are strong suspicions that the risk factors described above are strongly related to the development of DICA, there is still much uncertainty about the exact cause and possible consequences of DICA.

As the anatomical variety in DICA is large, the present study addresses the clinical implication of CA geometry expressed in tortuosity index (TI), curvature and torsion. TI is defined as a ratio between central luminal line length and straight distance. In addition, curvature is defined as the amount in which the CA deviates from a straight line, while torsion is defined as the degree in which the artery twists out of the curvature plane. Recent studies have shown that curvature is a reliable predictor for endoleaks and stent migration after aortic aneurysm repairs.[65–67] Curvature and torsion in CAs has been described to the best of our knowledge only once.[68] At this point, the relation of the more established TI with curvature and torsion is therefore unknown. The hypothesis is that in an artery with a low TI, the curvature can still be large, while the other way around is not possible. This is because TI can be relatively low while the artery still has a sharp kink. While tortuosity will give the physician a global understanding of the course of the artery, the curvature and torsion will additionally indicate whether there is only a sharp kink or whether it is more tortuous. Ultimately, this prior knowledge is likely to help the physician predict the chance of developing an aneurysm and to prepare carotid interventions.

3.2 Research aims

The main research question that will be answered in this chapter of the thesis is described below:

What is the correlation of tortuosity index curvature and torsion of the carotid artery?

To answer the main question, the following supporting research questions have been defined:

1. *What is the inter and intraobserver agreement for TI measurements in the carotid artery?*
2. *What are tortuosity indices of the carotid artery?*
3. *What are curvature and torsion values of the carotid artery?*
4. *Is there a correlation in tortuosity index, curvature and torsion within the carotid artery?*

3.3 Aim of the study

The aim of this study is to find out if and how tortuosity index, curvature and torsion are related in the CA. To achieve this objective, the following subgoals have been defined:

1. *Determine the inter- and intraobserver agreement for TI measurements in the carotid artery*
2. *Determine the tortuosity index values in the carotid artery.*
3. *Determine the curvature and torsion values in the carotid artery.*
4. *Determine if there is a correlation between tortuosity index, curvature and torsion in the carotid artery.*

3.4 Method

3.4.1 Patient selection and image technique

The dataset for tortuosity measurements exists of 140 subjects of which 35 had an extracranial carotid artery aneurysm (ECAA). Subjects underwent a CTA scan according to regular protocols. All CTA studies were performed using a 64- or 128-slice CT scanner (Philips Brilliance; Philips Medical Systems, Best, The Netherlands). The carotid arteries were visualized from aortic arch to skull base. Median slice thickness was 0.67mm (range 0.62-0.90mm), increment 0.33, collimation 64x0.625 and pitch 0.609. Radiation exposure parameters were 100-120 kilovolt and 150-300 milliampere second. The field of view was set per patient. Injection of 65 milliliter intravascular contrast (Lopromide, Schering, Berlin, Germany) was followed by a saline bolus of 40 milliliter, both at a flow rate of 6.0 milliliter per second.

3.4.2 Carotid tortuosity measurements

Carotid tortuosity measurements were performed using 3Mensio Vascular software (Version 9.1, Pie Medical Imaging, Maastricht, The Netherlands) since De Vries et al.[69] has demonstrated that this software is user-friendly and suitable for measuring tortuosity. First, CA was segmented and reconstructed after which the central luminal line (CLL) was calculated and drawn automatically using the software. For CLL calculation, four points were placed within the segmented CA in following order: (1) at skull base, (2) at carotid bifurcation, (3) at side of CCA origin and (4) at contralateral side of CCA origin. To ensure that all CLL points are located around the same position, the following two criteria for the locations were set; (1) the CLL start point at skull base was defined as the last slice on which the ICA is completely surrounded by bone and (2) CLL start point of the right CCA was located at its origin at the bifurcation of the right brachiocephalic artery and the CLL start point of the left CCA is located at its origin at the aortic arch. After all points were placed successfully at the correct positions, the software automatically draws the CLL. The course of the CLL was checked by the observer and corrected to the correct position where necessary. When the drawn CLL was satisfactory, the TI was calculated using the following equation:

$$TI = \frac{True\ length\ CLL}{Straight\ distance} \quad \textbf{(3)}$$

Where the true length CLL is represented by the length of the drawn CLL between two predefined landmarks and the straight distance is represented by the measured direct distance between the same two points.

TI was calculated three times; (1) from skull base to carotid bifurcation (ICA), (2) from carotid bifurcation to CCA origin (CCA) and (3) from skull base to CCA origin (CA). To ensure comparability and reproducibility of measurements, the following two criteria for the locations were set when looking in craniocaudal direction; (1) the location of the measurement point at skull base was defined as the last slice on which the ICA is completely surrounded by bone and (2) the location for the measurement point of both the carotid bifurcation and the origin of the CCA was defined as the most distal slice on which the arteries in question are visualized separately. An example of 3Mensio segmented CA along with performed TI measurements is shown in Figure 19.

3.4.3 Carotid artery curvature and torsion measurements

MATLAB (Version R2019b, MathWorks, Natick, Massachusetts, USA) was used for visualization of the CAs and exported 3Mensio semi-automatic drawn CLLs. To ensure comparability of

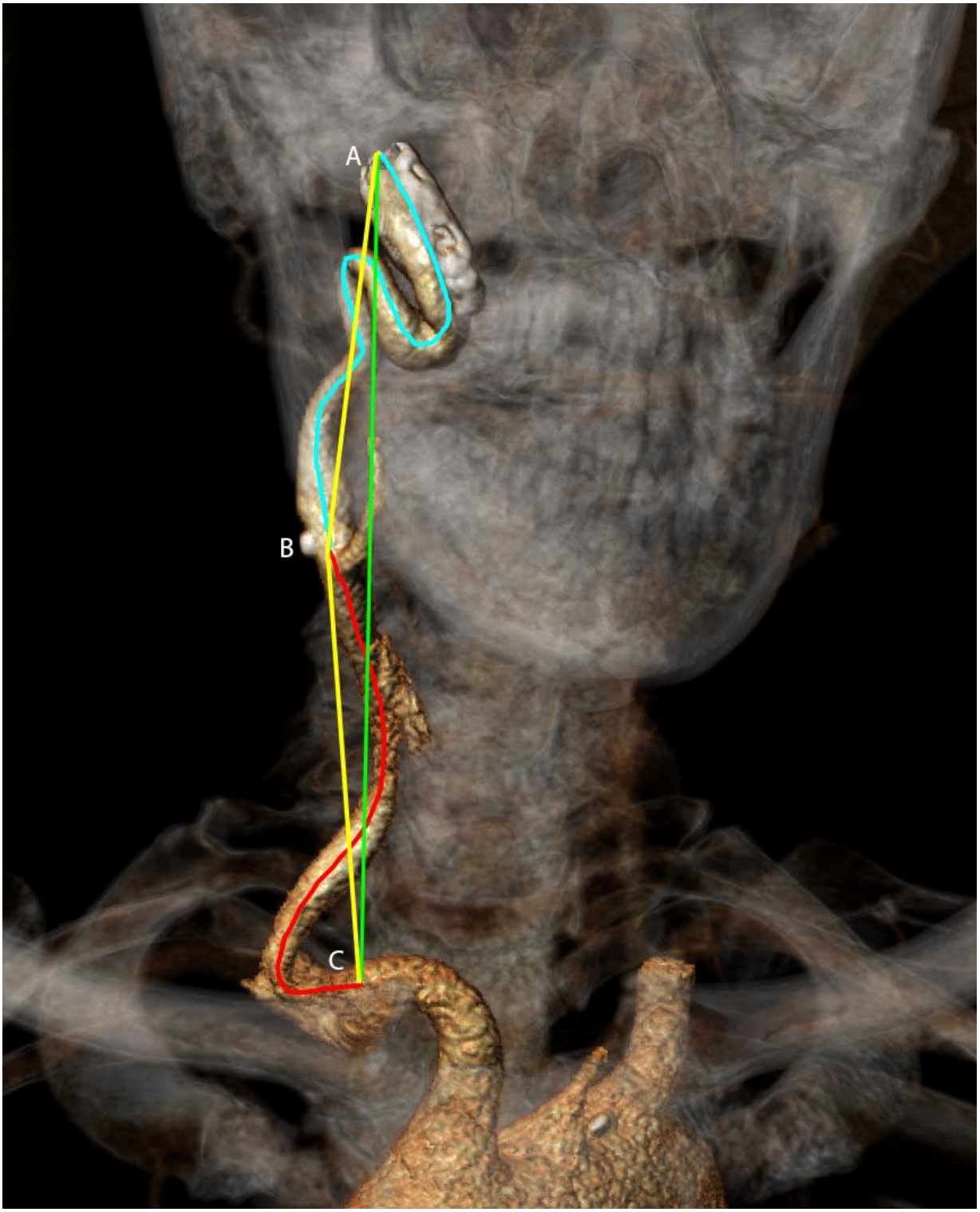

Figure 19: Example of a 3Mensio created segmentation of a subject with an extracranial carotid aneurysm of the right internal carotid artery (ICA). The carotid tortuosity index was calculated for every study patient as ratio of the length of the central luminal line (CLL) and the straight line length. The carotid artery was measured from skull base (A) until carotid bifurcation (B), and origin of the CCA (C). The CLL for the ICA is indicated in blue, for the common carotid artery (CCA) in red. The CLL of the total carotid artery was calculated by adding ICA and CCA CLL length. The straight distances are indicated in yellow and green.

Table 8: Curvature and torsion groups with corresponding cutoff values.

Group:	Curvature	Torsion
Low	curvature ≤ 0.15	torsion ≤ 5
Medium	0.15 < curvature ≤ 0.3	
High	0.15 < curvature > 0.3	torsion > 5

the results, the coordinates of the 1mm interpolated CLLs created with the steps described in section 3.4.2 were used. For CLL curvature calculation, the equation for calculation of the extrinsic linear curvature as described by Schuurmann et al.[65] was used (equation 4). To calculate CLL torsion, the equation derived from the theory described by Pressley[70] was used (equation 5). Both equations are described below:

$$\kappa = \frac{\sqrt{(z''y' - y''z')^2 + (x''z' - z''x')^2 + (y''x' - x''y')^2}}{(x'^2 + y'^2 + z'^2)^{\frac{3}{2}}} \quad \textbf{(4)}$$

$$\tau = \frac{x'''(y'z'' - y''z') + y'''(x''z' - x'z'') + z'''(x'y'' - x''y')}{(y'z'' - y''z')^2 + (x''z' - x'z'')^2 + (x'y'' - x''y')^2} \quad \textbf{(5)}$$

Where $[x, y, z]$ are the CLL cartesian coordinates, $'$ is the first derivative, $''$ is the second derivative and $'''$ is the third derivative. Calculated curvature will be arranged in three groups; low, medium, high curvature. Furthermore, calculated torsion will be arranged in two groups; low and high torsion. An overview of these created groups with corresponding cutoff values is shown in Table 8.

3.4.4 Statistical analysis

TI measurements were performed by two independent observers (researcher and graduation student at the department of vascular surgery). First, inter-observer agreement was assessed by calculating the Intraclass Correlation Coefficient (ICC) to denoted measurement reliability and reviewing Bland-Altman plots. Second, and Coefficient of Variation was calculated. For assessment of the intra-observer reliability and agreement, 20% of the cases were re-performed by both observers. For both inter- and intraobserver agreement similar statistical analysis steps were executed as described in section 2.4.1.3.

After determination of inter- and intraobserver agreement, multiple regression analyses were performed to find whether there is a correlation of TI, curvature and torsion. In order to assess the relation of mutual estimates, correlations between tortuosity, curvature, and torsion were analyzed.

3.4.4.1 Determine the correlation of TI, curvature and torsion.

First, to check correlation of TI, curvature and torsion univariate analysis was used to compare ipsi- and contralateral CA within ECAA group and to compare ECAA group with the control group. Second, Pearson correlation coefficient was calculated to test correlation between measured TI, curvature and torsion.[71] P-values below 0.05 are considered statistically significant. All statistical

Table 9: The ICC, reliability according to the predefined ICC classes (Table 1), lower limit of agreement (LLA), upper limit of agreement (ULA) and $CV_{\%mean}$ for interobserver agreement (n=174). Values between brackets are the 95% confidence intervals of the calculated ICC.

	ICC	Reliability	LLA	ULA	$CV_{\%mean}$
ICA	0.983 (0.977–0.988)	Excellent	-0.047	0.098	5.72%
CCA	0.921 (0.849–0.959)	Excellent	-0.049	0.092	6.35%
CA	0.980 (0.973–0.985)	Excellent	-0.033	0.068	4.27%

analyses are performed by use of SPSS statistical package version 25 (IBM SPSS for windows, Armonk, NY).

3.5 Results

3.5.1 Interobserver agreement

A total of 175 tortuosity measurements are performed by two observers in 140 unique subjects for interobserver assessment. Due to CA occlusion, one case was excluded from analysis. Table 9 presents an overview of the interobserver agreement with denoted reliability and calculated $CV_{\%mean}$. For all TI measurement segments, measurement reliability scored Excellent. In addition, only lower bound of 95% confidence interval of TI in the CA showed good reliability. Furthermore, lowest precision (1.95%) and highest $CV_{\%mean}$ (6.35%) were calculated for tortuosity measurements in the CCA. Figure 20 presents the created Bland-Altman plots of the segments used for tortuosity measurement. All plots show no systematic bias and limits of agreement are exceeded by less than 10% of the total dataset.

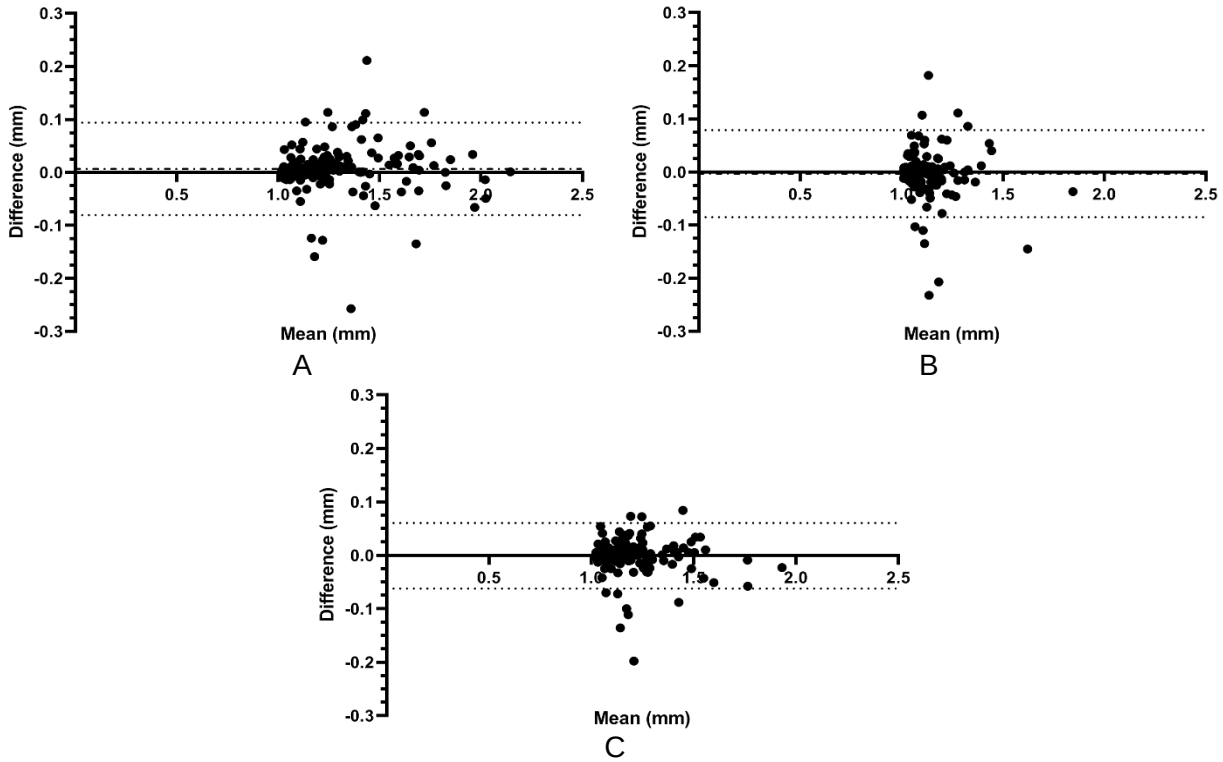

Figure 20: Bland-Altman plots of tortuosity index in ICA (A), CCA (B) CA (C). In all plots the horizontal dotted lines represent from top to bottom the upper limit of agreement, the bias and the lower limit of agreement.

Table 10: The ICC, reliability according to the predefined ICC classes (Table 1), lower limit of agreement (LLA), upper limit of agreement (ULA) and $CV_{\%mean}$ for intraobserver agreement (n=35). Values between brackets are the 95% confidence intervals of the calculated ICC.

	Observer	ICC	Reliability	LLA	ULA	$CV_{\%mean}$
ICA	1	0.980 (0.962-0.990)	Excellent	-0.055	0.108	6.31%
	2	0.998 (0.997-0.999)	Excellent	-0.011	0.031	1.61%
CCA	1	0.920 (0.847-0.959)	Excellent	-0.044	0.092	6.17%
	2	0.978 (0.956-0.989)	Excellent	-0.025	0.045	3.16%
CA	1	0.980 (0.962-0.990)	Excellent	-0.032	0.070	4.27%
	2	0.996 (0.993-0.998)	Excellent	-0.013	0.028	1.75%

3.5.2 Intraobserver agreement

For assessment of intraobserver agreement, 20% of the initial 175 tortuosity measurements are reperformed by the same two observers resulting in a dataset of 35 cases. Measurement reliability was excellent in all TI measurement segments for both observers. Only lower bound of 95% coincidence interval from measurements of observer 1 in CCA scores good reliability. Furthermore, $CV_{\%mean}$ was highest when comparing measurements of observer 1 (4.27%-6.31%), while $CV_{\%mean}$ for measurements of observer 2 were all lower (1.61%-3.16%). Figure 21 presents the created Bland-Altman of the segments used for tortuosity measurements. All plots show no systematic bias and limits of agreement are exceeded by less than 10% of the used dataset for intraobserver assessment. Because both the ICC scores and calculated $CV_{\%mean}$ show better outcomes for observer 2, only measurements of observer 2 will be used for further analysis.

3.5.3 The correlation of tortuosity, and curvature and torsion when comparing ipsi- and contralateral carotid artery in subjects with ECAA

Table 11 presents an overview of study population characteristics. The ECAA subject group existed of 35 cases and the control group of 105 cases. Median age was 62 years (25 – 82). In both groups, gender and side are equally distributed. For every subject within the ECAA group 3 matched control patients were included in the control group.

Wilcoxon signed rank test for matched subjects was used to compare TI, curvature an torsion of 33 affected ipsilateral and 30 non-affected contralateral carotid arteries. Due to uncertainties in the exported CLL, respectively 2 and 5 subjects were excluded from analysis. Within the ECAA patients group, no significant difference in measured TI, curvature and torsion in ipsi- and contralateral carotid arteries was found (Table 12).

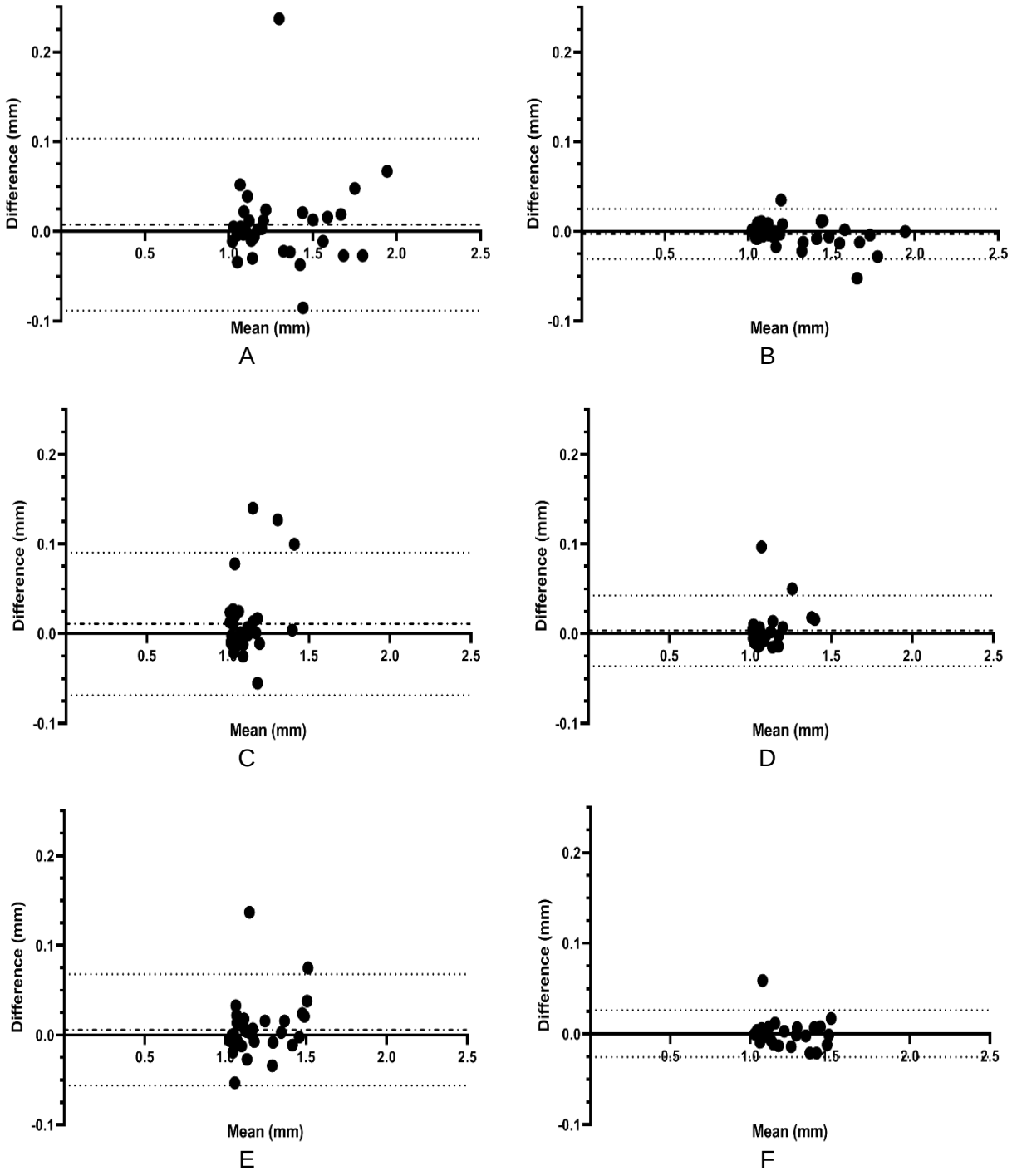

Figure 21: Bland-Altman plots of tortuosity measurements performed by observer 1 in ICA (A), CCA (C) and CA (E) and observer 2 in ICA (B), CCA (D) and CA (F). In all plots the horizontal dotted lines represent from top to bottom the upper limit of agreement, the bias and the lower limit of agreement.

Table 11: Baseline characteristics of study population.

		ECAA		Control	
		n	%	n	%
Cases		35	100	105	100
Male		18	51	54	51
Age at scan (median and range)		62	25 – 82	62	25- 82
Side	Left	17	49	51	49
	Right	18	51	54	51
Hypertension		16	47	34	32
Rheumatism		3	9	6	6
Atherosclerosis		10	29	15	14
Cardiac disease		5	15	21	20
Diabetes		3	9	7	7
Connective tissue disease		2	6	0	0

3.5.4 The correlation of TI, curvature and torsion in ECAA subjects compared to control group without presence of ECAA

Mann-Whitney U test for unrelated subjects was used to compare measured TI, curvature and torsion in 33 affected carotid arteries from the ECAA-group and 92 unaffected carotid arteries from the control group. Due to uncertainties in the exported CLL, respectively 2 and 13 subjects were excluded from analysis. Median TI, medium and high curvature are higher within ECAA subject group. Moreover, significant difference between ECAA and control group were seen within measured TI, medium and high curvature classes and low torsion class. Low curvature and high torsion classes are considered as not significantly different (Table 13).

3.5.5 Correlation of measured tortuosity index, curvature and torsion in the carotid artery

Pearson's correlation was used to find the correlation between measured TI and in Table 8 predefined curvature and torsion groups. For correlation coefficient calculation, 155 cases were included. Strongest positive correlation was found between TI and medium curvature (0.791). In addition, also strong positive correlation was seen between, TI and high curvature (0.686), medium and high curvature (0.677), low torsion and low curvature (0.556) and low torsion and medium curvature (0.473). Negative correlation was found between TI and low curvature (- 0.114) low curvature and medium curvature (- 0.098), low curvature and high curvature (- 0.197). All strong positive correlation outcomes described above show significant p-values whereas only the negative correlation outcome between low and high curvature was significant. Table 14 presents an overview of correlation in TI, curvature and torsion.

Table 12: CA median TI, curvature and torsion values in cases with ECAA compared with own contralateral CA. Values between brackets are minimum and maximum values of TI, curvature and torsion.

		ECAA n=33	Contralateral side n=30	p-value
TI		1.245 (1.046 – 1.793)	1.232 (1.023 – 1.943)	0.581
Curvature	Low	186 (147 – 230)	195.5 (148 – 240)	0.632
	Medium	40 (23 – 60)	39 (5 – 61)	0.349
	High	5 (0 – 15)	4.5 (0 – 20)	0.144
Torsion	Low	227 (177 – 252)	229 (177 – 259)	0.719
	High	7 (1 – 13)	7 (1 – 16)	0.222

Table 13: CA median TI, curvature and torsion values in cases with ECAA compared with carotid arteries from control group. Values between brackets are minimum and maximum values of TI, curvature and torsion.

		ECAA n=33	Control n=92	p-value
TI		1.245 (1.046 – 1.793)	1.098 (1.018 – 1.302)	0.000
Curvature	Low	186 (147 – 230)	189 (139 – 234)	0.716
	Medium	40 (23 – 60)	24 (2 – 52)	0.000
	High	5 (0 – 15)	0 (0 – 11)	0.000
Torsion	Low	227 (177 – 252)	200 (159 – 252)	0.000
	High	7 (1 – 13)	6 (2 – 12)	0.203

Table 14: Correlation of measured TI, low, medium and high curvature and low and high torsion (n = 155). Values between brackets are calculated p-values.

		TI	Curvature			Torsion	
			Low	Medium	High	Low	High
TI		1	- 0.114 (0.157)	0.791 (0.000)	0.686 (0.000)	0.331 (0.000)	0.185 (0.021)
Curvature	Low	- 0.114 (0.157)	1	- 0.098 (0.225)	- 0.197 (0.014)	0.556 (0.000)	0.341 (0.000)
	Medium	0.791 (0.000)	- 0.098 (0.225)	1	0.677 (0.000)	0.473 (0.000)	0.124 (0.123)
	High	0.686 (0.000)	- 0.197 (0.014)	0.677 (0.000)	1	0.270 (0.001)	0.042 (0.601)
Torsion	Low	0.331 (0.000)	0.556 (0.000)	0.473 (0.000)	0.270 (0.001)	1	0.206 (0.010)
	High	0.185 (0.021)	0.341 (0.000)	0.124 (0.123)	0.042 (0.601)	0.206 (0.010)	1

3.6 Discussion

The aim of this study was to find out if and how tortuosity index, curvature and torsion relate to each other in the CA. Geometry measurements were compared in aneurysm-affected CAs and their gender- and age-matched control CAs. First inter- and intraobserver agreement was assessed, showing excellent reliability and low $CV_{\%mean}$ in ICA, CCA and CA. Second, no significant difference was seen in TI, curvature and torsion when comparing the ipsi- and contralateral side within the patient with an unilateral CA aneurysm, whereas comparing ECAA subjects with those of the control group resulted in significant differences in all measurements. Furthermore, a strong positive correlation is seen between TI, medium curvature and high curvature. In addition, a strong positive correlation was seen between low torsion, low curvature and medium curvature.

3.6.1 Tortuosity index measurement reproducibility

According to the reliability classes as defined by Koo and Li[33], both inter- and intraobserver agreement reliability scored very high for TI measurements in the ICA, CCA and CA (Table 9 and Table 10). In addition, created Bland-Altman plots for inter- and intraobserver agreement show that limits of agreement are only exceeded by less than 10% of the used dataset and measurements show no systematic bias (Figure 20 and Figure 21). Therefore, TI measurements looks reproducible. However, ICC only determines the ratio of inter- and intraobserver differences. Consequently, reliability and reproducibility will still be high when both observers include similar TI measurement errors. To ensure measurement accuracy is also high, $CV_{\%mean}$ is used to provide information about the variability in terms of TI unit of measurement.[37] This means that the actual TI lies with a probability of 95% within the range of $CV_{\%mean}$ of the performed measurement. As a result, it means that the lower the $CV_{\%mean}$, the higher the accuracy of the TI measurements performed. When looking at all calculated $CV_{\%mean}$ percentages in Table 9 and Table 10, it is striking that the highest value is only 6.35%, since this means the measurements can be considered accurate. The excellent variability, the high precision and the low $CV_{\%mean}$, ensure that the TI measurements can be considered reproducible.

Although measurements reproducibility has been demonstrated, ICC and $CV_{\%mean}$ outcomes for assessment of intraobserver agreement in Table 10 show better results for observer 2. While analyzing TI measurements, four possible causes for this difference were found. First, used 3Mensio software is developed and designed for aortic applications. Therefore, the four points for CLL creation are usually placed above the aneurysm, within the aneurysm and within the left and right iliac branch instead of the selected measurement locations described in section 3.4.2. Moreover, for drawing the CLL it is important that there is a sufficient amount of contrast agent within the CA. Primarily, because 3Mensio only enables its users to place the above described points on a segmented area. But secondly, because higher contrast levels at for example the nearby internal jugular vein will possibly result in a false-drawn CLL. In most cases, the automatically signed CLL therefore had to be corrected manually. Since correction of the signed CLL is observer dependent, there will always be a slight variation in the measurements. However, as long as the CA is clearly distinguishable from its surrounding anatomy, this variation was not significant. Second, in some cases it was difficult to distinguish the course of the CA due to the presence of scatter artifacts, an insufficient amount of contrast within the artery or a combination of both. In the case of scatter artifacts present, usually only a part of the CLL had to be drawn manually. The degree of tortuosity in combination with present contrast in the scattered area determined the ease with which the CLL could be drawn. With increasing tortuosity or decreasing contrast, the variation between the measurements will probably be higher, because there will be

more difference between the drawn CLL. Third, in five cases observer 1 measured TI of the wrong carotid artery. Four times within the first measurement round and one time within the second. As the course of both CA's will never be the same, measuring the contralateral side ensures that there will be a difference in measured TI. Nonetheless, it is true that the influence of measuring the wrong contralateral side is small as long as the degree of tortuosity and the straight distance on both sides is approximately equal. Finally, during the analysis it appeared that at the start of the first round of measurements observer 1 drew the CLL of the CCA from the carotid bifurcation to the origin of the brachiocephalic artery while observer 2 did this only up to the origin of the CCA. Because in most cases the increase in CLL length is higher than the increase in straight distance, a difference in measured TI will also arise as a result and therefore will also influence calculated inter- and intraobserver agreement. Due to the fact that the intraobserver agreement of observer 2 was assessed as better than that of observer 1 and observer 2 performed all measurements according to the protocol, it was therefore decided that for further analysis only the measured TI, curvature and torsion values of observer 2 were used.

3.6.2 Curvature and torsion measurements

Exported 1mm interpolated CLL coordinates files from 3Mensio were used to calculate curvature and torsion of CA. First, alignment of CT DICOM-files and exported CLL was checked. Nine exported CLL's showed misalignment with the corresponding DICOM-files and were therefore excluded from further analysis (Figure 22A). Analyzing differences between misaligned CLL's and aligned CLL's showed that DICOM image orientation was slightly rotated within misaligned CLL's. Although it should be theoretically possible to align the CLL and the DICOM files with the help of a rotation and translation matrix, it turned out that this was not possible in practice. In all likelihood, this misalignment does not change the length and direction of the exported CLL and could therefore be used for curvature and torsion calculations without generating measurement errors. However, it cannot be demonstrated that this is actually the case and it has therefore been decided to exclude these cases for curvature and torsion analysis. Second, during data analysis it was also found that the exported CLL did not follow the course of the CCA in nine cases (Figure 22B). This error in the exported CLL is caused by the fact that 3Mensio was developed to draw a CLL from the point placed in the aortic aneurysm to the points that are placed in two iliac branches. However, in this study we place the two measurement points, as described in the section 3.4.2, left and right of the origin of the CCA. This ensures that the software draws two CLL which should follow the course of the CCA. Due to the problems mentioned in section 3.6.1, it may be possible that one or both of the CLL are not drawn correctly. One of the two CLL is then corrected to be able to calculate the TI after which it is exported from 3Mensio. However, in some cases the uncorrected instead of the corrected CLL has been exported. Since the cases were not stored in 3Mensio, it was not possible to still export the corrected CLL and therefore also these cases were excluded from further analysis.

For curvature and torsion measurements, in section 3.4.3 described equations for curvature and torsion are implemented in MATLAB. Implementation correctness was verified using a helix with parametrization in cartesian coordinates: $x(t) = \mathrm{acos}\,(t)$, $y(t) = \mathrm{asin}(t)$ and $z(t) = bt$, where a is the radius and $2\pi b$ the pitch and analytical equations derived from the original curvature and torsion equation. As verification outcomes showed outcome of 0.5 for both curvature and torsion when $a = 1$ and $b = 1$, implementation in MATLAB was considered successful. During the analysis of the measured curvature and torsion, extremely high and deviating values were nevertheless found in some cases. Most likely this is due to the use of the exported coordinates

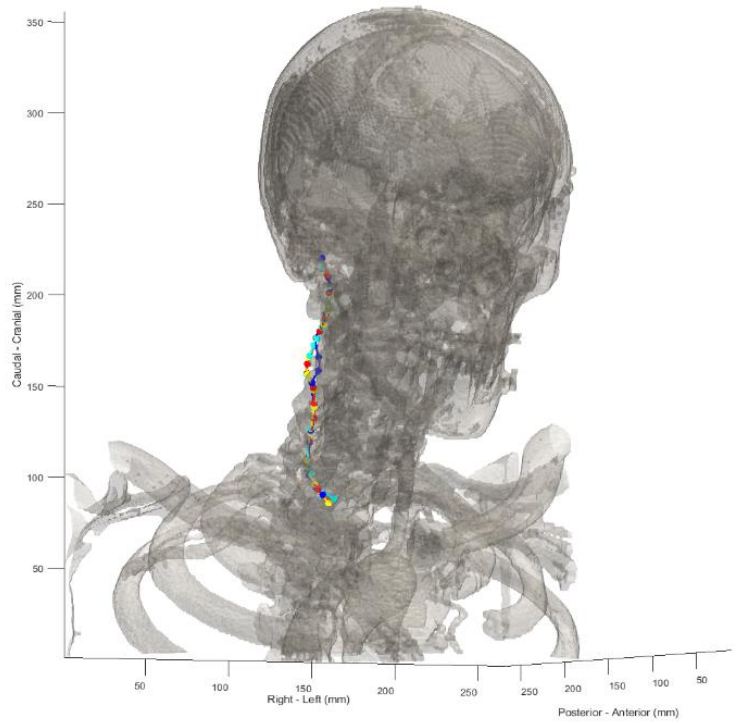

A

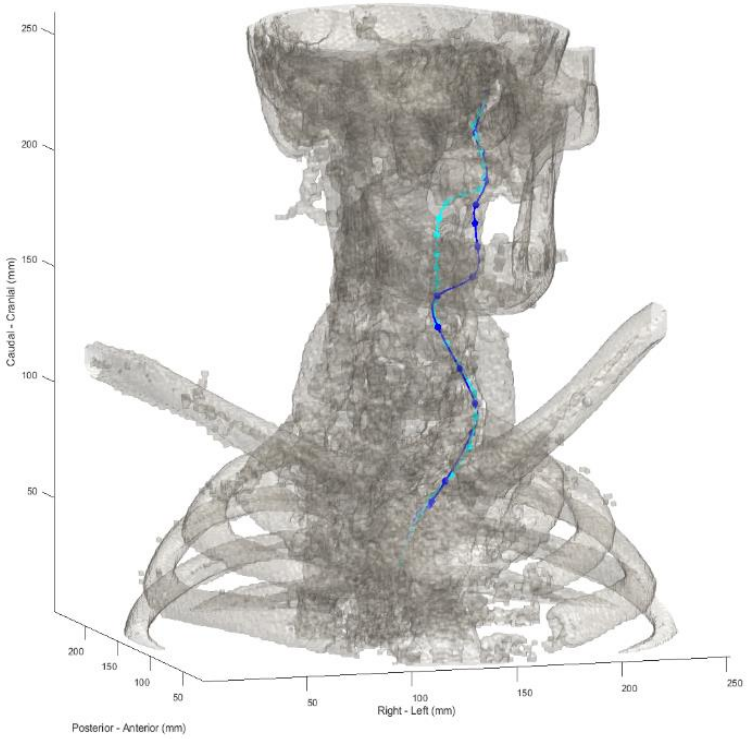

B

Figure 22: Overview of incorrect alignment of exported CLL and corresponding DICOM-files (A) and incorrect exported CLL-coordinates (B). In figure A exported CLL's lie behind created segmented area. In figure B, CLL from observer one (light blue) and observer 2 (blue) follow different pathways suggesting incorrect CLL placement.

instead of the coordinates of a newly interpolated line, as curvature and torsion are both very point-specific and very sensitive to geometric data.[68] However, very large deviations were rare and it was therefore decided not to exclude these cases from the analysis.

3.6.3 Correlation of TI, and curvature and torsion

The correlation of TI, and curvature and torsion was determined for measured outcomes of ipsi- and contralateral carotid arteries in a group with ECAA. In addition, the correlation was also determined for measured outcomes of carotid arteries with ECAA and a matched control group without presence of ECAA. No significant difference for TI, and curvature and torsion was found between CA of ECAA cases and therefore affected and unaffected CA were considered as equally tortuous. On the other hand, a significant difference was found in the comparison between the ECAA group and the control group for TI, medium and high curvature and low torsion. Furthermore, most values from the correlation table showed somewhat expected outcomes. For example, it is logical that high TI shows a strong positive correlation with the medium and high curvature group, since a higher TI value means that the CLL of the CA is longer than the straight distance and therefore in all likelihood also has a more tortuous course. On the other hand, there is a higher positive correlation between TI and the low torsion group, where the expectation is that this would actually be the other way around. When the not significantly different low curvature and high torsion are analyzed, it is striking that the median and maximum and minimum found are closer to each other than is seen within the significantly different measurements. In the case of the measured curvature values, the outcome seems logical, since only a significant difference is seen when the CA's show a more tortuous course. However, the same would be expected with torsion, but in this case torsion is significantly different in the low group instead of the high group. An explanation could be that for this study the chosen cut-off values for both the curvature and the torsion groups are arbitrarily chosen. As more has been described concerning the application of curvature measurements than for torsion, the selected curvature cut-off values are likely to be more accurate. Moreover, curvature measurements are easier to interpret than the relatively abstract torsion measurements. It is therefore advisable to find out in a subsequent study what the best cut-off values for curvature and (mainly) torsion in the CA are. Furthermore, in this study it was decided to calculate the curvature and torsion for each data point of the exported 1mm interpolated CLL instead of looking at line segments. This ensures that the number of points in the groups depends on the length of the CLL. For example, when kinking is involved, it is likely that a high curvature or torsion is less often measured compared to cases involving tortuosity or coiling while its importance is not less significant. Although there will always be a certain ratio between the length of the CLL and the number of available data points, it may be better to think in line sections compared to curvature and torsion per point. In this way it is ensured that the cases are easier to compare, because the difference in length between the cases is less important. On the other hand, dividing into segments ensures that an incorrectly measured high curvature can have a major influence on the assessment of the vessel, because the influence of this segment will be much greater than the ratio of many well measured points. Finally, although mathematically, curvature and torsion complement each other, the question is whether determining the torsion is clinically of added value. During the analysis of the curvature and torsion measurements, it turned out that a high curvature can be found in a tortuous area, while this is not the case for a high torsion. From a clinical point of view, it is more interesting to know whether the artery makes a sharp turn instead of the direction in which the artery deviates from its original course, because the direction of rotation hardly gives any information about the DICA type. Therefore, it seems to be the most important at present to determine good cut-off values for the curvature, to do more

research into the correlation between TI and curvature, and finally to find out whether the calculated TI and curvature are also a predictive measure for development of an ECAA.

3.7 Conclusion

Both the inter and the intra observer agreement for TI measurements showed excellent reliability and agreement, indicating that the measurements are reproducible. This study showed that geometry of the carotids in terms of tortuosity index, curvature and torsion, seems to be comparable within patients with a carotid aneurysm, but in comparison with control patients seems strikingly different. Additionally, a strong and positive correlation was found between true length and sharp bends of the carotid arteries.

Chapter 4: General discussion

Two research aims were defined at the beginning of this thesis. First aim was to develop a technique capable of automatically measuring arterial depth in the lower extremities. Since there is no ground truth with regard to performing automatic depth measurements in the lower extremities, it has first been investigated whether manual measurements can be considered reliable and reproducible. This showed that manually performed measurements in the SFA and PTA both showed excellent reliability and agreement and can therefore be regarded as ground truth. Subsequently, an automatic depth measurement technique was developed in MATLAB that measures the depth of arteries in the lower extremities. The following technique requirements were determined in advance: maximum measurement deviation of 3mm, arteries, bone and skin must be segmented separately and measuring time should not exceed 15 minutes. Validation showed that only the stated requirement of a maximum measuring deviation of 3mm was achieved and that the development of the automatic measuring technique would therefore not be successful. However, data analysis showed that in all cases that exceeded set segmentation and time limit requirements, only additional erroneous measurements have been performed due to the inclusion of bone regions in the arterial segmentation. Improving the segmentation of the anatomical structure is therefore likely to lead to the achievement of all requirements. Therefore, the developed technique is considered acceptable. Finally, manual and automatic depth measurements in the SFA were compared, demonstrating excellent reliability and agreement. It is therefore possible in any case to measure the arterial depth of the lower extremities at the level of the SFA using the developed automatic depth measurement technique. Second aim of this thesis was to address the clinical implication of CA geometry expressed in tortuosity index (TI), curvature and torsion. This study showed that geometry of the carotids in terms of tortuosity index, curvature and torsion, seems to be comparable within patients with a carotid aneurysm, but in comparison with control patients seems strikingly different. Additionally, a strong and positive correlation was found between true length and sharp bends of the carotid arteries.

To conclude, first steps have been taken in this thesis for both automatically measuring arterial depth in the lower extremities and for addressing the clinical implication of CA geometry expressed in TI, curvature and torsion. In case of the developed automatic depth measuring technique it is important to improve the segmentation outcomes. This will increase accuracy of the performed measurements and will also decrease measurement time. Furthermore, it is necessary to investigate the influence of the fact that the segmentation method used for the arterial segments only segments the vascular lumen. It should also be investigated whether the technique is able to measure the arterial depth in the entire lower extremity, rather than only at the level of the SFA. When the segmentations are improved and the technique is able to also include the arterial vessel wall in the arterial segmentation, it is likely in the future to use the outcome of the depth measurement technique to plan and perform a transcutaneous treatment method. In addition, the application of this technique can also be extended to, for example, the upper extremities. On the other hand, in the curvature and torsion measurements performed in the CA, it is important that the implications of both values are examined in particular. It is important to find out the best cut-off values for the drawn curvature and torsion classes, as these were chosen arbitrarily in this study. Subsequently, it can be examined what the predictive value of TI, curvature and torsion on possible development an ECAA can be.

Bibliography

1. World Health Organization. Cardiovascular diseases (CVDs). World Health Organization. https://www.who.int/en/news-room/fact-sheets/detail/cardiovascular-diseases-(cvds). Published 2019. Accessed February 27, 2019.

2. Roth GA, Johnson C, Abajobir A, et al. Global, Regional, and National Burden of Cardiovascular Diseases for 10 Causes, 1990 to 2015. *J Am Coll Cardiol*. 2017;70(1):1-25. doi:10.1016/j.jacc.2017.04.052

3. Townsend N, Wilson L, Bhatnagar P, Wickramasinghe K, Rayner M, Nichols M. Cardiovascular disease in Europe: epidemiological update 2016. *Eur Heart J*. 2016;37(42):3232-3245. doi:10.1093/eurheartj/ehw334

4. Timmis A, Townsend N, Gale C, et al. European Society of Cardiology: Cardiovascular Disease Statistics 2017. *Eur Heart J*. 2018;39(7):508-579. doi:10.1093/eurheartj/ehx628

5. National heart lung and blood institute. Peripheral Artery Disease. National heart lung and blood institute. https://www.nhlbi.nih.gov/health-topics/peripheral-artery-disease. Published 2020. Accessed March 13, 2020.

6. Diehm N, Shang A, Silvestro A, et al. Association of Cardiovascular Risk Factors with Pattern of Lower Limb Atherosclerosis in 2659 Patients Undergoing Angioplasty. *Eur J Vasc Endovasc Surg*. 2006;31(1):59-63. doi:10.1016/j.ejvs.2005.09.006

7. Ozkan U, Oguzkurt L, Tercan F. Atherosclerotic Risk Factors and Segmental Distribution in Symptomatic Peripheral Artery Disease. *J Vasc Interv Radiol*. 2009;20(4):437-441. doi:10.1016/j.jvir.2009.01.010

8. Rafieian-Kopaei M, Setorki M, Doudi M, Baradaran A, Nasri H. Atherosclerosis: process, indicators, risk factors and new hopes. *Int J Prev Med*. 2014;5(8):927-946. http://www.ncbi.nlm.nih.gov/pubmed/25489440.

9. Mayo Clinic staff. Peripheral artery disease (PAD); Diagnosis & Treatment. Mayo Clinic. https://www.mayoclinic.org/diseases-conditions/peripheral-artery-disease/diagnosis-treatment/drc-20350563. Published 2019. Accessed March 11, 2019.

10. Morcos R, Louka B, Tseng A, et al. The Evolving Treatment of Peripheral Arterial Disease through Guideline-Directed Recommendations. *J Clin Med*. 2018;7(1):9. doi:10.3390/jcm7010009

11. Fowkes FGR, Aboyans V, Fowkes FJI, McDermott MM, Sampson UKA, Criqui MH. Peripheral artery disease: epidemiology and global perspectives. *Nat Rev Cardiol*. 2017;14(3):156-170. doi:10.1038/nrcardio.2016.179

12. John Hopkins Vascular and Interventional Radiology. Percutaneous Transluminal Angioplasty. John Hopkins medicine. https://www.hopkinsmedicine.org/interventional-radiology/procedures/pta/. Published 2020. Accessed February 25, 2020.

13. Shishehbor MH, Jaff MR. Percutaneous Therapies for Peripheral Artery Disease. *Circulation*. 2016;134(24):2008-2027. doi:10.1161/CIRCULATIONAHA.116.022546

14. Mahmud E, Cavendish JJ, Salami A. Current Treatment of Peripheral Arterial Disease. *J Am Coll Cardiol*. 2007;50(6):473-490. doi:10.1016/j.jacc.2007.03.056

15. Jones DW, Schanzer A, Zhao Y, et al. Growing Impact of Restenosis on the Surgical Treatment of Peripheral Arterial Disease. *J Am Heart Assoc*. 2013;2(6). doi:10.1161/JAHA.113.000345

16. Copelan A, Hartman J, Chehab M, Venkatesan A. High-Intensity Focused Ultrasound: Current Status for Image-Guided Therapy. *Semin Intervent Radiol*. 2015;32(04):398-415. doi:10.1055/s-0035-1564793

17. Shaw CJ, ter Haar GR, Rivens IH, Giussani DA, Lees CC. Pathophysiological mechanisms of high-intensity focused ultrasound-mediated vascular occlusion and relevance to non-invasive fetal surgery. *J R Soc Interface*. 2014;11(95):20140029. doi:10.1098/rsif.2014.0029

18. Burks SR, Ziadloo A, Hancock HA, et al. Investigation of Cellular and Molecular Responses to Pulsed Focused Ultrasound in a Mouse Model. Rojas M, ed. *PLoS One*. 2011;6(9):e24730. doi:10.1371/journal.pone.0024730

19. Criqui MH, Aboyans V. Epidemiology of Peripheral Artery Disease. *Circ Res*. 2015;116(9):1509-1526. doi:10.1161/CIRCRESAHA.116.303849

20. Chen Q, Shi Y, Wang Y, Li X. Patterns of Disease Distribution of Lower Extremity Peripheral Arterial Disease. *Angiology*. 2015;66(3):211-218. doi:10.1177/0003319714525831

21. Crowther MA. Pathogenesis of Atherosclerosis. *Hematology*. 2005;2005(1):436-441. doi:10.1182/asheducation-2005.1.436

22. Insull W. The Pathology of Atherosclerosis: Plaque Development and Plaque Responses to Medical Treatment. *Am J Med*. 2009;122(1):S3-S14. doi:10.1016/j.amjmed.2008.10.013

23. Singh RB, Mengi SA, Xu Y-J, Arneja AS, Dhalla NS. Pathogenesis of atherosclerosis: A multifactorial process. *Exp Clin Cardiol*. 2002;7(1):40-53. http://www.ncbi.nlm.nih.gov/pubmed/19644578.

24. Singh P, Harper Y, Oliphant CS, et al. Peripheral interventions and antiplatelet therapy: Role in current practice. *World J Cardiol*. 2017;9(7):583. doi:10.4330/wjc.v9.i7.583

25. The British Journal of Cardiology. Lipids module 1: lipid metabolism and its role in atherosclerosis. The British Journal of Cardiology. https://bjcardio.co.uk/2015/07/lipids-module-1-lipid-metabolism-and-its-role-in-atherosclerosis-3/. Published 2016. Accessed March 4, 2019.

26. Zhou Y-F. High intensity focused ultrasound in clinical tumor ablation. *World J Clin Oncol*. 2011;2(1):8. doi:10.5306/wjco.v2.i1.8

27. Hsiao Y-H, Kuo S-J, Tsai H-D, Chou M-C, Yeh G-P. Clinical Application of High-intensity Focused Ultrasound in Cancer Therapy. *J Cancer*. 2016;7(3):225-231. doi:10.7150/jca.13906

28. Orsi F, Zhang L, Arnone P, et al. High-Intensity Focused Ultrasound Ablation: Effective and Safe Therapy for Solid Tumors in Difficult Locations. *Am J Roentgenol*. 2010;195(3):W245-W252. doi:10.2214/AJR.09.3321

29. Almekkaway MK, Shehata IA, Ebbini ES. Anatomical-based model for simulation of HIFU-induced lesions in atherosclerotic plaques. *Int J Hyperth*. 2015;31(4):433-442. doi:10.3109/02656736.2015.1018966

30. Shehata IA, Ballard JR, Casper AJ, Liu D, Mitchell T, Ebbini ES. Feasibility of Targeting Atherosclerotic Plaques by High-Intensity–focused Ultrasound: An In Vivo Study. *J Vasc Interv Radiol*. 2013;24(12):1880-1887.e2. doi:10.1016/j.jvir.2013.08.013

31. Damianou C, Christofi C, Mylonas N. Removing atherosclerotic plaque created using high cholesterol diet in rabbit using ultrasound. *J Ther Ultrasound*. 2015;3(1):3. doi:10.1186/s40349-015-0025-8

32. McGraw KO, Wong SP. Forming inferences about some intraclass correlation coefficients. *Psychol Methods*. 1996;1(1):30-46. doi:10.1037/1082-989X.1.1.30

33. Koo TK, Li MY. A Guideline of Selecting and Reporting Intraclass Correlation Coefficients for Reliability Research. *J Chiropr Med*. 2016;15(2):155-163. doi:10.1016/j.jcm.2016.02.012

34. Bartlett JW, Frost C. Reliability, repeatability and reproducibility: analysis of measurement errors in continuous variables. *Ultrasound Obstet Gynecol*. 2008;31(4):466-475. doi:10.1002/uog.5256

35. Bland JM, Altman DG. Statistical methods for assessing agreement between two methods of clinical measurement. *Lancet (London, England)*. 1986;1(8476):307-310. http://www.ncbi.nlm.nih.gov/pubmed/2868172.

36. Bland JM, Altman DG. Agreement Between Methods of Measurement with Multiple Observations Per Individual. *J Biopharm Stat*. 2007;17(4):571-582. doi:10.1080/10543400701329422

37. Leijenaar RTH, Carvalho S, Velazquez ER, et al. Stability of FDG-PET Radiomics features: An integrated analysis of test-retest and inter-observer variability. *Acta Oncol (Madr)*. 2013;52(7):1391-1397. doi:10.3109/0284186X.2013.812798

38. Barnhart HX, Barboriak DP. Applications of the repeatability of quantitative imaging biomarkers: a review of statistical analysis of repeat data sets. *Transl Oncol*. 2009;2(4):231-235. http://www.ncbi.nlm.nih.gov/pubmed/19956383.

39. N/A. *Instructions for Use v1.0 : ICC HIFU-SynthesizerTM System Module 1.1*. Edina www.hifu-rx.com.

40. Mathworks. imwarp. Mathworks. https://www.mathworks.com/help/images/ref/imwarp.html. Published 2020. Accessed February 9, 2020.

41. NEMA. C.7.6.2 Image Plane Module. DICOM. http://dicom.nema.org/medical/dicom/current/output/chtml/part03/sect_C.7.6.2.html. Published 2020. Accessed February 9, 2020.

42. Frangi AF, Niessen WJ, Vincken KL, Viergever MA. Multiscale vessel enhancement filtering. In: ; 1998:130-137. doi:10.1007/BFb0056195

43. Jerman T, Pernuš F, Likar B, Špiclin Ž. Beyond Frangi: an improved multiscale vesselness filter. In: Ourselin S, Styner MA, eds. ; 2015:94132A. doi:10.1117/12.2081147

44. Mathworks. bwlabeln. Mathworks. https://www.mathworks.com/help/images/ref/bwlabeln.html. Published 2020. Accessed February 10, 2020.

45. Patrick S, Birur Np, Gurushanth K, Raghavan As, Gurudath S. Comparison of gray values of cone-beam computed tomography with hounsfield units of multislice computed tomography: An in vitro study. *Indian J Dent Res*. 2017;28(1):66. doi:10.4103/ijdr.IJDR_415_16

46. Lorbeer R, Grotz A, Dörr M, et al. Reference values of vessel diameters, stenosis prevalence, and arterial variations of the lower limb arteries in a male population sample using contrast-enhanced MR angiography. Gadeau A-P, ed. *PLoS One*. 2018;13(6):e0197559. doi:10.1371/journal.pone.0197559

47. Lee KC, Bamford A, Gardiner F, et al. Investigating the intra- and inter-rater reliability of a panel of subjective and objective burn scar measurement tools. *Burns*. 2019;45(6):1311-1324. doi:10.1016/j.burns.2019.02.002

48. Analan PD, Yilmaz EE, Adam M, Leblebici B. The effect of physician experience on the measurement reliability of the Reimers' hip migration percentage in children with cerebral palsy. *J Phys Ther Sci*. 2015;27(10):3255-3258. doi:10.1589/jpts.27.3255

49. Barrett JF, Keat N. Artifacts in CT: Recognition and Avoidance. *RadioGraphics*. 2004;24(6):1679-1691. doi:10.1148/rg.246045065

50. Philips Healthcare. Philips IQon Elite spectral CT. 2018. https://www.philips.co.uk/c-dam/b2bhc/gb/resource-catalog/landing/brightontender/ct-iqon-elite-spectral-ct-product-specification-lr.pdf.

51. Hemalatha RJ, Thamizhvani TR, Dhivya AJA, Joseph JE, Babu B, Chandrasekaran R. Active Contour Based Segmentation Techniques for Medical Image Analysis. In: *Medical and Biological Image Analysis*. InTech; 2018. doi:10.5772/intechopen.74576

52. Luis R, Mara A, Azzato F, Milei J. Carotid Artery – Pathology, Plaque Structure – Relationship between Histological Assessment, Color Doppler Ultrasonography and Magnetic Resonance Imaging – Dolichoarteriopathies – Barorreceptors. In: *Carotid Artery Disease - From Bench to Bedside and Beyond*. InTech; 2014. doi:10.5772/57157

53. Arslan Y, Arslan İB, Pekçevik Y, Şener U, Köse Ş, Zorlu Y. Matrix Metalloproteinase Levels in Cervical and Intracranial Carotid Dolichoarteriopathies. *J Stroke Cerebrovasc Dis*. 2016;25(9):2153-2158. doi:10.1016/j.jstrokecerebrovasdis.2016.05.028

54. Yu J, Qu L, Xu B, et al. Current Understanding of Dolichoarteriopathies of the Internal Carotid Artery: A Review. *Int J Med Sci*. 2017;14(8):772-784. doi:10.7150/ijms.19229

55. Togay-Işikay C, Kim J, Betterman K, et al. Carotid artery tortuosity, kinking, coiling: stroke risk factor, marker, or curiosity? *Acta Neurol Belg*. 2005;105(2):68-72. http://www.ncbi.nlm.nih.gov/pubmed/16076059.

56. Metz H, Murray-Leslie RM, Bannister RG, Bull JW, Marshall J. Kinking of the internal carotid artery. *Lancet (London, England)*. 1961;1(7174):424-426. http://www.ncbi.nlm.nih.gov/pubmed/13769898.

57. Weibel J, Fields WS. Tortuosity, coiling, and kinking of the internal carotid artery: II. Relationship of morphological variation to cerebrovascular insufficiency. *Neurology*. 1965;15(5):462-462. doi:10.1212/WNL.15.5.462

58. Sacco S, Totaro R, Baldassarre M, Carolei A. Morphological variations of the internal carotid artery: Prevalence, characteristics and association with cerebrovascular disease.

Int J Angiol. 2007;16(2):59-61. http://www.ncbi.nlm.nih.gov/pubmed/22477273.

59. Phan TG, Beare RJ, Jolley D, et al. Carotid Artery Anatomy and Geometry as Risk Factors for Carotid Atherosclerotic Disease. *Stroke*. 2012;43(6):1596-1601. doi:10.1161/STROKEAHA.111.645499

60. Pancera P, Ribul M, Presciuttini B, Lechi A. Prevalence of carotid artery kinking in 590 consecutive subjects evaluated by Echocolordoppler. Is there a correlation with arterial hypertension? *J Intern Med*. 2000;248(1):7-12. doi:10.1046/j.1365-2796.2000.00611.x

61. Prencipe G, Pellegrino L, Vairo F, Tomaiuolo M, Furio OA. [Dolichoarteriopathy (kinking, coiling,tortuosity) of the carotid arteries and cardiovascular risk factors]. *Minerva Cardioangiol*. 46(1-2):1-7. http://www.ncbi.nlm.nih.gov/pubmed/9780615.

62. Pellegrino L, Prencipe G, Ferrara V, Correra M, Pellegrino PL. [Bilateral and monolateral dolichoarteriopathies (Kinking, Coiling, Tortuosity) of the carotid arteries and atherosclerotic disease. An ultrasonographic study]. *Minerva Cardioangiol*. 2002;50(1):15-20. http://www.ncbi.nlm.nih.gov/pubmed/11830714.

63. Saba L, Argiolas GM, Sumer S, et al. Association between internal carotid artery dissection and arterial tortuosity. *Neuroradiology*. 2015;57(2):149-153. doi:10.1007/s00234-014-1436-x

64. Kamenskiy A V., Pipinos II, Carson JS, MacTaggart JN, Baxter BT. Age and disease-related geometric and structural remodeling of the carotid artery. *J Vasc Surg*. 2015;62(6):1521-1528. doi:10.1016/j.jvs.2014.10.041

65. Schuurmann RCL, Kuster L, Slump CH, et al. Aortic Curvature Instead of Angulation Allows Improved Estimation of the True Aorto-iliac Trajectory. *Eur J Vasc Endovasc Surg*. 2016;51(2):216-224. doi:10.1016/j.ejvs.2015.09.008

66. Schuurmann RCL, van Noort K, Overeem SP, et al. Aortic Curvature Is a Predictor of Late Type Ia Endoleak and Migration After Endovascular Aneurysm Repair. *J Endovasc Ther*. 2017;24(3):411-417. doi:10.1177/1526602817700378

67. Schuurmann RCL, Ouriel K, Muhs BE, et al. Aortic curvature as a predictor of intraoperative type Ia endoleak. *J Vasc Surg*. 2016;63(3):596-602. doi:10.1016/j.jvs.2015.08.110

68. Kamenskiy A V., MacTaggart JN, Pipinos II, Bikhchandani J, Dzenis YA. Three-Dimensional Geometry of the Human Carotid Artery. *J Biomech Eng*. 2012;134(6). doi:10.1115/1.4006810

69. de Vries EE, Pourier VEC, van Laarhoven CJHCM, Vonken EJ, van Herwaarden JA, de Borst GJ. Comparability of semiautomatic tortuosity measurements in the carotid artery. *Neuroradiology*. 2019;61(2):147-153. doi:10.1007/s00234-018-2112-3

70. Pressley A. *Elementary Differential Geometry*. London: Springer London; 2010. doi:10.1007/978-1-84882-891-9

71. Software T. How To Find Relationship Between Variables, Multiple Regression. TIBCO Software Inc. http://www.statsoft.com/textbook/multiple-regression. Published 2019. Accessed March 21, 2019.

Appendix A

Protocol manuele dieptemetingen

Laad dataset

Start PACS/Hix en open de juiste casus in PACS. Open ook het knipprogramma van Windows.

Locatie anatomische landmarks

Gebruik voor het uitvoeren van de dieptemetingen altijd de transversale slices van CTA 3/3 serie. Coronale en sagittale slice kunnen eventueel voor orientatie worden gebruik.

Dieptemetingen dienen op anatomische landmarks uitgevoerd te worden. Alle landmarks zijn gedefinieerd op de 1e slice waarop de origo van arteriën zichtbaar is, wanneer van craniaal naar caudaal door de dataset heen wordt gescrold. De landmarks zijn gelokaliseerd op de volgende locaties:

1. Origo iliaca externa
2. Origo femoralis superficialis
3. Poplitea (thv eerste slice waarop Patella niet te zien is)
4. Origo tibialis anterior
5. Origo tibialis posterior

Uitvoeren dieptemetingen

1. Zoek de eerste anatomische landmark op in de transversale weergave.
2. Selecteer in 3mensio de functie om afstanden te berekenen en voer dit uit op de volgende manieren:
    a. Trek een verticale, rechte lijn vanaf dorsale arteriewand naar de huid aan de ventrale zijde.
    b. Trek een verticale, rechte lijn vanaf ventrale arteriewand naar de huid aan de dorsale zijde.
    c. Trek een horizontale, rechte lijn vanaf de laterale arteriewand naar de huid aan de mediale zijde.
    d. Trek een horizontale, rechte lijn vanaf mediale arteriewand naar de huid aan de laterale zijde.
    e. Bepaal op het oog wat jij de kortste afstand van de contralaterale zijde van de vaatwand ten opzichte van de huid vindt en trek hier een rechte lijn tussen.
3. Nadat alle lijnen op een meetpunt zijn getrokken, maak je een Printscreen met behulp van het knipprogramma van Windows (zie figuur 1 & 2). Zorg ervoor dat de informatie linksonder op het scherm wordt mee geknipt. Afhankelijk van het meetmoment en observer sla je deze als volgt op:[observer-studienummer-locatie].
   Vb 1e keer meten: CH1-L01-1, FS1-L01-1, JK1-L01-1
   Vb 2e keer meten: CH2-L01-1, FS2-L01-1, JK2-L01-1
4. Verwijder alle metingen op het meetpunt en ga door naar de volgende anatomische landmark.

Herhaal de stappen 1 t/m 5 voor alle aangegeven anatomische landmarks.

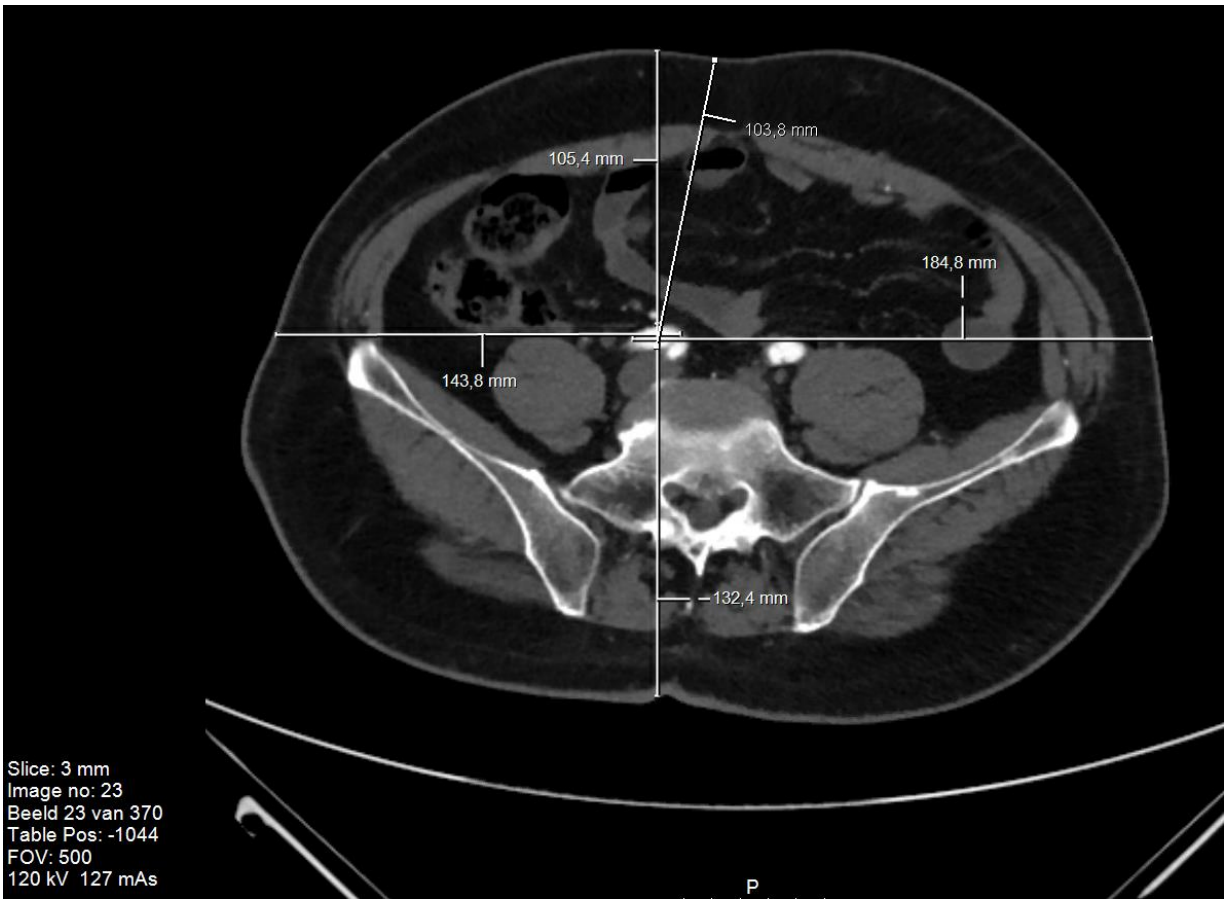

Figure 23: Example of depth measurements at origin of external iliac artery.

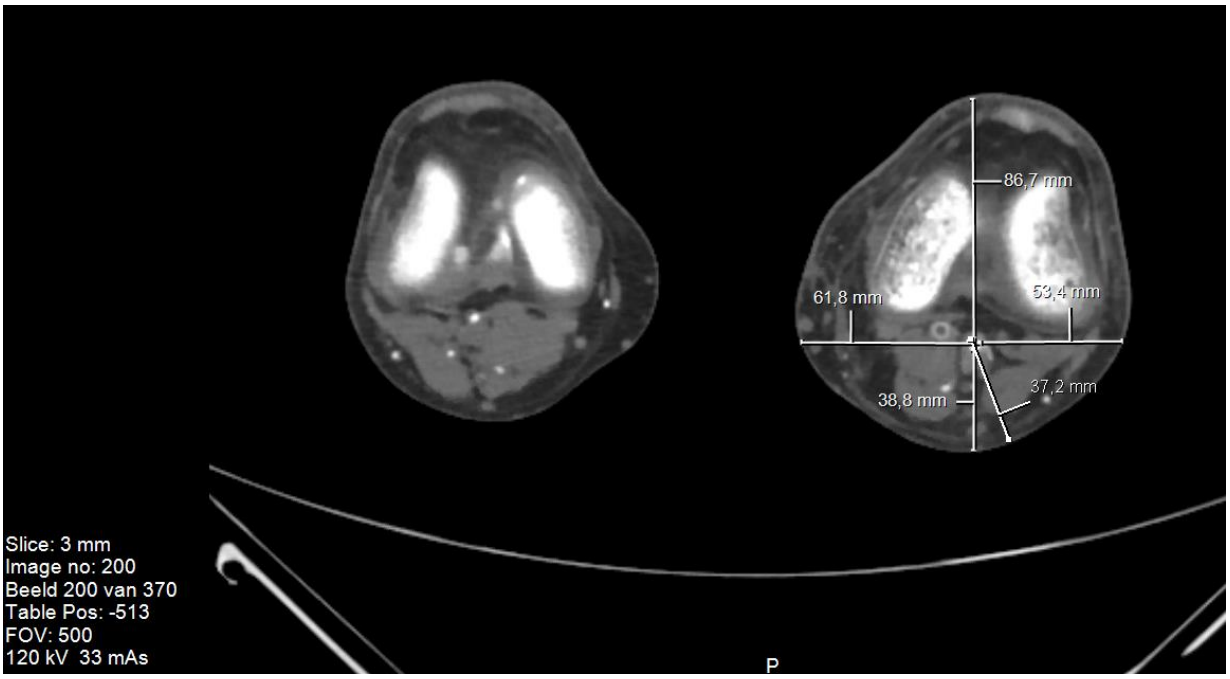

Figure 24: Example of depth measurements at origin of popliteal artery at the first slice on which kneecap is not visible when looking in a craniocaudal direction.

Appendix B

Bland-Altman plots of Manual depth measurements

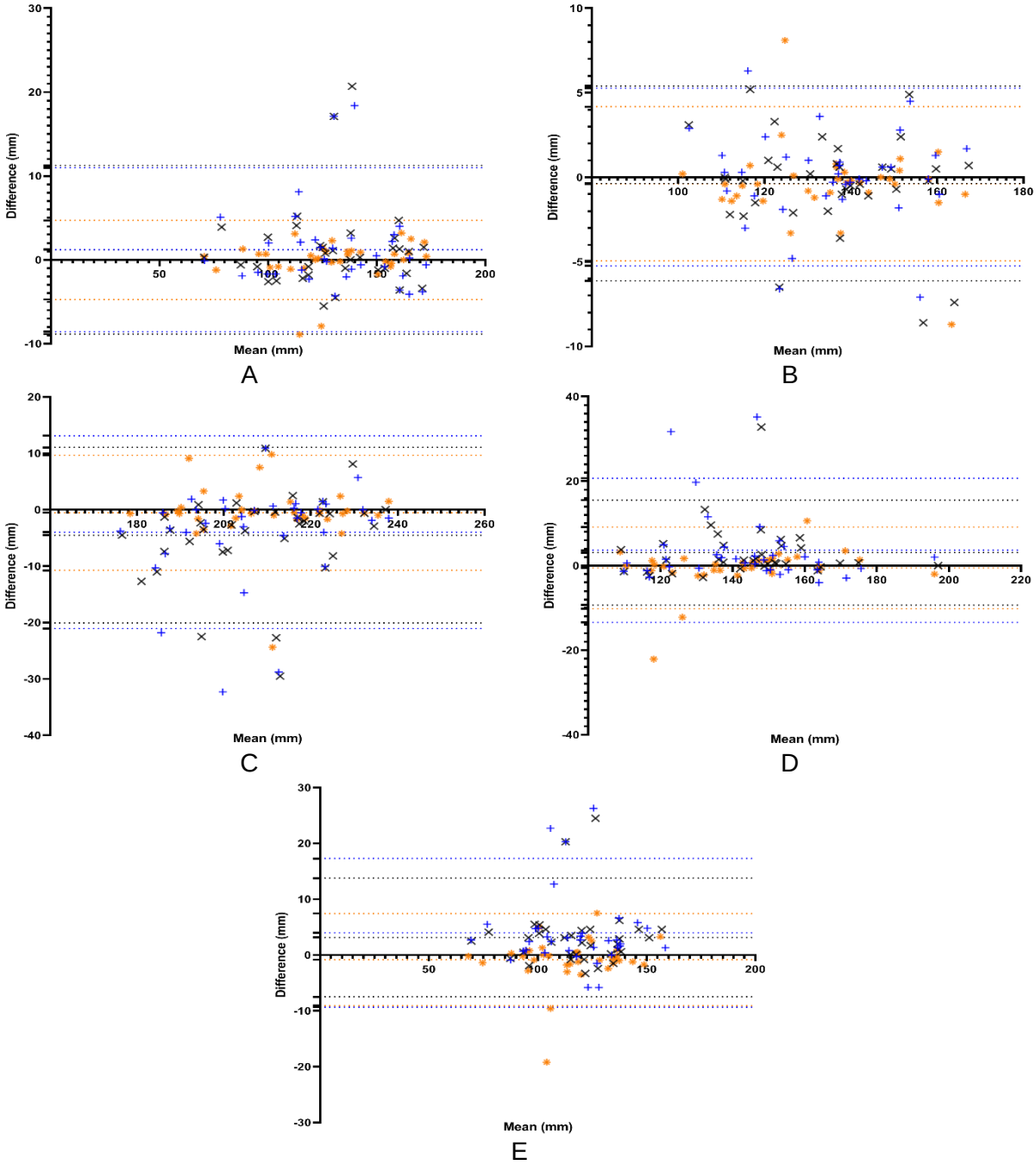

Figure 25: Bland-Altman plots for depth measurements in the AIE in measurements direction A (A), B (B), C (C), D (D) and E (E). Figures show comparison of measurements performed by observer 1 and 2 (Blue), observer 1 and 3 (Black) and observer 2 and 3 (Orange). In all plots the horizontal dotted colored lines represent from top to bottom the upper limit of agreement, the bias and the lower limit of agreement with corresponding to the compared measurements.

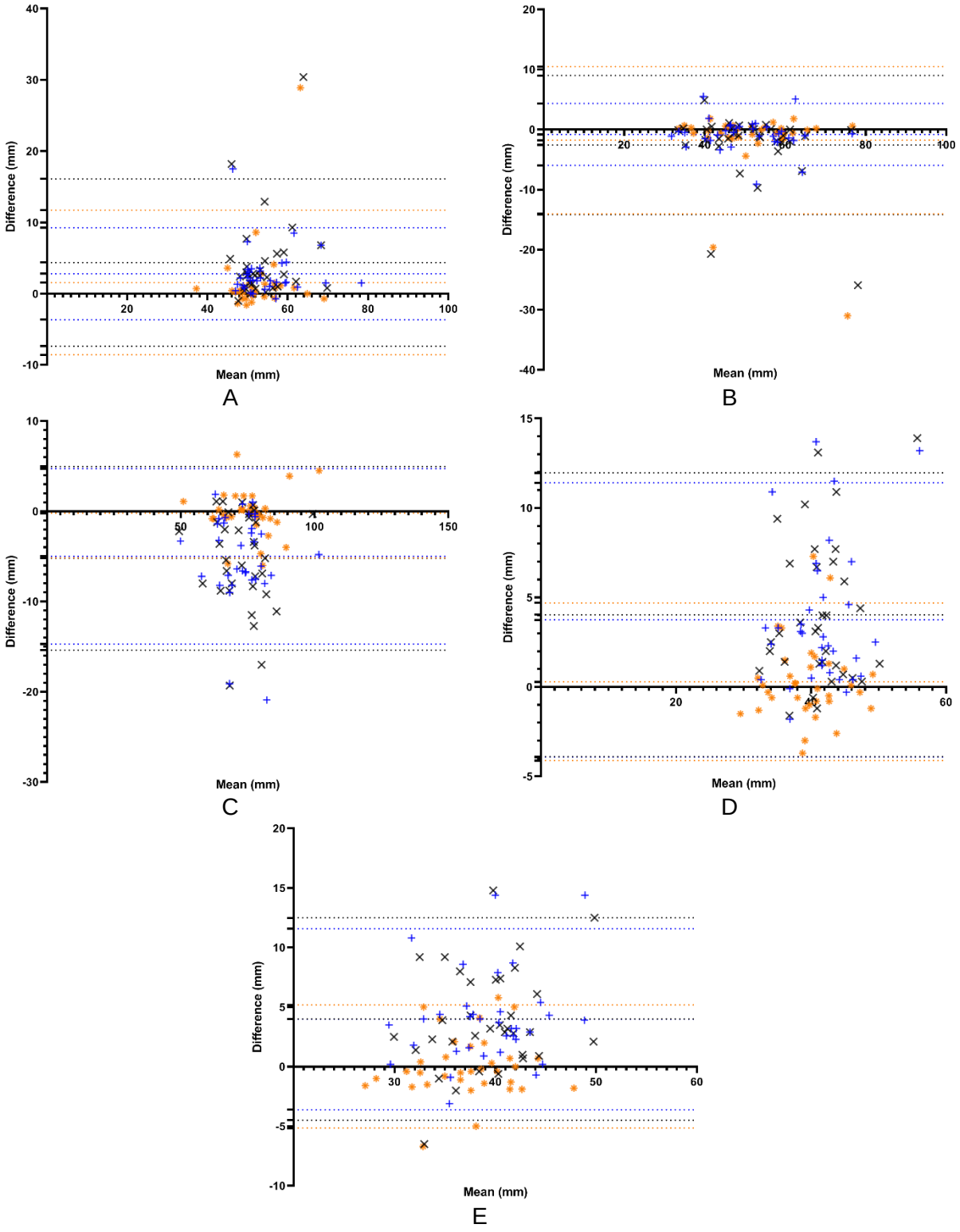

Figure 26: Bland-Altman plots for depth measurements in the ATA in measurements direction A (A), B (B), C (C), D (D) and E (E). Figures show comparison of measurements performed by observer 1 and 2 (Blue), observer 1 and 3 (Black) and observer 2 and 3 (Orange). In all plots the horizontal dotted colored lines represent from top to bottom the upper limit of agreement, the bias and the lower limit of agreement with corresponding to the compared measurements.

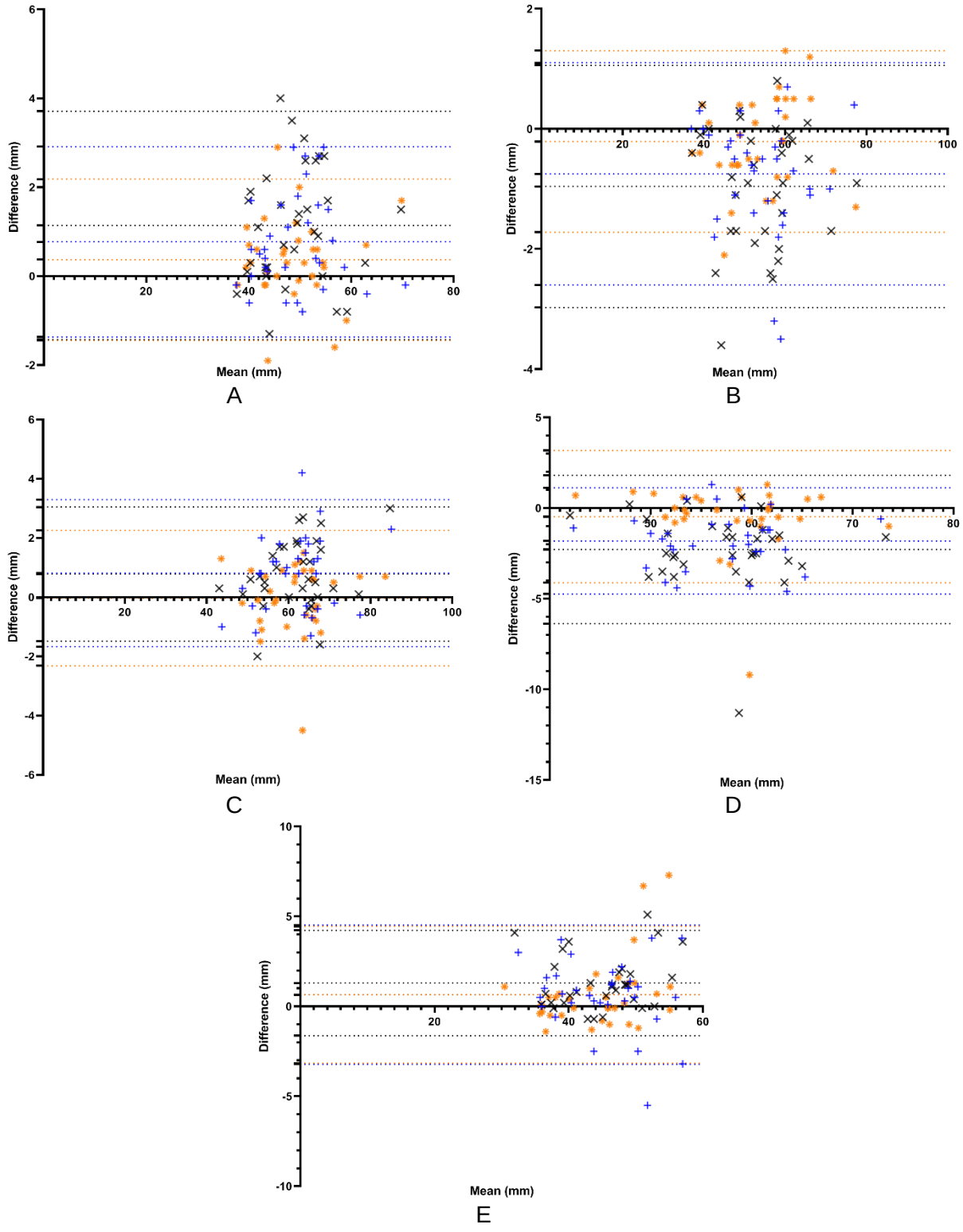

Figure 27: Bland-Altman plots for depth measurements in the ATP in measurements direction A (A), B (B), C (C), D (D) and E (E). Figures show comparison of measurements performed by observer 1 and 2 (Blue), observer 1 and 3 (Black) and observer 2 and 3 (Orange). In all plots the horizontal dotted colored lines represent from top to bottom the upper limit of agreement, the bias and the lower limit of agreement with corresponding to the compared measurements.